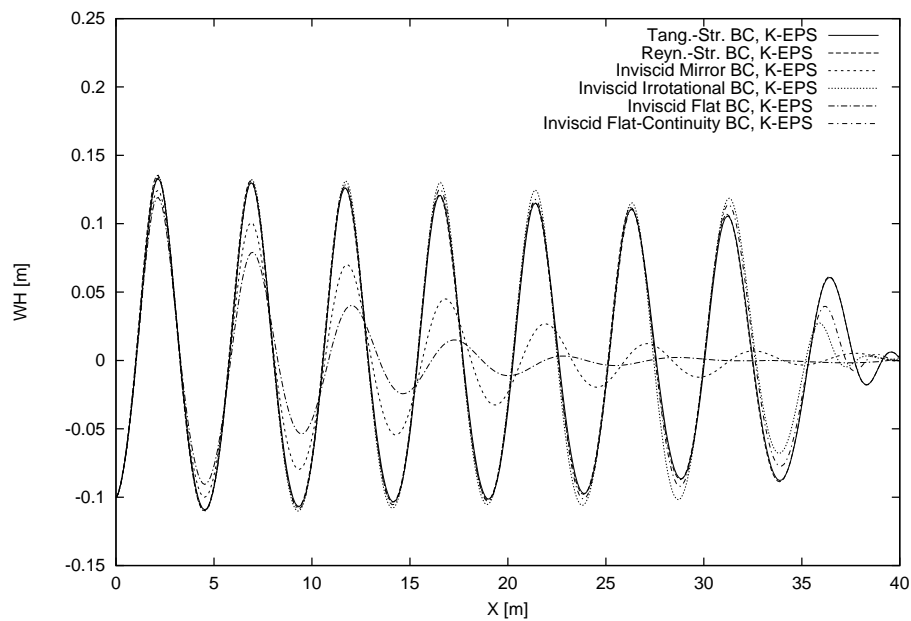# Helsinki University of Technology - Ship Laboratory

Investigation of Two-Dimensional Transom Waves Using Inviscid and Viscous Free-Surface Boundary Conditions at Model- and Full-Scale Ship Reynolds Numbers

Juha Schweighofer

June 5, 2003

Abstract

Two-dimensional transom waves are computed using inviscid and viscous free-surface boundary conditions at model- and full-scale ship Reynolds numbers. The computations are carried out solving the steady Euler or RaNS equations with the Navier-Stokes solver, FINFLO. The viscous free-surface boundary conditions are obtained from a flat-surface approximation. Different numerical schemes used when evaluating the free-surface deformation are presented. Their effect on the evaluated transom waves and the flow field is discussed at model and full scale. Further, computations of turbulent free-surface flows carried out at full-scale ship Reynolds numbers using the moving-grid technique and no wall functions are presented and discussed. An improved extrapolation method combining model testing and CFD is proposed.

The simulations in this work demonstrate the significant effect of the numerical realization of the free-surface boundary conditions and the decreasing Froude number on the computed transom waves, the flow field and the total resistance. At full-scale ship Reynolds numbers, multigridding will speed up the convergence. The free-stream dissipation of the turbulent kinetic energy has to be treated like a material property when using Chien's low-Reynolds number k-ϵ turbulence model. The scaling of the computed results is in excellent agreement with the modified ITTC-78 method. The convected turbulent kinetic energy is amplified by the transom waves. At the vicinity of the transom, a significant increase of the nondimensional vorticity is obtained at full scale.

Key words: FINFLO, transom waves, free-surface boundary conditions, Reynolds-averaged Navier-Stokes equations, Euler equations, full scale, scaling.

Preface

This work is dedicated to my parents Terttu and Gernot Schweighofer, and the memory of my grandparents Martta and Tapani Savimäki.

I would like to express my deepest gratitude to my supervisor, Prof. Jerzy Matusiak, for his support and interest in my work during all stages of my studies. I am obliged also to Prof. Petri Varsta, the head of the Ship Laboratory of Helsinki University of Technology, for his practical advices and the excellent working conditions I experienced.

I would like to thank Mrs. Leila Silonsaari for her invaluable support with respect to the university bureaucracy, and her personal encouragement during all the past years.

I would like PhD. Tinqui Li to accept my best thanks for his critics regarding the research carried out, and his valuable hints concerning the existing literature.

I am grateful to Lic.Sc. Ilkka Saisto and Mr. Tommi Mikkola for their information on their own results and the free-surface subroutine of FINFLO.

Special thanks are given to D.Sc. Antonio Sanchez, D.Sc. Petri Kaurinkoski, D.Sc. Reijo Lehtimäki, Mr. Antti Hellsten and Mr. Mikko Korhonen for their support in running the FINFLO code and the post-processing tools.

I am deeply obliged to Prof. Timo Siikonen for the creation of the CFD Graduate School, his excellent lectures, and his fruitful advices.

I would like to say:"Thank you!", to the always friendly staff of the Ship Laboratory, and my friends in Finland. Particularly to Lic.Sc. Hendrik Naar, Mr. Meelis Mäesalu and Ms. Karin Sitzwohl for their sincere friendship during the past years. What is a man without friends? Nothing.

Finally, I would like to express my deepest gratitude to my beloved wife, Petra, for her warm affection to me, and for reminding me that there is also something else than ships in this world. What is a man without a woman? Not as much as he could be.

Espoo, June 5, 2003   Juha Schweighofer

Contents

Nomenclature

A	wetted surface, reference area
A^+	Van Driest damping constant
B	width of the model slice
C, C_1, C_2, C_3, C_μ	empirical coefficients
C_D, C_T	drag coefficient, total resistance coefficient
C_F	mean skin friction coefficient
C_f	local skin friction coefficient
C_P	pressure resistance coefficient
C_R	residual resistance coefficient
C_{TM}	measured total resistance coefficient of the model
C_{TMC}	computed total resistance coefficient of the model
C_{TS}	total resistance coefficient of the ship
C_{TSC}	computed total resistance coefficient of the ship
C_v	viscous resistance coefficient
ΔC_F	difference of the mean skin friction coefficient
d	thickness of a cell
$DTWMAX$	dimensional Courant number in the free-surface evaluation
F, G, H	flux vectors in the x-, y- and z-directions
F_{Kleb}	Klebanoff intermittency function
F_{max}	maximum of the turbulence function, F
Fn_T	Froude number based on the draught of the transom
g	gravitational constant
I_∞	free-stream turbulence level
$\vec{i}$, $\vec{j}$, $\vec{k}$	unit vectors in the x-, y- and z-directions
K	curvature of the free surface
k	turbulent kinetic energy, form factor
K-EPS	k-ϵ turbulence model
L	length overall
l_{mix}	mixing length
L_{pp}	length between perpendiculars

n, t	referred to the normal and tangential directions on the free surface
n	number of control volumes
$\vec{n}, \vec{t}$	normal and tangential vectors on the free surface
n_i, t_i	components of the normal and tangential vectors on the free surface
n_x	x-component of the normal unit vector on the hull
P	production of turbulent kinetic energy
p	pressure
Q	source term
R	radius of bow
Re_l	Reynolds number
Re_x	local Reynolds number
Re_T	turbulence Reynolds number
Re_Θ	Reynolds number based on the boundary-layer momentum thickness
R_P	pressure resistance
R_T	total resistance
T	stress tensor, depth of transom
t	time
t_x	x-component of the tangential unit vector on the hull
U	vector of conservative variables
u, v, w	velocity components in the x-, y- and z-directions
u_τ	friction velocity
U_∞	free-stream velocity
u^+	nondimensional velocity component in the x-direction
$\vec{V}$	velocity vector
V_T	mean velocity in direction tangential to the wall
$V_{T,diff}$	difference between the maximum and minimum tangential velocity in the velocity profile
WH	wave height
X	distance from the transom
x, y, z	coordinate directions of a Cartesian coordinate system
y_n, y^+	dimensional and nondimensional normal distances from the wall
$y_{n,max}$	distance from the wall where $F = F_{max}$
y_m	inner/outer-layer matching point of the Baldwin-Lomax model
$|z|, |z|^+$	dimensional and nondimensional distance from the wall

α	closure coefficient
β	local wave elevation
$\vec{\gamma}$	vorticity vector
γ^*	nondimensional vorticity
Δ	residual
δ	boundary-layer thickness
δ_{ij}	Kronecker delta
ϵ	dissipation of turbulent kinetic energy
κ	Kármán constant
λ	wave length, scale
$\Delta\lambda$	difference of the wave length
μ	molecular viscosity
μ_T	turbulent viscosity
μ_{Ti}	turbulent viscosity of the Baldwin-Lomax model in the inner layer
μ_{To}	turbulent viscosity of the Baldwin-Lomax model in the outer layer
μ_k	diffusion coefficient
μ_ϵ	diffusion coefficient
ν	kinematic viscosity
ρ	density of the fluid
$-\rho\overline{u_i' u_j'}$	Reynolds stresses
σ	surface tension
$\sigma_k, \sigma_\epsilon$	turbulent Prandtl numbers for k and ϵ
τ	stress
Φ	flow quantity
$\|\Phi\|_2$	L_2-norm of a quantity, Φ
ψ	piezometric pressure
∇	nabla operator
ω	vorticity

Superscripts:

T transpose of a vector

Subscripts:

air	referred to air
$Blasius$	referred to Blasius
FS	free surface
$Fullyturb.$	referred to a from the beginning fully turbulent flow
i, j	grid-coordinate directions
i, j, k	cell centre
$liquid$	referred to fluid
max	maximum
$true$	true value
v	viscous
$wall$	value on the wall
$White$	referred to White
xx, yy, zz	indicate normal stresses
xy, xz, yz	indicate shear stresses
$1, 2, 3$	x-, y- and z-components
∞	referred to free-stream values

Abbreviations:

BC	boundary condition
BL1, BL2, BL3, BL4	blocks of the computational domain
CFD	computational fluid dynamics
CPU	central processing unit
DDADI	diagonally dominant alternating direction implicit
FINFLO	finite-volume-based Reynolds-averaged Navier-Stokes solver developed at Helsinki University of Technology
FSC	full scale
GB	gigabyte
ITTC	International Towing Tank Conference
MB	megabyte
Mflop	megaflop
MSC	model scale
RaNS	Reynolds-averaged Navier-Stokes
SST	shear-stress transport
2-d	two-dimensional

1 Introduction

1.1 General

A ship moving in water always creates a wave system. In the computational analysis of such a wave system, the kinematic and the dynamic boundary conditions are required for the free surface. Usually, several simplifications are introduced in viscous flow simulations leading to the same free-surface boundary conditions as in potential flow simulations. However, there is vorticity at the free surface, *Choi and Stern (1993), Dabiri and Gharib (1997), Longuet-Higgins (1997), Lundgren and Koumoutsakos (1999), Ohkusu (1996).* In consequence, the velocity gradients are non-zero. Also, the pressure is non-zero due to the viscous terms appearing in the dynamic boundary condition in the normal direction to the free surface. The error associated with the application of the inviscid free-surface boundary conditions may be unacceptable, *Stern et al. (1996).* The application of the physically correct viscous free-surface boundary conditions seems to be desirable. Even for identical analytical formulation of the free-surface boundary conditions, computed wave profiles differ depending on the numerical scheme used. Publications usually give the analytical formulation, but, unfortunately, the numerical scheme employed is seldom presented or discussed.

There are a few publications on ship flow computations using the viscous free-surface boundary conditions, *Lilek (1995,1996), Alessandrini and Delhommeau (1994,1997), Liu and Kodama (1993), Cowles and Martinelli (1999), Jeong and Doi (1995), Dong and Huang (1999), Gentaz et al. (2000), Vogt (1998).* Comparative studies of the influence of the viscous and inviscid free-surface boundary conditions on ship flows are very rare. The viscous free-surface boundary conditions give results of improved or at least of equal accuracy compared to the inviscid ones. So far, detached transom flows over

a large range of Reynolds numbers up to full scale have not been treated using the viscous free-surface boundary conditions including the influence of turbulence. Most ships have a transom, and the stern induced resistance is significant, *Saisto (2000)*. *Vanden-Broek (1980)* and *Saisto (1995,2000)* investigated 2-d detached transom flows as potential flow past a semi-infinite flat-bottomed body. Respective viscous flow evaluations are given in *Tahara and Iwasaki (1998), Funeno and Yamano (2001)* and *Yamano et al. (2000,2001)*. In transom flows, the boundary layer of the hull is convected into the transom waves. There, the velocity gradients and vorticity are stronger compared with the case where the boundary layer is not taken into account. Therefore, in such cases, the application of the viscous free-surface boundary conditions seems to be appropriate.

Usually, numerical investigations of turbulent free-surface flows are carried out at Reynolds numbers of a model-scale ship. The results obtained must be scaled to full scale, which might cause errors in the case of new vessel types where the scaling mechanisms are not known. Computations of full-scale ships are attractive as no scaling is necessary, and the allowances may be reduced. The shape of the hull and the propeller may be optimized with respect to the proper flow around the ship. Additionally, computations of full-scale ships will serve as supplement to model testing as more insight in the scaling mechanisms is obtained. Computations of turbulent flows solving the RaNS equations at full-scale ship Reynolds numbers are presented in the following references: *Ju and Patel (1991,1994), Tzabiras (1992,1993), Ishikawa (1994), Schmitt (1997), Eca and Hoekstra (1997,2000), Schweighofer (1997), Dolphin (1997), 6 from Larsson et al. (2000), Chen et al. (2001), Starke (2001), Chao (2001)*. In only one of these publications, *Chen et al. (2001)*, turbulent free-surface flows have been computed at full-scale ship Reynolds numbers. *Chen et al. (2001)* used a fixed-grid technique and wall functions. The results were significantly affected by the grid resolution, *Chen (2001)*. The computed waves showed a slight dependence on the Reynolds number, *Chen (2001)*. *Yamano et al. (2001)* investigated the scale effect on the stern-wave resistance, and they presented results up to the Reynolds number of a full-scale ship. Nevertheless, they did not solve the RaNS equations. Instead, they used empirical relations for the velocity and boundary-layer thickness at the stern, and the waves and the flow lines below the free surface were approximated by trochoids.

At full-scale ship Reynolds numbers, turbulent free-surface flows have not been computed using the moving grid-technique without the use of wall functions. Compared with the fixed-grid techniques, the moving-grid technique has several advantages. The conservation of mass and momentum can easily

be fulfilled on the free surface, and the application of the free-surface boundary conditions is easy to carry out, *Lilek (1996).* Applying wall functions to full-scale computations of turbulent ship flows, the amount of grid cells may be kept fairly small. Therefore, the computational times can be kept short. Nevertheless, it is difficult to define a wall function applicable to different geometries. Physically more correct and of more general validity is the computation of the entire boundary layer until the wall instead of the use of a predetermined nondimensional velocity profile.

1.2   Scope of the Work

This work focusses on two tasks related to each other. The first one is to carry out a comparative study of the influence of the viscous and inviscid free-surface boundary conditions on two-dimensional detached transom flow at model-scale and full-scale ship Reynolds numbers. The second one is to discuss computations of turbulent free-surface flows using the moving-grid technique and no wall functions at full-scale ship Reynolds numbers. In particular, the following items are considered in this work:

- Different free-surface boundary conditions and their numerical realizations are presented. Their effect on the evaluated transom waves and the flow field at model-scale and full-scale ship Reynolds numbers is discussed.

- Using the moving-grid technique, the computations of the turbulent flow are conducted without the application of wall functions at different Reynolds numbers of a ship corresponding to model scale and full scale.

- The efficiency of multigridding at the full-scale Reynolds number of a ship is discussed.

- The influence of the free-stream turbulence quantities on the turbulent boundary-layer flow is evaluated at the Reynolds number of a full-scale ship.

- The influence of the boundary layer on the transom waves is discussed.

- The scaling of the pressure and skin friction resistance is evaluated and compared with the ITTC-57 and ITTC-78 extrapolation methods.

- An improved extrapolation method combining model testing and CFD is proposed.

The Reynolds-averaged Navier-Stokes equations or the Euler equations are iteratively solved by the FINFLO code until the steady state is reached. A cell-centered finite-volume method is applied. No wall functions are used. Turbulence is treated by Chien's low-Reynolds number k-ϵ turbulence model. Further, the Baldwin-Lomax model is used for the investigation of multigridding at the full-scale ship Reynolds number. Incompressibility of the flow is considered by an artificial-compressibility approach. The free-surface is evaluated by a moving-grid technique.

Following the primary suggestions of PhD. Tinqui Li, the viscous free-surface boundary conditions are implemented into the FINFLO code in two dimensions. A flat-surface approximation is used. The implementation is carried out in Cartesian coordinates. The free-surface boundary conditions and the continuity equation are applied directly on the free surface. Nevertheless, the necessary velocity gradients are calculated from the velocities at the cell centres below the free surface. Further, alternative inviscid free-surface boundary conditions are investigated, which are implemented also in two-dimensions. Numerous computations of the two-dimensional flat-bottomed model, *Ile*, are conducted at the Froude numbers, 2.1, 2.2, 2.3 and 2.8 and the Reynolds numbers, 2.8×10^6, 2.933×10^6, 3.066×10^6, 3.732×10^6 and 9.442×10^8. The appearance of the bow wave is suppressed. At the transom, the wave-height is set equal to the depth of the transom.

The investigations are performed in two dimensions to keep CPU times reasonably short. This simplifies the problem, allowing to evaluate the pure influence of the free-surface boundary conditions on the computed transom waves. The conclusions should be valid also for three dimensions. In the future, the obtained knowledge will concretely contribute to full-scale computations of ships.

The simulations of this work demonstrate the significant effect of the numerical realization of the free-surface boundary conditions on the computed transom waves. Further, at the investigated Froude numbers lower than 2.8, it makes physically a difference whether the inviscid irrotational or the Reynolds-stress free-surface boundary conditions are used. Multigridding at full-scale ship Reynolds numbers will speed up the convergence. The free-stream dissipation of the turbulent kinetic energy has to be treated like a material property when using Chien's low-Reynolds number k-ϵ turbulence model. For detached transom flows over a flat bottom at the two higher Reynolds numbers, the boundary layer has very little influence on the appearing transom waves, and the pressure resistance coefficient is almost independent of the Reynolds number. The scaling of the computed results is in excellent agreement with the modified ITTC-78 method. The ITTC-57

extrapolation method overestimates slightly the total resistance coefficient. The form factor with respect to the skin friction line of a flat plate remains constant. If no wave breaking occurs, then the Boussinesq approximation will have no influence on the evaluated waves through the dynamic free-surface boundary condition with respect to the normal stresses on the free-surface. For the investigated case at the highest Froude number, the influence of the turbulent viscosity on the transom waves through the dynamic free-surface boundary conditions can be neglected at model and full scale. The convected turbulent kinetic energy is amplified by the transom waves. At the vicinity of the transom, the increase of the Reynolds number causes a significant increase of the nondimensional vorticity.

The results shown demonstrate that free-surface computations of turbulent ship flows are possible at full-scale ship Reynolds numbers using the moving-grid technique and no wall functions.

2 Numerical Method

The computations below are carried out using the Navier-Stokes solver, FIN-FLO, originally developed in the Laboratory of Aerodynamics of Helsinki University of Technology, *Kaurinkoski and Hellsten (1998), Siikonen et al. (1990), Siikonen (1995), Siikonen (1996)*. The work of Siikonen is associated with the the development of the largest part of FINFLO. In the past six years, in the Ship Laboratory of the Helsinki University of Technology, this flow solver has been further developed for the treatment of ship flows, *Li (2000), Mikkola (1999), Sundell (1997)*. The Reynolds-averaged Navier-Stokes equations are iteratively solved by a cell-centered finite-volume method until a steady state is reached. Incompressibility of the flow is considered by an artificial compressibility approach, *Rahman et al. (1997)*. An upwind-type spatial discretization of third-order accuracy without flux limitation is applied to the approximation of the convective terms. Incompressible flux-difference splitting is used as flux-splitting method, *Rahman (1997), Rahman (2000)*. The viscous fluxes are evaluated according to a thin-layer approximation which is activated in all coordinate directions. Here, the central differencing scheme is used for the calculation of the velocities at the cell surfaces. The solution of the discretized equations is obtained using a diagonally dominant alternating direction implicit (DDADI) time integration method, *Lombard et al. (1983)*, with local time stepping. The turbulence is treated by Chien's low-Reynolds number k-ϵ turbulence model. The computations are carried out without the application of multigridding. Nevertheless, at the full-scale ship Reynolds number, the efficiency of multigridding is evaluated using the Baldwin-Lomax turbulence model. The free surface is evaluated by a moving-grid technique, *Lehtimäki (2000), Li (2000), Mikkola (1999), Sundell (1997)*.

2.1   Governing Equations

The computations are carried out using an incompressible fluid as medium. Therefore, the following theory is explained for incompressible flows. Nevertheless, it should be kept in mind that FINFLO is a Navier-Stokes solver for compressible flows. Incompressibility of the flow in question is taken into account by the above mentioned features.

In a right-handed Cartesian coordinate system, the Reynolds-averaged Navier-Stokes equations for incompressible flow and the equations for the turbulent kinetic energy, k, and the dissipation of the turbulent kinetic energy, ϵ, can be written in the following form:

$$\frac{\partial U}{\partial t} + \frac{\partial \left(F - F_v \right)}{\partial x} + \frac{\partial \left(G - G_v \right)}{\partial y} + \frac{\partial \left(H - H_v \right)}{\partial z} = Q \ , \qquad (2.1)$$

where $U = (\rho, \rho u, \rho v, \rho w, \rho k, \rho \epsilon)^T$, and t is the time. The inviscid fluxes, F, G and H, are

$$F = \begin{pmatrix} \rho u \\ \rho u^2 + \psi \\ \rho v u \\ \rho w u \\ \rho u k \\ \rho u \epsilon \end{pmatrix} \ , \quad G = \begin{pmatrix} \rho v \\ \rho u v \\ \rho v^2 + \psi \\ \rho w v \\ \rho v k \\ \rho v \epsilon \end{pmatrix} \ , \quad H = \begin{pmatrix} \rho w \\ \rho u w \\ \rho v w \\ \rho w^2 + \psi \\ \rho w k \\ \rho w \epsilon \end{pmatrix} \ . \quad (2.2)$$

U is the vector of the conservative variables. ρ is the density of the fluid. The velocity is $\vec{V} = u\vec{i} + v\vec{j} + w\vec{k}$, where u, v and w are the velocity components in the x-, y- and z-directions, respectively. ψ is the piezometric pressure which is defined as

$$\psi = p + \rho g z \ . \qquad (2.3)$$

p is the static pressure, g is the gravitational constant, and z is the z-coordinate of the location of interest. The z-axis is directed upwards from the free surface (Fig. 3.1). The viscous fluxes are

$$F_v = \begin{pmatrix} 0 \\ \tau_{xx} \\ \tau_{xy} \\ \tau_{xz} \\ \mu_k \left(\frac{\partial k}{\partial x} \right) \\ \mu_\epsilon \left(\frac{\partial \epsilon}{\partial x} \right) \end{pmatrix} \ , \quad G_v = \begin{pmatrix} 0 \\ \tau_{xy} \\ \tau_{yy} \\ \tau_{yz} \\ \mu_k \left(\frac{\partial k}{\partial y} \right) \\ \mu_\epsilon \left(\frac{\partial \epsilon}{\partial y} \right) \end{pmatrix} \ , \quad H_v = \begin{pmatrix} 0 \\ \tau_{xz} \\ \tau_{yz} \\ \tau_{zz} \\ \mu_k \left(\frac{\partial k}{\partial z} \right) \\ \mu_\epsilon \left(\frac{\partial \epsilon}{\partial z} \right) \end{pmatrix} \ . \quad (2.4)$$

Because of the incompressibility of the flow, the term, $\nabla \cdot \vec{V}$, is equal to zero, which is consistent with the continuity equation. Therefore, the stress tensor, τ_{ij}, may be given as

$$\tau_{ij} = \mu \left(\frac{\partial u_i}{\partial x_j} + \frac{\partial u_j}{\partial x_i} \right) - \rho \overline{u_i' u_j'} \ . \tag{2.5}$$

The Boussinesq approximation, *Anderson et al. (1984)*,

$$-\rho \overline{u_i' u_j'} = \mu_T \left(\frac{\partial u_i}{\partial x_j} + \frac{\partial u_j}{\partial x_i} \right) - \frac{2}{3} \rho k \delta_{ij} \ , \tag{2.6}$$

is applied to the Reynolds stresses, $-\rho \overline{u_i' u_j'}$. μ and μ_T are the molecular and the turbulent viscosities, respectively, and δ_{ij} is the Kronecker delta. $(u_1, u_2, u_3) = (u, v, w)$ and $(x_1, x_2, x_3) = (x, y, z)$.

The source term, Q, and the diffusion coefficients of the turbulence quantities, μ_k and μ_ϵ, are given in the following section.

2.2 Turbulence Models

2.2.1 Chien's Low-Reynolds Number k-ϵ Turbulence Model

In Eq. (2.6), the Reynolds stresses, $-\rho \overline{u_i' u_j'}$, are calculated using the turbulent viscosity, μ_T. The turbulent viscosity is derived from Chien's low-Reynolds number k-ϵ turbulence model, *Chien (1982), Wilcox (1993), Schweighofer (1997)*, where two transport equations for the turbulent kinetic energy, k, and the dissipation of the turbulent kinetic energy per unit mass, ϵ, are solved (Eqs. 2.1, 2.2, 2.4 and 2.7). In further consequence, the turbulent viscosity is calculated as a function of k and ϵ.

The task of this investigation is not the development of a new turbulence model with respect to free-surface flows. The available turbulence models in association with the Boussinessq approximation are Chien's low-Reynolds number k-ϵ turbulence model, the Baldwin-Lomax turbulence model, *Baldwin and Lomax (1978), Wilcox (1993), Schweighofer (1997)*, and Menter's k-ω SST turbulence model, *Menter (1993), Schweighofer (1997)*. The Baldwin-Lomax model is not able to reproduce the turbulent viscosity in the transom waves to be computed as it depends only on the local instantaneous flow condition and no turbulence is convected into the waves. The turbulent viscosity can be calculated only within the boundary layer close to the wall, but not

within the transom waves. Menter's k-ω SST turbulence model would be a promising alternative. It has been implemented into the code, *Brandt (2000)*, but at this stage, it has not been tested sufficiently. Therefore, the only appropriate choice is Chien's low-Reynolds number k-ϵ turbulence model. At model scale, it has been applied to ship flows by *Saisto and Sundell (1996)* giving an accuracy of less than five percent for the total resistance coefficient. *Schweighofer (1997)* proved its applicability to turbulent flows over a flat plate for Reynolds numbers up to full-scale ship Reynolds numbers. The turbulence is convected from the boundary layer at the wall into the waves, and the influence of the free-surface on the turbulence can be taken into account by the production of the turbulent kinetic energy, which is determined from the turbulent viscosity and the appearing velocity gradients. The pressure gradients are expected to be small as the ratio of the length between the perpendiculars and the draught of the model, L_{pp}/T, is equal to fifteen, and no complicated separation with back flow is expected to occur, which is concluded from the measurements of *Saisto (1995)*. Therefore, Chien's low-Reynolds number k-ϵ turbulence model is assumed to be sufficient for the investigation to be performed. The Boussinesq approximation gives satisfactory results for ship flows without a free surface, *Saisto and Sundell (1996), Schweighofer (1997)*. Nevertheless, the evaluated free surface might be influenced through the dynamic free-surface boundary conditions by the turbulent viscosity and the Boussinesq approximation. One task of this work is the evaluation of this influence and the applicability of the Boussinesq approximation to free-surface computations.

In Chien's k-ϵ turbulence model, no wall-function approach is used. The solution is extended to the wall, the whole computational domain is treated with the same scheme, and the wall-reflection terms vanish further away from solid surfaces. The source term, Q, is given as

$$
Q = \begin{pmatrix} 0 \\ 0 \\ 0 \\ 0 \\ P - \rho\epsilon - 2\mu\frac{k}{y_n^2} \\ C_1\frac{\epsilon}{k}P - C_2\frac{\rho\epsilon^2}{k} - 2\mu\frac{\epsilon}{y_n^2}e^{-y^+/2} \end{pmatrix} , \tag{2.7}
$$

where y_n and y^+ are the dimensional and the nondimensional normal distances from the wall, respectively. The nondimensional distance from the

wall, y^+, is obtained from

$$y^+ = y_n \frac{\rho u_\tau}{\mu} = y_n \frac{\sqrt{\rho \tau_{wall}}}{\mu} = y_n \left[\frac{\rho |\nabla \times \vec{V}|}{\mu} \right]^{1/2}_{wall} . \tag{2.8}$$

u_τ and τ_{wall} are the friction velocity and the wall-shear stress, respectively. In Eq. (2.7), ϵ is a modified dissipation per unit mass. The true dissipation per unit mass, ϵ_{true}, is derived from

$$\epsilon_{true} = \epsilon + 2 \frac{\mu k}{\rho y_n^2} . \tag{2.9}$$

Using Eq. (2.6) for the Reynolds stresses, $-\rho \overline{u_i' u_j'}$, the production of turbulent kinetic energy, P, is modelled as

$$\begin{aligned} P &= -\rho \overline{u_i' u_j'} \frac{\partial u_i}{\partial x_j} \\ &= \left[\mu_T \left(\frac{\partial u_i}{\partial x_j} + \frac{\partial u_j}{\partial x_i} \right) - \frac{2}{3} \rho k \delta_{ij} \right] \frac{\partial u_i}{\partial x_j} . \end{aligned} \tag{2.10}$$

In certain cases, the turbulent viscosity, μ_T, may become unphysically high, e.g. close to the stagnation point. In order to avoid this phenomena, the production of turbulent kinetic energy, P, is limited as suggested by *Menter (1993)*

$$P = min\left(P, 20\rho\epsilon \right) . \tag{2.11}$$

The turbulent viscosity, μ_T, is calculated from

$$\mu_T = C_\mu \frac{\rho k^2}{\epsilon} . \tag{2.12}$$

In Eqs. (2.7, 2.12, 2.15 and 2.16), several empirical coefficients appear. These are

$$\begin{aligned} C_1 &= 1.44 , \\ C_2 &= 1.92 \left(1 - 0.22 e^{-Re_T^2/36} \right) , \\ C_\mu &= 0.09 \left(1 - e^{-0.0115 y^+} \right) , \\ \sigma_k &= 1.0 , \\ \sigma_\epsilon &= 1.3 , \end{aligned} \tag{2.13}$$

where Re_T is the turbulence Reynolds number. It is obtained from

$$Re_T = \frac{\rho k^2}{\mu \epsilon} . \tag{2.14}$$

In the expressions for C_1 and C_2, the constants, 1.44 and 1.92, are the same as in the standard k-ϵ model, *Wilcox (1993)*. In Chien's original model, slightly different constants are used, namely 1.35 and 1.80.

Finally, the diffusion coefficients of the turbulence quantities are derived from

$$\mu_k \quad = \quad \mu + \frac{\mu_T}{\sigma_k} \; , \tag{2.15}$$

$$\mu_\epsilon \quad = \quad \mu + \frac{\mu_T}{\sigma_\epsilon} \; , \tag{2.16}$$

where σ_k and σ_ϵ are the appropriate turbulent Prandtl numbers for k and ϵ.

2.2.2   The Baldwin-Lomax Turbulence Model

For the evaluation of the efficiency of multigridding at the full-scale ship Reynolds number, the Baldwin-Lomax turbulence model is used, *Baldwin and Lomax (1978), Wilcox (1993), Schweighofer (1997)*. In the beginning of the respective investigation at full scale, Chien's k-ϵ turbulence model gives false results with respect to the turbulence quantities which are due to certain limitations within the code (see also Section 4.1.2). Therefore, at this stage, the use of Chien's k-ϵ turbulence model is not appropriate. Further, the results obtained with the Baldwin-Lomax model may be used as additional reference for the evaluation of the reliability of the full-scale results later obtained with the corrected code, input and Chien's k-ϵ turbulence model.

The Baldwin-Lomax turbulence model is a two-layer model. The turbulent viscosity, μ_T, is given by separate expressions in each layer, and the turbulent viscosity is

$$\mu_T = \left\{ \begin{array}{ll} \mu_{Ti} & \text{for } y_n \leq y_m \; , \\ \mu_{To} & \text{for } y_n > y_m \; , \end{array} \right. \tag{2.17}$$

y_m is the smallest value of the perpendicular distance, y_n, from the wall at which the formulas give the same value. The minimum of these values is taken to be valid.

The turbulent viscosity in the inner layer is obtained from the Prandtl-van Driest formulation:

$$\mu_{Ti} = \rho l_{mix}^2 |\frac{\partial V_T}{\partial y_n}| \; , \tag{2.18}$$

where V_T is the mean velocity in direction tangential to the wall. l_{mix} is the mixing length given by

$$l_{mix} = \kappa y_n \left(1 - e^{-y^+/A^+} \right) \; , \tag{2.19}$$

where the constants, κ and A^+, are 0.4 and 26, respectively.

The turbulent viscosity in the outer layer is obtained from either

$$\mu_{To} = \alpha C_1 F_{Kleb} y_{n,max} F_{max} \rho \ , \tag{2.20}$$

or

$$\mu_{To} = \alpha C_1 F_{Kleb} C_2 V_{T,diff}^2 \frac{y_{n,max}}{F_{max}} \rho \ , \tag{2.21}$$

with $\alpha = 0.0168$, $C_1 = 1.6$ and $C_2 = 0.25$. The smallest alternative is taken. F_{max} is determined from the function

$$F = y_n |\frac{\partial V_T}{\partial y_n}|(1 - e^{-y^+/A^+}) \ .$$

F_{max} is the maximum value of F in the velocity profile. The corresponding distance from the wall is denoted by $y_{n,max}$. $V_{T,diff}$ is the difference between the maximum and minimum tangential velocity in the velocity profile. For walls, the minimum velocity is zero. The intermittency function is given by

$$F_{Kleb} = \frac{1}{1 + 5.5(C_3 y_n / y_{n,max})^6} \ , \tag{2.23}$$

where $C_3 = 0.3$.

In the RaNS equations, the turbulent kinetic energy and the dissipation of the turbulent kinetic energy are not used anymore. Therefore, the fluxes consist only of four lines instead of six ones, and the respective source term is

$$Q = \begin{pmatrix} 0 \\ 0 \\ 0 \\ 0 \end{pmatrix} \ . \tag{2.24}$$

2.3 Boundary Treatment

The computational domain is limited by different boundaries where different boundary conditions are applied. In the conducted computations, the following boundary conditions are used: external, mirror, solid wall and free surface.

At an external boundary, the flow quantities are simply set to their free-stream values.

On symmetry planes, usually the mirror condition is applied. Here, the flow quantities are mirrored from the computational domain to the ghost cells on the other side of the plane.

Solid walls may be defined as inviscid or viscous solid walls. Solving the Euler equations, inviscid solid walls are used allowing only tangential velocities at the surface.

Viscous solid walls are employed for the solution of the Reynolds-averaged Navier-Stokes equations. The no-slip condition on the wall is fulfilled by setting the velocities on the surface equal to zero. In this way, the only contribution to the inviscid fluxes arises from the pressure terms in the momentum equations. The pressure on the wall, ψ_{wall}, is evaluated from the pressure values of the computational domain using a second order extrapolation, *Siikonen (1996)*,

$$\psi_{wall} = \frac{3}{2}\psi_1 - \frac{1}{2}\psi_2 \ .$$ (2.25)

ψ_1 and ψ_2 are the pressure values in the first and the second cell from the wall, respectively. In the calculation of the inviscid fluxes at the solid boundary, flux-difference splitting is not used.

The viscous fluxes are calculated using the following equation for the appearing derivatives perpendicular to the solid wall, *Siikonen (1996)*:

$$\left(\frac{\partial \Phi}{\partial y_n}\right)_{wall} = \frac{9\Phi_1 - \Phi_2 - 8\Phi_{wall}}{3d_{wall}} \ ,$$ (2.26)

where Φ_1 and Φ_2 denote the values of the flow quantity, Φ, in the first and second cell from the wall, respectively. Φ_{wall} is the value of the flow quantity, Φ, at the wall, and d_{wall} is the thickness of the first cell above the surface. At the wall, the viscous fluxes for k and ϵ are set to zero, and the corresponding diffusion coefficients are obtained from a formula similar to Eq. (2.25). In this way, there is no need to specify the surface values of the turbulence quantities.

This work is focussed on the treatment of the free surface. Therefore, the treatment of the free surface is described in a separate section which is given in the following.

2.4 Free Surface

The free surface is evaluated using a moving-grid technique where the grid is deformed in order to fit the free surface at any time. This technique follows the principles of the so-called interface-tracking method.

On the free surface, the kinematic and dynamic boundary conditions are applied determining its shape.

The kinematic boundary condition states that a fluid particle remains on the free surface for all times. Through the free surface, no mass flow is allowed to appear. Therefore, the velocity components of the fluid particles normal to the free surface must be equal to zero. The kinematic boundary condition is fulfilled when, *Ferziger and Perić (1999)*,

$$\frac{d\beta}{dt} = w = \frac{\partial\beta}{\partial t} + u\frac{\partial\beta}{\partial x} + v\frac{\partial\beta}{\partial y} , \qquad (2.27)$$

where $\beta(x, y, t)$ is the local wave elevation. The kinematic boundary condition does not contain any approximations. It gives the rate of change of the wave height, β, provided the slope and the velocities on the free surface are known. Integration of Eq. (2.27) with respect to time gives the shape of the free surface. Having reached the steady state, $\frac{\partial\beta}{\partial t}$ will be equal to zero.

The dynamic boundary condition states that the normal and tangential stresses must be equal on both sides of the free surface. Generally, it may be written as, *Ferziger and Perić (1999)*,

$$(T_{liquid} \cdot \vec{n})\vec{n} = (T_{air} \cdot \vec{n})\vec{n} + \sigma K , \qquad (2.28)$$

$$(T_{liquid} \cdot \vec{n})\vec{t} = (T_{air} \cdot \vec{n})\vec{t} + \frac{\partial\sigma}{\partial t} . \qquad (2.29)$$

T_{liquid} and T_{air} are the stress tensors for the fluid and air. $\vec{n} = (n_1, n_2, n_3)^T$ is the unit normal vector on the free surface directed outwards from it. n_1, n_2 and n_3 are the corresponding vector components in the x-, y- and z-directions. Similarly, $\vec{t} = (t_1, t_2, t_3)^T$ is the unit tangential vector on the free surface. σ is the surface tension, and K is the curvature of the free surface. $\frac{\partial\sigma}{\partial t}$ is the local change of the surface tension in the tangential direction. The shear stresses of the air and the surface tension on the free surface are very small. Therefore, they are neglected. Using the tensor notation, the dynamic boundary condition may be rewritten as

$$(T_{ij}n_j)n_i = 0 , \qquad (2.30)$$

$$(T_{ij}n_j)t_i = 0 , \qquad (2.31)$$

where $T_{ij} = T_{liquid}$. The stress tensor, T_{ij}, is defined as

$$T_{ij} = -p\delta_{ij} + \mu\left(\frac{\partial u_i}{\partial x_j} + \frac{\partial u_j}{\partial x_i}\right) - \rho\overline{u_i'u_j'} . \qquad (2.32)$$

The Reynolds stresses, $-\rho\overline{u_i'u_j'}$, are obtained from Eq. (2.6), resulting in

$$T_{ij} = -p\delta_{ij} + (\mu + \mu_T)\left(\frac{\partial u_i}{\partial x_j} + \frac{\partial u_j}{\partial x_i}\right) - \frac{2}{3}\rho k\delta_{ij} . \qquad (2.33)$$

2.4.1 Inviscid Free-Surface Boundary Conditions

For inviscid flow, the molecular viscosity, μ, and the Reynolds stresses are equal to zero. The dynamic boundary condition becomes simply

$$p = p_{air} = 0 \ . \tag{2.34}$$

The corresponding piezometric pressure is

$$\psi = \rho g \beta \ . \tag{2.35}$$

For the calculation of the velocities on the free surface and in the ghost cells, a zero-gradient condition is applied

$$\frac{\partial u}{\partial n} = \frac{\partial v}{\partial n} = \frac{\partial w}{\partial n} = 0 \ , \tag{2.36}$$

where n is referred to the normal direction on the free surface. The piezometric pressure in the ghost cells is calculated according to a linear extrapolation from the pressure values of the computational domain. The flow quantities in the ghost cells are needed for the bulk-flow solution.

For viscous flow, it is common to use the same free-surface boundary conditions as for inviscid flow. Here, additional ones for the turbulence quantities must be introduced. For the turbulent kinetic energy, k, and the dissipation of the turbulent kinetic energy, ϵ, also a zero-gradient condition is applied

$$\frac{\partial k}{\partial n} = \frac{\partial \epsilon}{\partial n} = 0 \ . \tag{2.37}$$

Eqs. (2.27, 2.34 up to 2.37) are denoted as inviscid free-surface boundary conditions.

2.4.2 Viscous Free-Surface Boundary Conditions

The investigation of the influence of viscous free-surface boundary conditions on the flow, particularly on wave making, is the central topic of this work. The investigation is carried out for a two-dimensional case (Fig. 3.1). Therefore, the implementation of the respective boundary conditions is done in two dimensions. Here, the appearing flow quantities are only dependent on the time and the x- and z-coordinates. The velocity components in the y-direction are equal to zero. The kinematic boundary condition is given by Eq. (2.27). In this work, the viscous free-surface boundary conditions

are called the tangential-stress and the Reynolds-stress free-surface boundary conditions. On the free surface, the flat-surface approximation is applied giving

$$\vec{n} \approx \begin{pmatrix} 0 \\ 0 \\ 1 \end{pmatrix} , \quad \vec{t} \approx \begin{pmatrix} 1 \\ 0 \\ 0 \end{pmatrix} . \tag{2.38}$$

Tangential-Stress Free-Surface Boundary Conditions

The tangential-stress free-surface boundary conditions are obtained from Eqs. (2.31, 2.33 and 2.38). The tangential stresses on the free surface are set equal to zero giving

$$\frac{\partial u}{\partial z} = -\frac{\partial w}{\partial x} . \tag{2.39}$$

Using the continuity equation, the derivative of the velocity component, w, in the z-direction may be calculated from

$$\frac{\partial w}{\partial z} = -\frac{\partial u}{\partial x} . \tag{2.40}$$

The pressure, p, is set equal to zero, and the piezometric pressure, ψ, is obtained from Eq. (2.35). To the turbulence quantities, Eq. (2.37) is applied.

Eqs. (2.27, 2.34, 2.35, 2.37, 2.39 and 2.40) are denoted as tangential-stress free-surface boundary conditions.

Reynolds-Stress Free-Surface Boundary Conditions

The Reynolds-stress free-surface boundary conditions are obtained from Eqs. (2.30, 2.31, 2.33 and 2.38). Here, the tangential and normal stresses are set equal to zero on the free surface. The velocity derivatives in the z-direction are calculated from Eqs. (2.39 and 2.40).

The pressure on the free surface is not equal to zero anymore. It contains a contribution resulting from the molecular viscosity and the Reynolds stresses. The order of magnitude of the appearing Reynolds number is 10^6. Therefore, in the dynamic boundary condition, the influence of the molecular viscosity is assumed to be very small. Neglecting the molecular viscosity, the pressure, p, is calculated from

$$\begin{aligned} p &= 2\mu_T \frac{\partial w}{\partial z} - \frac{2}{3}\rho k \\ &= -2\mu_T \frac{\partial u}{\partial x} - \frac{2}{3}\rho k . \end{aligned} \tag{2.41}$$

The corresponding piezometric pressure, ψ, is

$$
\begin{aligned}
\psi &= p + \rho g \beta \\
&= -2\mu_T \frac{\partial u}{\partial x} - \frac{2}{3}\rho k + \rho g \beta \; .
\end{aligned} \tag{2.42}
$$

Eqs. (2.27, 2.37, 2.39 up to 2.42) are denoted as Reynolds-stress free-surface boundary conditions.

2.4.3 Alternative Inviscid Free-Surface Boundary Conditions

The currently implemented inviscid mirror free-surface boundary conditions (see Section 2.4.4) give a dampened wave profile, which is physically not correct. Therefore, three alternative approaches regarding the inviscid free-surface boundary conditions are implemented and investigated. As in the case of the viscous free-surface boundary conditions, the implementation is carried out in two dimensions.

Inviscid Irrotational Free-Surface Boundary Conditions

Considering Eq. (2.36), it may be concluded that the flow at the free surface is irrotational. For irrotational flow, the vorticity vector, $\vec{\gamma}$, must be equal to a zero vector. This is the case when

$$
\vec{\gamma} = \nabla \times \vec{V} = \vec{0} \; , \tag{2.43}
$$

where ∇ is the nabla operator. In the given two-dimensional x-z-coordinate system, the flow is irrotational when

$$
\frac{\partial u}{\partial z} = \frac{\partial w}{\partial x} \; . \tag{2.44}
$$

In this work, Eqs. (2.27, 2.34, 2.35, 2.37, 2.40 and 2.44) are denoted as inviscid irrotational free-surface boundary conditions, which are consistent with the ones for potential flow.

Inviscid Flat Free-Surface Boundary Conditions

Using a flat free-surface approximation and the assumption that the normal and tangential gradients of the normal velocity are negligible, the inviscid

flat free-surface boundary conditions are obtained, *Choi and Stern (1993)*. The velocity gradients in the z-direction are simply set to zero giving

$$\frac{\partial u}{\partial z} = \frac{\partial w}{\partial z} = 0 \ . \tag{2.45}$$

In this work, Eqs. (2.27, 2.34, 2.35, 2.37 and 2.45) are denoted as inviscid flat free-surface boundary conditions.

Inviscid Flat-Continuity Free-Surface Boundary Conditions

Taking the continuity equation into consideration, a physically more correct relation for the inviscid flat free-surface boundary conditions may be obtained, *Stern et al. (1996)*. This gives

$$\frac{\partial u}{\partial z} = 0 \ , \tag{2.46}$$

and

$$\frac{\partial w}{\partial z} = -\frac{\partial u}{\partial x} \ . \tag{2.47}$$

In this work, Eqs. (2.27, 2.34, 2.35, 2.37, 2.46 and 2.47) are denoted as inviscid flat-continuity free-surface boundary conditions.

2.4.4 Implementation of the Free-Surface Boundary Conditions

Implementation of the Inviscid Mirror Free-Surface Boundary Conditions

In the current version of FINFLO, Eq. (2.36) has been already implemented by Tom Sundell, *Mikkola (1999)*, in the following way:

$$u_{FS} = \frac{9u_k - u_{k-1}}{8} \ , \quad v_{FS} = \frac{9v_k - v_{k-1}}{8} \ , \quad w_{FS} = \frac{9w_k - w_{k-1}}{8} \ , \tag{2.48}$$

where u_{FS}, v_{FS} and w_{FS} are the velocity components in the x-, y- and z-directions on the free surface. The subscribts, k and $k-1$, are referred to the centres of the the first and second cells below the free surface (Fig. 2.1). The indices, i and j, have been dropped for simplicity, e.g. $u_{i,j,k} = u_k$. Eq. (2.48) is obtained from Eq. (2.26) by setting $(\partial\Phi/\partial y_n)_{wall}$ equal to zero.

Knowing the free-surface velocities, the new wave height, β, may be calculated from Eq. (2.27). Eq. (2.35) is applied to the calculation of the
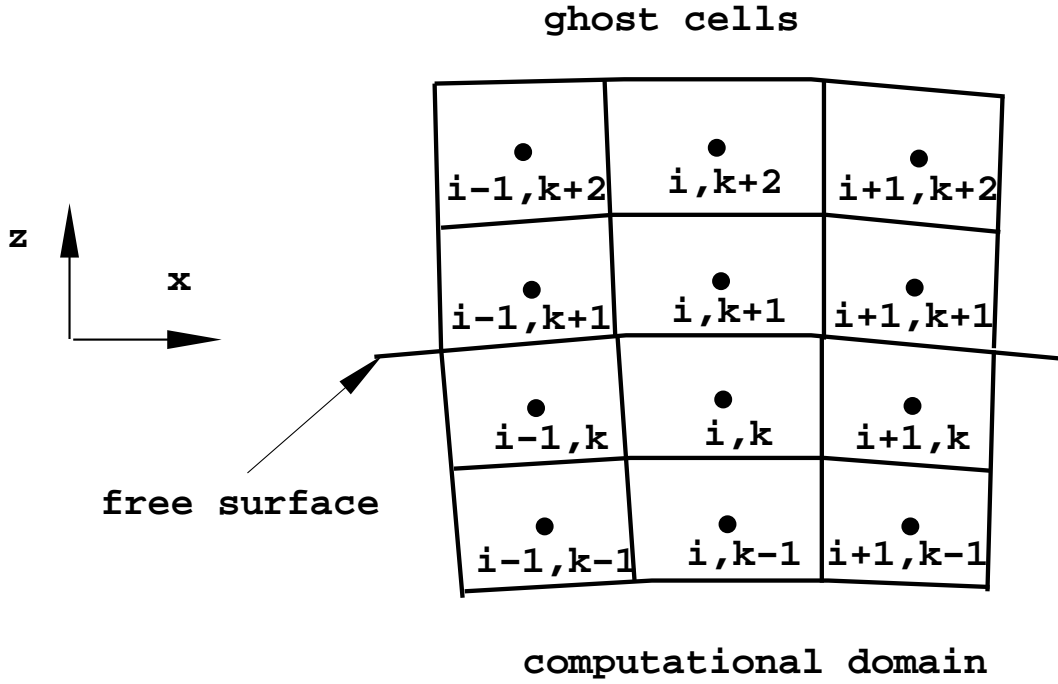
ghost cells

computational domain

Fig. 2.1: Naming of the cells associated with the free surface in a two-dimensional coordinate system.

piezometric pressure on the free surface. The piezometric pressure in the ghost cells is set according to a linear extrapolation giving:

$$\psi_{k+1} = 2\rho g\beta - \psi_k \ , \tag{2.49}$$

$$\psi_{k+2} = 2\psi_{k+1} - \psi_k \ , \tag{2.50}$$

where the subscripts, $k + 1$ and $k + 2$, are referred to the centres of the first and second cells above the free surface (Fig. 2.1). These cells are called ghost cells. Eqs. (2.49 and 2.50) are obtained from a Taylor-series expansion.

Having linearly extrapolated the piezometric pressure from the computational domain to the ghost cells, the respective velocities in the ghost cells are set according to

$$u_{k+1} = u_k \ , \quad v_{k+1} = v_k \ , \quad w_{k+1} = w_k \ , \tag{2.51}$$

$$u_{k+2} = u_{k-1} \ , \quad v_{k+2} = v_{k-1} \ , \quad w_{k+2} = w_{k-1} \ . \tag{2.52}$$

Similarly, the respective values for the turbulence quantities, k and ϵ are set according to

$$k_{k+1} = k_k \ , \quad \epsilon_{k+1} = \epsilon_k \ , \quad k_{k+2} = k_{k-1} \ , \quad \epsilon_{k+2} = \epsilon_{k-1} \ . \tag{2.53}$$

Implementation of the Tangential-Stress Free-Surface Boundary Conditions

The tangential-stress free-surface boundary conditions are realized in the following way.

Using Eq. (2.39), the velocity component in the x-direction on the free surface is derived from

$$u_{FS} = u_{i,k} - \frac{(w_{i,k} - w_{i-1,k})}{(x_{i,k} - x_{i-1,k})} \frac{(z_{i,k+1} - z_{i,k})}{2} \ , \tag{2.54}$$

where x and z are the x- and z-coordinates of the respective cell centre. The subscripts are referred to the cell centres according to Fig. 2.1.

Using Eq. (2.40), the velocity component in the z-direction on the free surface is derived from

$$w_{FS} = w_{i,k} - \frac{(u_{i,k} - u_{i-1,k})}{(x_{i,k} - x_{i-1,k})} \frac{(z_{i,k+1} - z_{i,k})}{2} \ . \tag{2.55}$$

In Eqs. (2.54 and 2.55), a two-point upwind scheme of first-order accuracy is applied to the calculation of the velocity derivatives in the x-direction. It is obtained from a Taylor-series expansion. One computation is carried out using a central-difference scheme of second-order accuracy for the calculation of the velocity derivatives in the x-direction. This scheme is obtained again from a Taylor-series expansion. Eqs. (2.54 and 2.55) become

$$u_{FS} = u_{i,k} - \frac{(w_{i+1,k} - w_{i-1,k})}{(x_{i+1,k} - x_{i-1,k})} \frac{(z_{i,k+1} - z_{i,k})}{2} \ , \tag{2.56}$$

$$w_{FS} = w_{i,k} - \frac{(u_{i+1,k} - u_{i-1,k})}{(x_{i+1,k} - x_{i-1,k})} \frac{(z_{i,k+1} - z_{i,k})}{2} \ . \tag{2.57}$$

Both schemes give results of the same accuracy (Fig. 4.12). Therefore, the two-point upwind scheme is applied to all computed cases.

The piezometric pressure and the turbulence quantities in the ghost cells are set according to Eqs. (2.49, 2.50 and 2.53).

The velocities in the ghost cells are obtained from a linear extrapolation given by

$$u_{i,k+1} = 2u_{FS} - u_{i,k} \ , \quad w_{i,k+1} = 2w_{FS} - w_{i,k} \ , \tag{2.58}$$

$$u_{i,k+2} = 2u_{i,k+1} - u_{i,k} \ , \quad w_{i,k+2} = 2w_{i,k+1} - w_{i,k} \ . \tag{2.59}$$

Implementation of the Reynolds-Stress Free-Surface Boundary Conditions

Using Eq. (2.42) and a linear extrapolation, the piezometric pressure in the ghost cells is set to

$$\psi_{i,k+1} = 2\left(-2\mu_T\frac{(u_{i,k}-u_{i-1,k})}{(x_{i,k}-x_{i-1,k})} - \frac{2}{3}\rho k + \rho g\beta\right) - \psi_{i,k} , \qquad (2.60)$$

$$\psi_{i,k+2} = 2\psi_{i,k+1} - \psi_{i,k} . \qquad (2.61)$$

The velocities on the free surface and in the ghost cells are calculated from Eqs. (2.54, 2.55, 2.58 and 2.59).

To the turbulence quantities, Eq. (2.53) is applied.

Implementation of the Inviscid Irrotational Free-Surface Boundary Conditions

Using Eq. (2.44), the velocity component in the x-direction on the free surface is calculated as

$$u_{FS} = u_{i,k} + \frac{(w_{i,k}-w_{i-1,k})}{(x_{i,k}-x_{i-1,k})}\frac{(z_{i,k+1}-z_{i,k})}{2} . \qquad (2.62)$$

The velocity component in the z-direction on the free surface is derived from Eq. (2.55). The velocity components in the ghost cells are set according to Eqs. (2.58 and 2.59). To the piezometric pressure and the turbulence quantities in the ghost cells, Eqs. (2.49, 2.50 and 2.53) are applied.

Implementation of the Inviscid Flat Free-Surface Boundary Conditions

In FINFLO, Eq. (2.45) is realized as follows:

$$u_{FS} = u_{i,k} , \quad w_{FS} = w_{i,k} . \qquad (2.63)$$

In the ghost cells, the velocity components, the piezometric pressure and the turbulence quantities are set according to Eqs. (2.58, 2.59, 2.49, 2.50 and 2.53).

Implementation of the Inviscid Flat-Continuity Free-Surface Boundary Conditions

Using Eqs. (2.46 and 2.47), the velocity components on the free surface are obtained from

$$u_{FS} = u_{i,k} , \qquad (2.64)$$

$$w_{FS} \;=\; w_{i,k} - \frac{\left(u_{i,k} - u_{i-1,k}\right)}{\left(x_{i,k} - x_{i-1,k}\right)} \frac{\left(z_{i,k+1} - z_{i,k}\right)}{2} \;. \tag{2.65}$$

In the ghost cells, the velocity components, the piezometric pressure and the turbulence quantities are set according to Eqs. (2.58, 2.59, 2.49, 2.50 and 2.53).

3 Computations

The computations are carried out on the Silicon Graphics Origin 2000/128 computer of the Center for Scientific Computing, *Fagerholm and Haataja (1999)*. It consists of 128 MIPS R12000 processors. The theoretical performance power of one processor is 600 Mflop/s. The central memory of the computer accounts for 160 GB.

For the computations, the maximum memory request is about 170 MB of the central memory. At model scale, the solution is converged after about 75000 iterations. At full-scale, the computations are carried out in three stages. First, the first two crests of the transom wave are computed in the same way as at model scale. Due to difficulties associated with Chien's turbulence model and oscillations of the free surface at the transom, the computations are terminated. In the second stage, using the obtained grid (Fig. 3.4), the computations are started from the beginning, and the free surface is kept fixed. The respective solution is converged after about 100000 iterations. In the third stage, the free surface is allowed to deform giving a converged solution after further 50000 iterations. In this way, no oscillations of the free surface close to the transom appear, and a rather large time step may be used in order to get the entire wave pattern within a reasonable time.

At model scale, using the coarser grids, it takes about 7.5 CPU-seconds for one iteration cycle. For the finest grid and the investigation of the side influence on the results, it takes about 17 CPU-seconds for one iteration cycle. At full scale, using the grid, ROUGHFSC, it takes about 2 CPU-seconds for one iteration cycle. For the grid, FINEFSC, it takes about 11 CPU-seconds for one iteration cycle.

3.1 Computed Case

The computed cases are numerical simulations of inviscid and viscous flows around the model, *Ile*. The geometry of this model is given in Fig. 3.1.

The model is assumed to be infinitely wide in the y-direction. Therefore, the appearing flow may be considered as two-dimensional. The shape of the bow is a circle segment with radius, R, and the bottom is flat. The transom is located at the origin of the global Cartesian coordinate system. Its x-axis, determining the still water level, is directed from the transom in flow direction. The z-axis is directed upwards from the still water level. The direction of the y-axis is given by the right-hand rule. At the bow, the formation of the bow wave is suppressed. At the transom, the wave height of the free surface is set equal to the draught, T. Downstream of the transom, the free surface may be deformed arbitrarily. The appearance of sinkage and trim is suppressed.

At model scale, the geometrical dimensions of the investigated model are:

- Length overall, $L = 2.000$ m

- Radius, $R = 1.450$ m

- Draught, $T = 0.100$ m

In the cases, LONG1 and LONG2, the length of the flat bottom is increased to 4.479 m and 7.959 m, respectively. The other geometrical dimensions remain unchanged.

At full scale, the geometrical dimensions of the investigated model are:

- Length overall, $L = 80.000$ m

- Radius, $R = 58.000$ m

- Draught, $T = 4.000$ m

- Scale, $\lambda = 40$

The length of the flat plate (FLATR, FLATF and FLATFST) is equal to the length between the perpendiculars, L_{pp}, at full scale. At full scale, $L_{pp} = 61.16$ m.

The computations are carried out at four Froude numbers based on the draught, T, of the model. The Froude numbers are defined as

$$Fn_T = \frac{U_\infty}{\sqrt{gT}} \ , \tag{3.1}$$

where U_∞ is the free stream velocity. They account for 2.1, 2.2, 2.3 and 2.8, respectively.

The wave formation behind the model, *Ile*, has been investigated by *Saisto (1995 and 2000)*. He solved the potential flow in two dimensions using the boundary element method. In his work, he carried out also several model tests at different Froude numbers in order to measure the transom wave. The resistance coefficient of the model has been evaluated by *Aho and Schweighofer (1995)* in a laboratory exercise. There, the forces acting on a moving slice of the model (Fig. 3.1) were measured. The width of the slice was $B = 0.370$ m. In the model tests, the model was kept fixed on an even keel. These results are used in the validation of the computations and the discussion of the computed resistance coefficient.
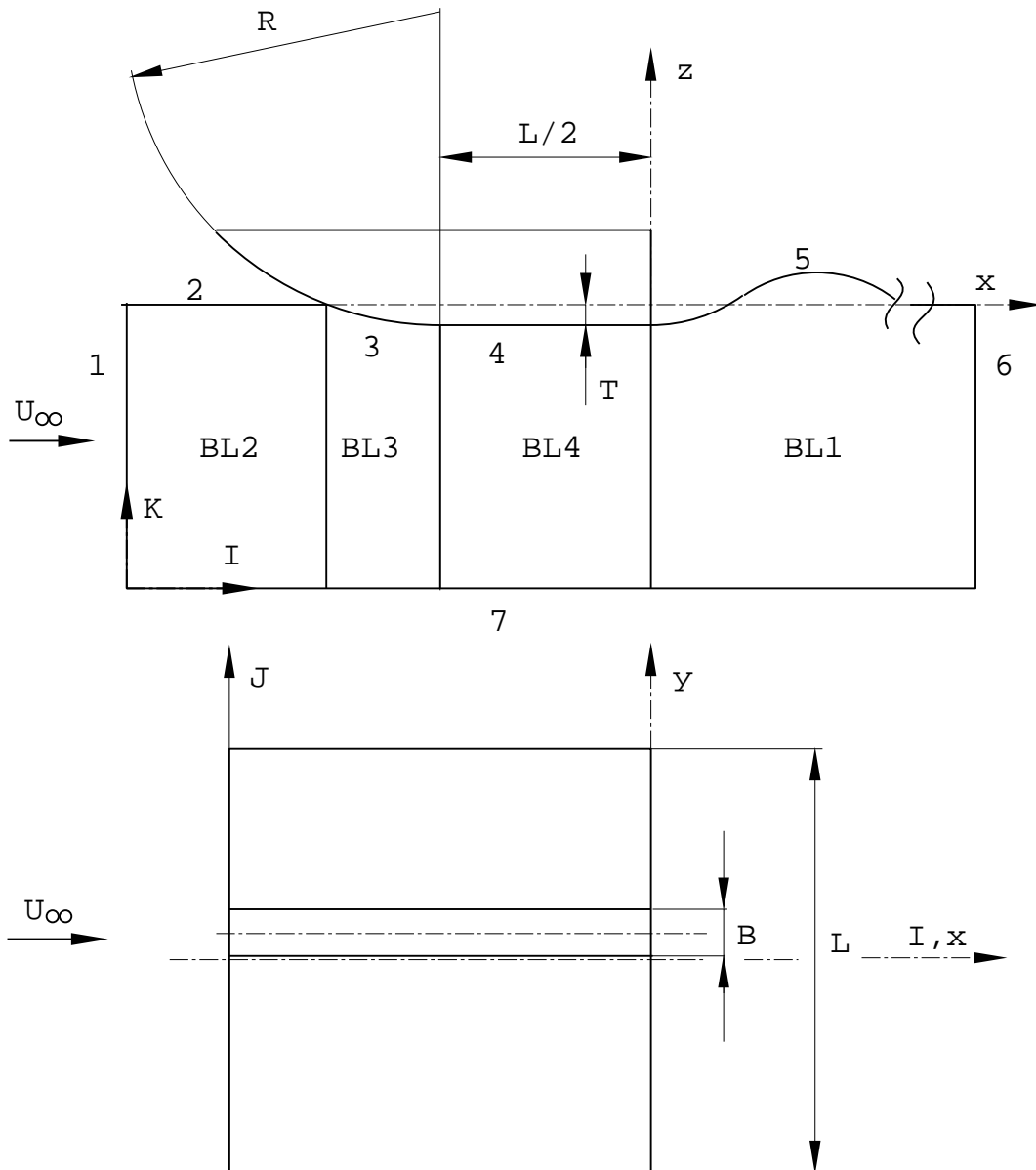
Fig. 3.1: Computed case, *Ile*. **Top:** Used coordinate systems. Subdivision of the computational domain into four blocks: BL2, BL3, BL4 and BL1. **Bottom:** Experimental arrangement.

3.2   Grid
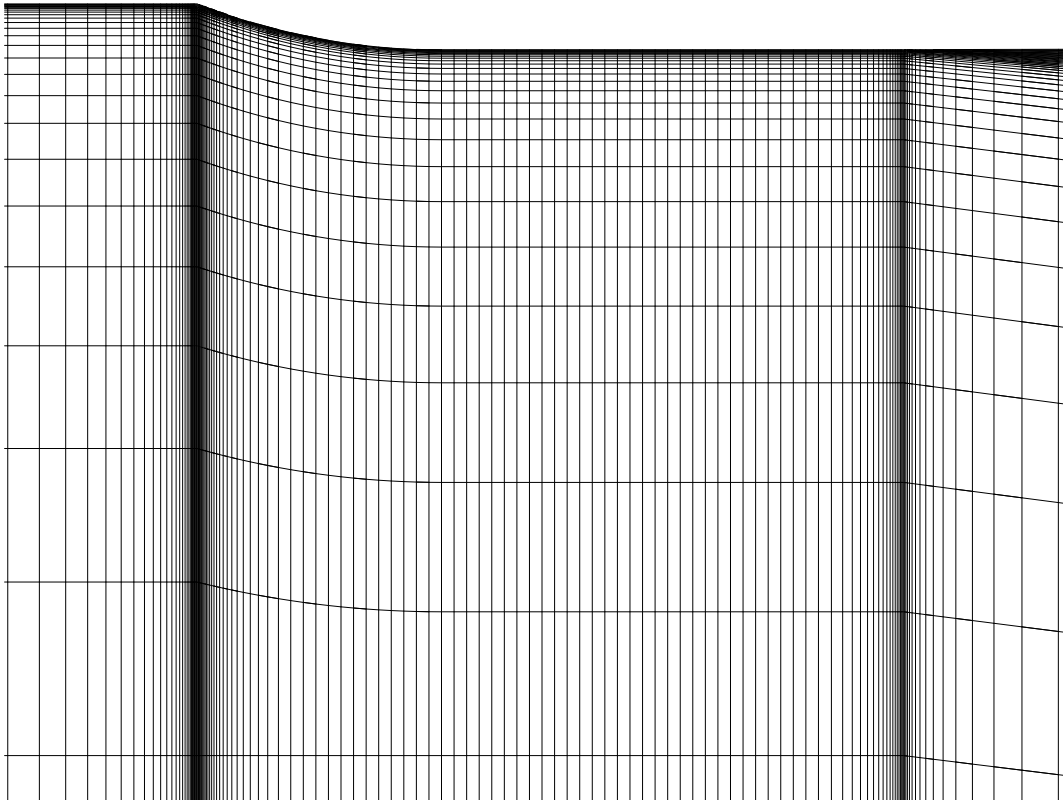
Fig. 3.2: The grid, FINE, of the computed case, *Ile*. Region around the model.

In order to get appropriate grids for the computations, numerous generated grids must be tested. The shape of the calculated case may be described analytically. Therefore, a separate code is written for the grid generation. The high resolution of the grids close to the free surface causes the appearance of negative cells when the grid starts to move from the initial position. Generally, the volume of the cells is calculated from the coordinates of their corner and centre points using the vector analysis. In cases of strong deformations of the cells, the appearing vector products, and therefore also the volumes, may become negative resulting in unstable solutions and a terminated computation. In the beginning of this investigation,
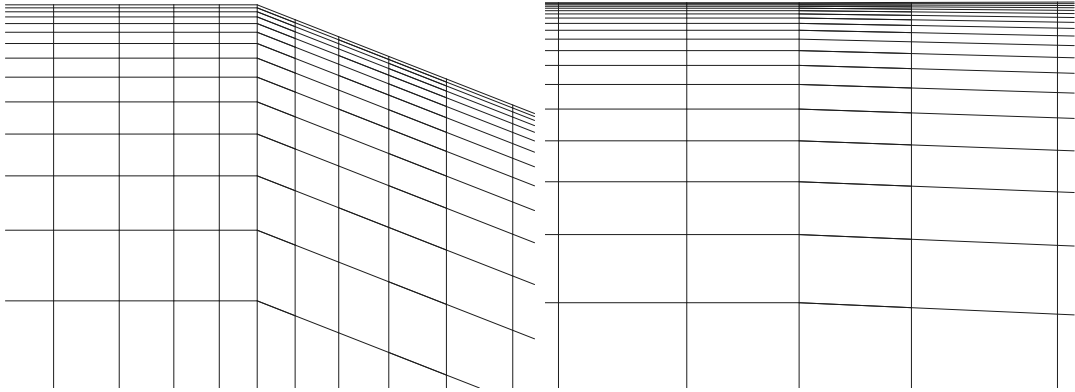
Fig. 3.3: Zoomed grid, FINE, of the computed case, *Ile.* **Left**: Bow region. **Right**: Transom region.

the negative volumes are due to the extremely thin cells at the free surface which merge into one at certain locations. Stable solutions are obtained with the grids: FINE, FINETRANSOM, LONG1, LONG2, SIDE, FINEST, FINEFSC and ROUGHFSC. At full scale, the grids are manually manipulated using the commercial grid-generation software, IGG 3.7, *NUMECA INTERNATIONAL (1999).*

3.2.1 FINE

The grid, FINE, consists of four blocks (Figs. 3.1 and 3.2). The block, BL2, is composed of $64 \times 1 \times 64$ cells in the i-, j- and k-directions, respectively. Side one is located at 20.00 m upstream from the origin of the global Cartesian coordinate system. Therefore, the length of the inflow region is about $9L$. The width of the block, BL2, accounts for 1 m, and its draught from the still-water level is $5L = 10$ m. The expected wave length is about $2.5L$. Therefore, the draught should be sufficient in order to avoid the appearance of shallow water effects. In order to capture the pressure peak at the bow, the grid is very fine there. In the computed cases, the blocks are connected to each other exactly node by node (Fig. 3.3). Therefore, the fine resolution of the grid in the boundary layer is continued in the block, BL2, close to the still-water level. The length of the first cell at the bow is 0.0002 m, and its height is 8×10^{-6} m. In this way, the nondimensional distance of the first node from the wall, y^+, remains always below the value, four. Almost everywhere

at the wall, the nondimensional distance of the first node, y^+, accounts for about 0.7. This holds for the Froude numbers, Fn_T, equal to 2.1, 2.2, 2.3 and 2.8 of the investigations. Starting from the bow in upstream direction and the still-water level in negative z-direction, the length and height of the cells are increased by not more than 30 percent until an equal distribution of the remaining cells is obtained. The block, BL3, consists of $48 \times 1 \times 64$ cells in the i-, j- and k-directions, respectively. The length of the first cell at the bow is equal to the one of the adjacent cell in the block, BL2. The nodes on the left and the right sides of block, BL3, are connected by circle segments with increasing radii, R. Apart from this feature, the block, BL3, is built up in the same manner as the block, BL2. The block, BL4, is composed of $48 \times 1 \times 64$ cells in the i-, j- and k-directions, respectively. At the transom, turbulence and bigger changes of the velocity and the pressure might appear. Therefore, the mesh is quite fine there. The length of the first cell at the transom is equal to 0.002 m. Also, the block, BL4, is composed in the same manner as the block, BL2. Here, the length of the first cell at the shoulder is equal to the one of the adjacent cell in the block, BL3. The block, BL1, consists of $384 \times 1 \times 64$ cells in the i-, j- and k-directions, respectively. The length of the first cell at the transom is equal to the one of the adjacent cell in the block, BL4. The length of the following cells is increased by not more than 30 percent in the flow direction until an equal distribution of the remaining cells is obtained. Side six of the block, BL1, is located at 40 m downstream from the origin of the global Cartesian coordinate system. Therefore, the length of the wake region accounts for 20 L. For the Froude numbers, $Fn_T = 2.1$, 2.2, 2.3 and 2.8, the waves are resolved by at least 24, 27, 30 and 45 equally distributed cells per wave length, respectively. The resolution of the boundary layer is continued in the block, BL1. In this way, the influence of the convected boundary layer on the appearing transom waves may be captured. Nevertheless, farther downstream the grid becomes coarser. On side six, the cells are equally distributed from the still-water level in the negative z-direction. The nodes on the left and the right sides of the block, BL1, are connected to each other by straight lines.

3.2.2 FINETRANSOM

The grid, FINETRANSOM, is identical with the grid, FINE. Only the resolution at the transom is higher. The length of the first cell at the transom in the blocks, BL4 and BL1, is 0.00053 m.

3.2.3 LONG1 and LONG2

The grids, LONG1 and LONG2, are also identical with the grid, FINE. Only the block, BL4, is different in the way that it is 4.479 m and 7.959 m long, respectively. The length of the block, BL4, is increased by adding a certain amount of cells with constant length to the original block. The block, BL4, of the grid LONG1, consists of $176 \times 1 \times 64$ cells in the i-, j- and k-directions, respectively. The one of the grid, LONG2, is composed of $304 \times 1 \times 64$ cells in the i-, j- and k-directions, respectively. The blocks, BL2 and BL3, are shifted in the upstream direction.

3.2.4 SIDE

The grid, SIDE, is identical with the grid, LONG2. Only, in the negative z-direction, 64 cells of constant height are added to the ones of LONG2, giving 128 cells in the k-direction. Side seven is shifted to 34.357 m below the still water level, which accounts for about $14L$.

3.2.5 FINEST

The grid, FINEST, is composed in the same manner as the grid, FINE. The geometrical main dimensions of the computational domain remain unchanged. The grid, FINEST, consists of 1×96 cells in the j- and k-directions, respectively. In the i-direction, the blocks, BL2, BL3, BL4 and BL1, are built up of 96, 72, 96 and 576 cells, respectively. The length of the first cell at the bow is reduced to 0.0001 m. At the transom, it accounts for 0.001 m. The height of the first cell at the wall is the same as in the grid, FINE. For the Froude number, $Fn_T = 2.8$, the waves are resolved by at least 70 equally distributed cells per wave length.

3.2.6 FINEFSC and ROUGHFSC

The grid, FINEFSC, consists of 1×96 cells in the j- and k-directions, respectively. In the i-direction, the blocks, BL2, BL3, BL4 and BL1, are built up of 64, 48, 48 and 384 cells, respectively. It is obtained from the grid, FINE, by scaling. The scale, λ, is equal to 40. The resolution in the i-direction is the same as in the grid, FINE. Nevertheless, in the k-direction, the resolution is different due to the thinner boundary layer with respect to the draught and the requested distance of the first node from the wall. The distance of the first node from the wall is 4.2×10^{-6} m. In this way, the nondimensional distance of the first node from the wall, y^+, remains below

the value, 2.5. Almost everywhere at the wall, the nondimensional distance of the first node, y^+, accounts for about 2.0. In the block, BL1, two wave crests are presented (Fig. 3.4). They are obtained from laborious, time consuming computations, where the upper boundary of the block, BL1, was a flat plane in the beginning, similar to the ones at model scale. The different resolution in the k-direction and the slightly different structure cause a higher degree of the nonorthogonality in the grid, FINEFSC, compared with the grid, FINE. The resolution of the waves is the same as for the the grid, FINE.

The grid, ROUGHFSC, corresponds to the second level of the grid, FINE-FSC. In the i-direction, the length of one cell is equal to the one of two adjacent cells of the grid, FINEFSC. Similarly, in the k-direction, the height of one cell is equal to the one of two adjacent cells of the grid, FINEFSC. The grid, ROUGHFSC, consists of 1×48 cells in the j- and k-directions, respectively. In the i-direction, the blocks, BL2, BL3, BL4 and BL1, are built up of 32, 24, 24 and 192 cells, respectively. The waves are resolved by at least 23 equally distributed cells per wave length.

3.2.7 FLATR, FLATF and FLATFST

At full scale, the validation is performed by computing the turbulent flow over a flat plate. The used grids are FLATR, FLATF and FLATFST in the order of their coarseness.

FLATR ist the coarsest grid. In the same manner as the grid, FINE, the computational domain is subdivided into the blocks, BL2, BL3, BL4 and BL1. It consists of 1×48 cells in the j- and k-directions, respectively. In the i-direction, the blocks, BL2, BL3, BL4 and BL1, are built up of 32, 24, 24 and 192 cells, respectively. The grid, FLATR, corresponds to the second level of the grid, FLATF. In the i-direction, the length of one cell is equal to the one of two adjacent cells of the grid, FLATF. Similarly, in the k-direction, the height of one cell is equal to the one of two adjacent cells of the grid, FLATF.

The grid, FLATF, consists of 1×96 cells in the j- and k-directions, respectively. In the i-direction, the blocks, BL2, BL3, BL4 and BL1, are built up of 64, 48, 48 and 384 cells, respectively. In the i-direction, the resolution is exactly the same as the one of the grid, FINEFSC. Also the dimensions of the computational domain are exactly the same. The flat plate is located at the still-water level where the z-coordinate is equal to zero. Naturally, the upper boundary of the block, BL1, is a plane at the still-water level. Therefore, in the k-direction, the resolution is slightly different from the one of the grid, FINEFSC. The distance of the first node from the
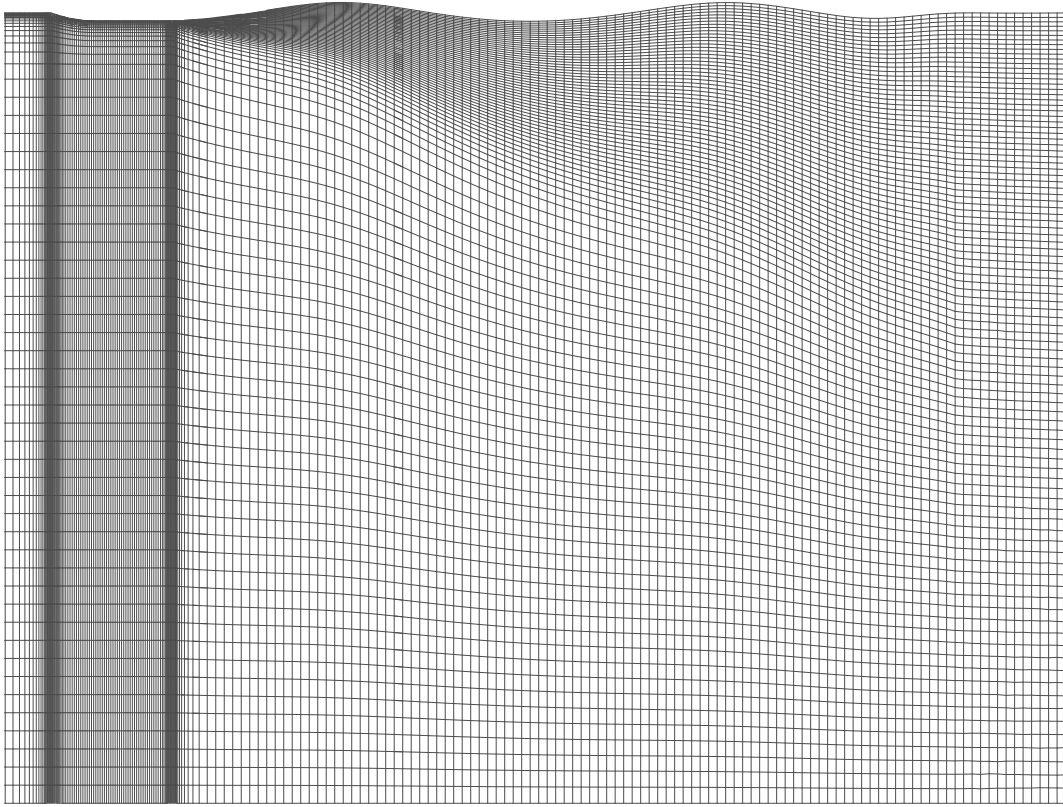
Fig. 3.4: The grid, FINEFSC, of the computed case, *Ile*. Region around the model.

wall is 4.2×10^{-6} m. In this way, the nondimensional distance of the first node from the wall, y^+, remains below the value, 3.7. Almost everywhere at the wall, the nondimensional distance of the first node, y^+, accounts for about 2.0.

The grid, FLATFST, is the finest grid (Fig. 3.5). It consists of 1×192 cells in the j- and k-directions, respectively, giving an significantly improved resolution of the boundary layer. In the i-direction, the blocks, BL2, BL3, BL4 and BL1, are built up of 64, 48, 48 and 128 cells, respectively. The dimensions of the computational domain are the same as the ones of the grid, FLATF. The distance of the first node from the wall is 5.0×10^{-6} m. In this way, the nondimensional distance of the first node from the wall, y^+, remains below the value, 4.2. Almost everywhere at the wall, the nondimensional

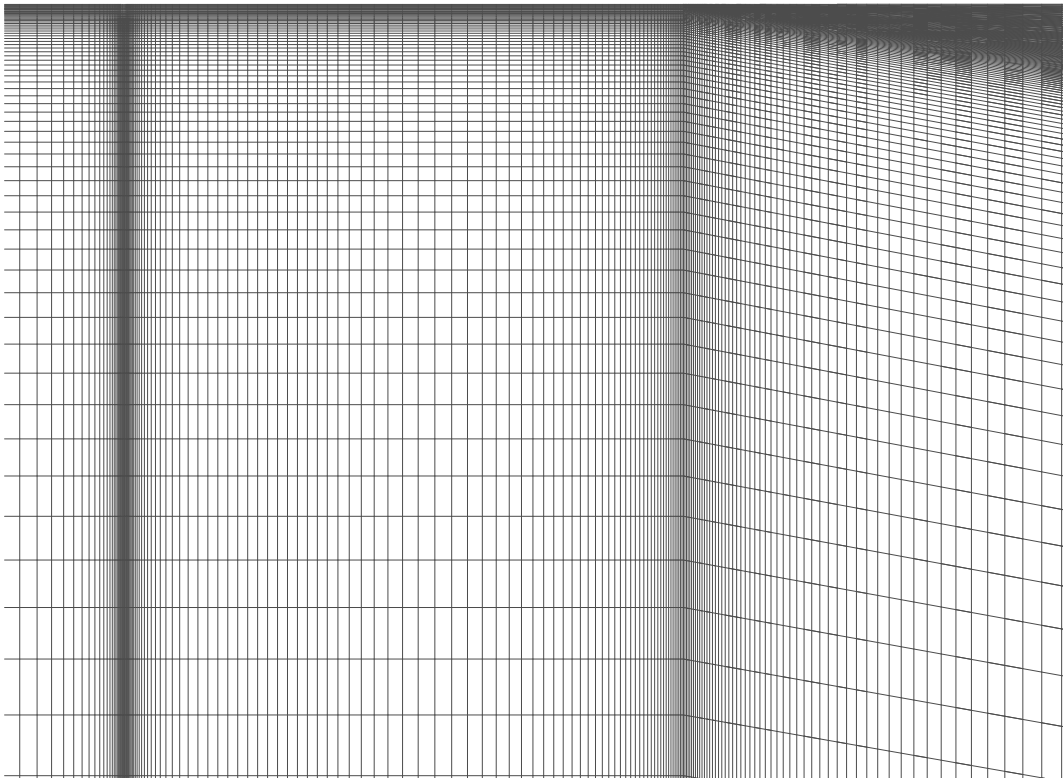distance of the first node, y^+, accounts for about 2.2.

Fig. 3.5: The grid, FLATFST, used for the flat-plate computations at the full-scale ship Reynolds number. Region around the flat plate.

3.3 Initial Values and Boundary Conditions

3.3.1 Model-Scale Computations

For the Froude numbers, $Fn_T = 2.1$, 2.2, 2.3 and 2.8, the corresponding Reynolds numbers of the computations, $Re_l = U_\infty \times L_{pp}/\nu$, account for 2.8×10^6, 2.933×10^6, 3.066×10^6 and 3.732×10^6, respectively. The length between the perpendiculars, L_{pp}, is 1.529 m. The free-stream velocity, U_∞, is set to 2.080 m/s, 2.179 m/s, 2.278 m/s and 2.773 m/s with respect to the respective Froude number. The reference area is used in the calculation of the drag coefficient, C_D. It is equal to 1.541 m². The Mach number is equal to zero, and the density is 999.4 kg/m³. The initial values of the turbulence level and the nondimensional turbulence coefficient, μ_T/μ, are set to 0.02 and 10.00 in the input. The free-stream turbulence level and the nondimensional free-stream turbulence coefficient, $\mu_{T\infty}/\mu$, are set to 0.001 and 0.01, respectively. The maximum nondimensional turbulence coefficient is set to the very high value of 5000. Therefore, the nondimensional turbulence coefficient may be regarded as unrestricted. The turbulence coefficients are made nondimensional by referring them to the molecular viscosity. The Courant number is set to either three or five. The lower value is used for the computations at the Froude number, 2.1. In the free-surface evaluation, the maximum time step is calculated from

$$\Delta t_{max} = \frac{DTWMAX}{|\vec{V}|} \ ,$$ (3.2)

where DTWMAX accounts for 0.0005 for the computations at the Froude numbers, 2.2, 2.3 and 2.8. For the grid, FINETRANSOM, DTWMAX must be reduced to 0.0003 in order to obtain a converged solution. At the Froude number, 2.1, DTWMAX must further be reduced to 0.0001 in the beginning and to 0.00005 in the end. $\vec{V}$ is the velocity vector consisting of the velocity components at the respective cell centres of the first cell row below the free surface.

A brief explanation of the used boundary conditions is given in Sections 2.3 and 2.4. They are applied on the boundaries of the computational domain described in Fig. 3.1. The sides, one and six, are defined as inflow and outflow boundaries. Here, the external boundary condition is applied. The sides, two and seven, as well as the sides normal to the y-axis are defined as symmetry planes. Here, the mirror boundary condition is applied. The sides, three and four, are defined as solid walls, and the side, five, is defined as free surface.

3.3.2 Full-Scale Computations

The full-scale computations are performed at the Froude number, $Fn_T = 2.8$, and the full-scale ship Reynolds number, $\mathrm{Re}_l = 9.442 \times 10^8$. The length between the perpendiculars, L_{pp}, is 61.16 m. The free-stream velocity, U_∞, is set to 17.538 m/s. The reference area is equal to 2465.6 m^2. The Mach number is equal to zero, and the density is 999.4 kg/m^3. The intial values of the turbulence level and the nondimensional turbulence coefficient, μ_T/μ, are set to 0.02 and 10.00 in the input. The free-stream turbulence level and the nondimensional free-stream turbulence coefficient, $\mu_{T\infty}/\mu$, are set to 0.001 and 16.5, respectively. The maximum nondimensional turbulence coefficient is set to 5000000 in order to avoid any restrictions of the turbulence coefficient. The free-stream dissipation of the turbulent kinetic energy is the same as the one at model scale within a range of about two percent. The Courant number is set either to two or three. The lower value is applied for the computations using the grid, ROUGHFSC, and the higher one is applied for the computations using the grid, FINEFSC. The maximum time step, DTWMAX, accounts for 0.01 in the beginning and for 0.0001 in the end.

On the boundaries of the computational domain, the same boundary conditions are applied as at model scale.

The investigation of the efficiency of multigridding at full scale is conducted under the same conditions as the full-scale computations of the model, *Ile*. Nevertheless, the Courant number on the finest level is set to 5, and the one on the coarser level is set to 7.5. The side, five, of the grid, FINEFSC, is not defined as free-surface anymore (Figs. 3.1 and 3.4). It is kept fixed, and the mirror boundary condition is applied there.

3.3.3 Flat-Plate Computations

The computations of the turbulent flow over the flat plate are carried out under the same conditions as the full-scale computations of the model, *Ile*. Nevertheless, the nondimensional free-stream turbulence coefficient, $\mu_{T\infty}/\mu$, is set alternatively to 0.01, 1 and 16.5, and the free-stream turbulence level is set to 0.001. Additionally, one computation is performed where the nondimensional free-stream turbulence coefficient and the free-stream turbulence level are set to 0.01 and 0.000157, respectively. The side, five, is defined as symmetry plane, where the mirror boundary condition is applied. For the grids, FLATR, FLATF and FLATFST, the Courant numbers are set to two, five and four, respectively. The reference area is equal to 2446.4 m^2.

4 Results

In this chapter, the computed results for the test case, *Ile*, are presented. In the beginning, the validation of the numerical method is carried out followed by the analysis. The *ITTC - Quality Manual (1999)* distinguishes between verification and validation. Verification is a process where the numerical error of the respective simulation due to the grid and the convergence is estimated. Knowing the numerical and experimental errors, the validation may be carried out by comparing the results of the simulations with the ones of experiments giving the modelling error. In this work, the applicability of the experimental results is considered as limited due to the code, the experimental arrangement and the appearing full-scale ship Reynolds number. Therefore, also theoretical and computational results obtained by different authors in association with qualitative observations are used for validation purposes. Nevertheless, experimental results are used as far as possible.

4.1 Validation

In this investigation, several approaches with respect to the evaluation of the free surface are implemented into the incompressible version of the Navier-Stokes solver, FINFLO. The code has been widely validated for turbulent ship flows at model scale, *Järvinen (2000), Li (2002), Mikkola (2002), Niittymäki (2001)*. The first time, computations are carried out at full-scale ship Reynolds numbers. Therefore, the validation has to be performed with respect to the evaluation of the free surface and full-scale computations.

4.1.1 Free Surface

Regarding the evaluation of the free surface, the validation is performed using the analytical wave length of a wave in deep water, the results presented by

Vanden-Brock (1980) and the ones obtained from model tests and potential-flow computations, *Saisto (1995 and 2000)*.

Analytical Wave Length

According to the linear wave theory, the length of a two-dimensional wave in deep water, λ, may be given by, *The Society of Naval Architects and Marine Engineers (1988)*,

$$\lambda = \frac{2\pi U_\infty^2}{g} \ .$$
(4.1)

Here, the flow is assumed to be incompressible and inviscid. The motion of the fluid particles is characterized by an appropriate velocity potential resulting in sinusoidal waves. Eq. (4.1) holds also for the transversal waves at a distance of about two wave lengths behind a ship. Closer to the stern they become little shorter.

A more accurate theoretical relation for the wave length of nonlinear transom waves is given by *Vanden-Brock (1980)*. There, the flow is assumed to be incompressible, inviscid and irrotational. The waves are not sinusoidal anymore.

Due to three-dimensional influences, the length of the measured wave profile cannot be used.

In Table 1, the wave lengths of the computed transom waves are compared with the ones obtained from Eq. (4.1) and given by *Vanden-Broeck (1980)*. The results of Vanden-Broeck are taken as reference wave-lengths.

The analytical solution according to Eq. (4.1) gives a greater wave length than the one obtained by Vanden-Broeck. This may be traced to the circumstance that the analytical solution is based on the assumption of sinusoidal waves, and the linearized free-surface boundary conditions are applied on the still-water level.

For the Froude number, $Fn_T = 2.8$, the wave-length solutions are almost independent of the grid resolution. Solving the Euler equations with the inviscid mirror free-surface boundary conditions gives the greatest deviation compared with the result of Vanden-Broeck. Using the inviscid irrotational and viscous free-surface boundary conditions, the results are almost exactly the same as the one of Vanden-Broeck.

Table 1: Wave length, λ, obtained from the wave theory and the computations for the Froude numbers, 2.3 and 2.8. For the grids, FINE and FINEST, the computations were performed using Chien's k-ϵ turbulence model and the inviscid and viscous free-surface boundary conditions.

Grid	FINE		FINEST
Fn_T	2.3	2.8	2.8
Analytical, λ [m]	3.324	4.925	4.925
Vanden-Broeck, λ [m]	2.974	4.802	4.802
Euler, inviscid mirror BC, λ [m]	3.333	4.875	4.858
$\Delta\lambda$ [%]	12	1.5	1.2
k-ϵ, inviscid mirror BC, λ [m]	3.250	4.775	4.775
$\Delta\lambda$ [%]	9.3	0.6	0.6
k-ϵ, inviscid irrotational BC, λ [m]	3.080	4.792	
$\Delta\lambda$ [%]	3.6	0.2	
k-ϵ, tang.-str. BC, λ [m]	3.167	4.792	4.792
$\Delta\lambda$ [%]	6.5	0.2	0.2
k-ϵ, Reyn.-str. BC, λ [m]	3.167	4.792	4.792
$\Delta\lambda$ [%]	6.5	0.2	0.2

For the Froude number, $Fn_T = 2.3$, the wave lengths are presented for the grid, FINE. Also here, the Euler solution gives the greatest deviation from the wave length of Vanden-Broeck. The viscous free-surface boundary conditions give again a closer result. The closest result is obatined with the inviscid irrotational free-surface boundary conditions.

Compared with the results for $Fn_T = 2.8$, the greater deviations from the result of Vanden-Broeck are due to the coarse resolution of the transom waves which become shorter with decreased Froude numbers.

Experiment and Potential-Flow Computations

The case examined in this work has already been investigated by Saisto. He carried out measurements, *Saisto (1995)*, and potential-flow computations, *Saisto (2000)*, of the wave profile behind the transom at different Froude numbers. His results show excellent agreement with the ones given by *Vanden-Broeck (1980)*. In his numerical investigation, the appearance of the bow wave was suppressed. The bottom was flat and semi-infinitely long. The following computations are carried out for the Froude number, 2.8, using the inviscid mirror and the inviscid irrotational free-surface boundary conditions.
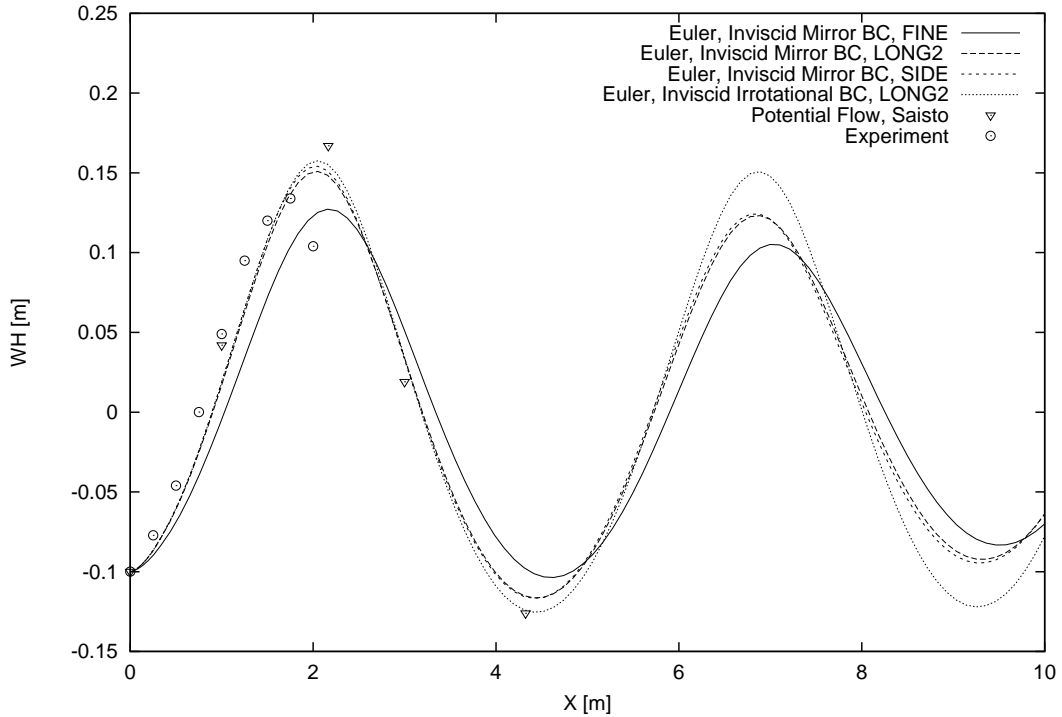
Figure 4.1: Wave profiles behind the transom of the model, *Ile.* Comparison of the computed results with the ones obtained from potential-flow computations, *Saisto (2000)*, and the experiment, *Saisto (1995)*. The computations were carried out solving the Euler equations with the inviscid mirror and the inviscid irrotational free-surface boundary conditions. The used grids were FINE, LONG2 and SIDE. $Fn_T = 2.8$.

For the grid, FINE, the solution of the Euler equations gives a significant deviation of the transom wave from the potential-flow solution and the experimental result (Fig. 4.1). The height and the steepness of the computed wave profile are much smaller. This deviation is mainly caused by the existence of a low-pressure region at the bow shoulder. Saisto's computations were carried out without the presence of the bow shoulder. The bottom was only flat. Therefore, at the shoulder region, the flow situations are different in the compared computations resulting in different wave profiles. In the experiment, the bow wave and the shoulder were present. In this case, they seem to equalize their influences on the transom wave. The steepness of the wave is quite close to the one obtained from Saisto's computations. Nevertheless, the wave height of the experimental result is much lower because of viscosity and three-dimensional effects. In the experiment, the wave

pattern was already three-dimensional at a distance of about 2.7 meters behind the transom. Generally, either the shoulder influence or the bow-wave influence on the transom wave is dominant, which would give a wave profile different from the one derived by Saisto. Only for a very long model, these influences on the transom wave will become negligible. Therefore, using the experimental result for validation purposes might be somehow questionable. Nevertheless, it may be used for a qualitative evaluation at least.

In order to get rid of the shoulder influence, the grid, FINE, is made longer by adding a certain amount of cells to the flat bottom. Their length is constant. In this way, the flat bottom becomes significantly longer, and the rest of the computational domain remains identical with the grid, FINE. Two cases, LONG1 and LONG2, are investigated. LONG1 has a many meters shorter flat bottom than LONG2. The wave profile obtained with the grid, LONG2, shows only a very slight change in comparison with the one obtained with the grid, LONG1. Therefore, the grid, LONG2, is consistent with a semi-infinitely long grid. Using the grid, LONG2, the computation gives a result close to the ones obtained from the potential-flow computation and the experiment (Fig. 4.1). This clarifies also the remarkable influence of the shoulder on the results.

Using the grid, SIDE, the influence of the depth of the computational domain on the results is evaluated. The grid, SIDE, is consistent with the grid LONG2, but it possesses a significantly greater depth. For the grid, SIDE, almost no change of the wave profile is obtained (Fig. 4.1). Therefore, the water depth may be assumed as sufficiently large.

Using the grid, LONG2, and the inviscid irrotational free-surface boundary conditions, an improved solution is obtained. The wave profile is close to the one obtained from the potential-flow computation, particularly farther downstream, and it is almost not dampened, which is physically correct.

In Fig. 4.2, the influence of the resolution at the transom on the wave profile is investigated. The grid, FINETRANSOM, possesses an at least three times higher resolution at the transom than the grid FINE. The computations using the grids, FINE and FINETRANSOM, give no difference. Therefore, the resolution at the transom may be assumed as sufficient.

In Fig. 4.3, the influence of the resolution of the grid on the wave profile is evaluated. At the transom, almost no grid influence is apparent. Farther away, it is significant.

According to Figs. 4.1 up to 4.3, it may be concluded that the wave profile at the transom obtained for the case, LONG2, is the solution of the Euler equations with application of the inviscid irrotational free-surface boundary conditions. Here, the flat bottom is semi-infinitely long. The difference

between the Euler and potential-flow solutions is due to the fact that the Eulerian flow is rotational, and the potential flow is irrotational. A similar result was obtained by *Farmer (1993)*. The application of the inviscid mirror free-surface boundary conditions gives a significantly dampened wave profile. The reason for this will be clarified in the section, 4.3. Comparing the results obtained for the grid, FINE, and from the experiment (Fig. 4.1), it may be concluded that the appearance of the bow wave has a significant influence on the transom wave. The experiment includes shoulder and bow-wave effects. The grid, FINE, includes only shoulder effects. Close to the transom, the area of interest, the grids, FINE and FINEST, are sufficient for the further analysis.
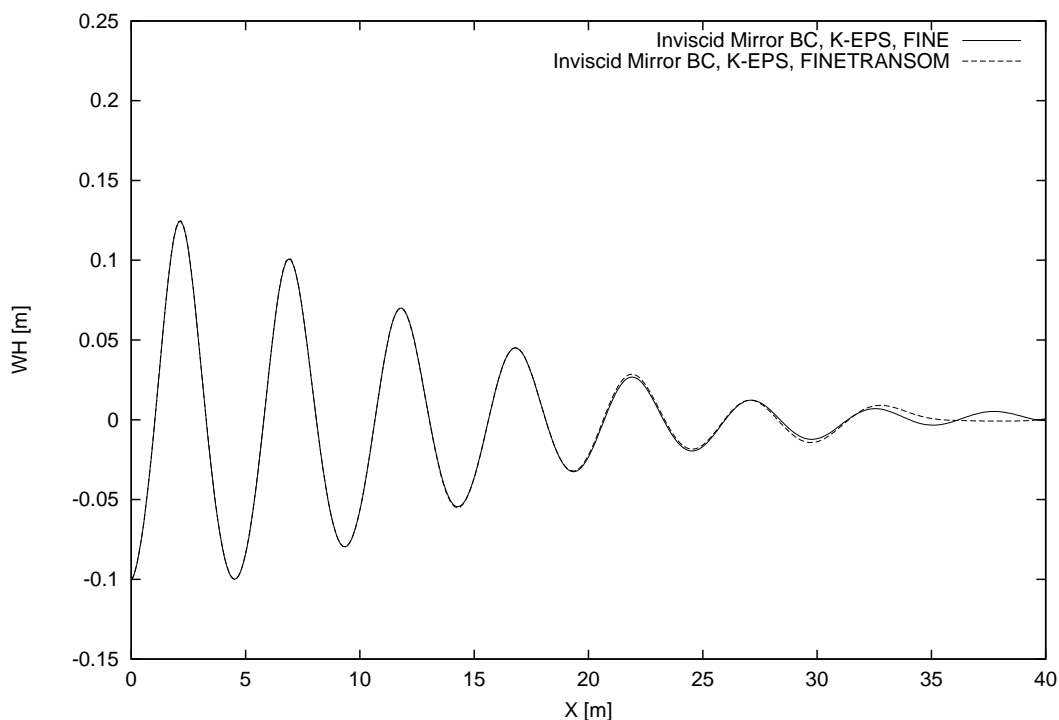
Figure 4.2: Influence of the resolution at the transom on the wave profile of the model, *Ile*. Comparison of the computed results obtained for the grids, FINE and FINETRANSOM. The computations were carried out using Chien's k-ϵ turbulence model and the inviscid mirror free-surface boundary conditions. $Fn_T = 2.8$.
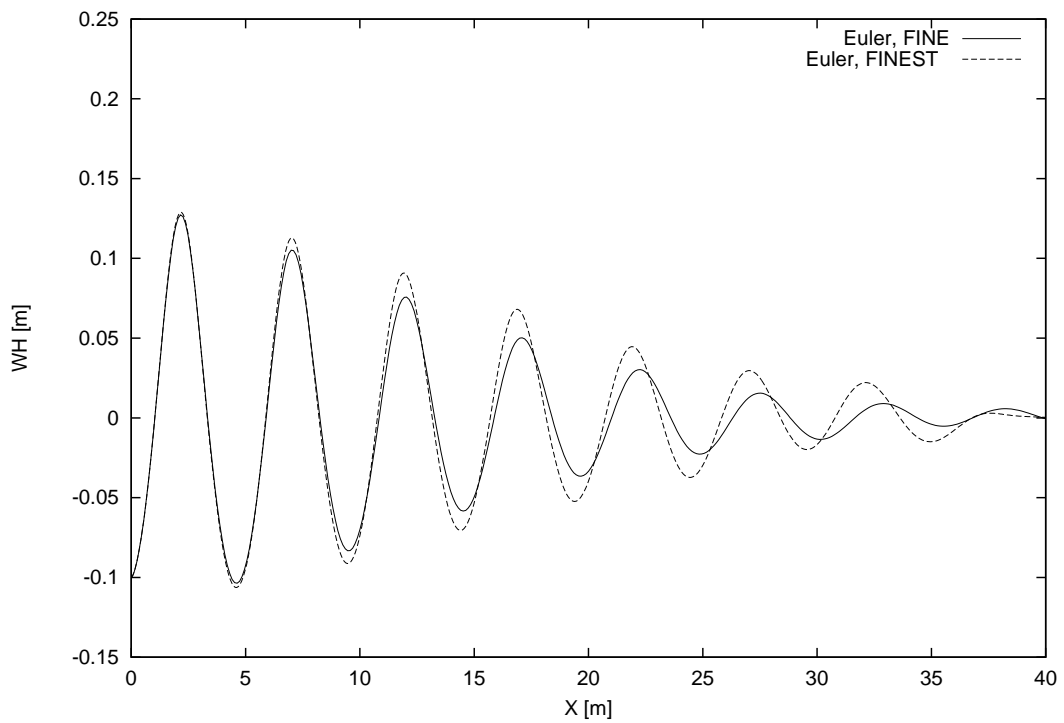
Figure 4.3: Influence of the grid resolution on the wave profile behind the transom of the model, *Ile*. Comparison of the computed results obtained for the grids, FINE and FINEST. The computations were carried out solving the Euler equations with the inviscid mirror free-surface boundary conditions. $Fn_T = 2.8$.

4.1.2 Flat Plate at the Full-Scale Ship Reynolds Number, $Re_l = 9.442 \times 10^8$

In a former investigation, it has been shown that the FINFLO code is able to deal with high-Reynolds-number flows without pressure gradient up to ship scale, *Schweighofer (1997)*. There, the fully turbulent flow over a flat plate for a large range of Reynolds numbers was investigated using the two-dimensional, compressible version of FINFLO, FINF2D, *Hellsten (1996)*, *Hoffrén and Siikonen (1992)*. The three-dimensional, incompressible version of FINFLO used in this work has not been tested for turbulent flows at full-scale ship Reynolds numbers so far. Therefore, using Chien's low Reynolds number k-ϵ turbulence model, the fully turbulent flow over a flat plate is computed at the full-scale ship Reynolds number, $Re_l = 9.442 \times 10^8$. The computations are described in the chapter, three. The validation is carried out with respect to the skin friction, the nondimensional velocity profile and the nondimensional turbulent viscosity.

Influence of the Free-Stream Turbulence Quantities on the Turbulent Boundary Layer

The appearing free-stream turbulence quantities are the turbulent kinetic energy, k_∞, the turbulence level, I_∞, the nondimensional turbulent viscosity, $\mu_{T\infty}/\mu$, and the dissipation of the turbulent kinetic energy, ϵ_∞. Their relation to each other is given in the following.

In the input, the turbulence level, I_∞, and the nondimensional turbulent viscosity, $\mu_{T\infty}/\mu$, are given. Using the free-stream velocity, U_∞, the free-stream turbulent kinetic energy, k_∞, is obtained from

$$k_\infty = \frac{3}{2}(I_\infty U_\infty)^2 \ .$$

The dissipation of the turbulent kinetic energy, ϵ_∞, is obtained by rearranging Eq. (2.12) to

$$\epsilon_\infty = 0.09 \frac{\rho k_\infty{}^2}{\mu_{T\infty}} \ .$$

The turbulence level, I_∞, is set to the same value as at model scale. It accounts for 0.001, which corresponds to the lower limit of a normal wind tunnel, *Schlichting (1979)*.

In the first case, the nondimensional turbulent viscosity, $\mu_{T\infty}/\mu$, is set to 0.01 corresponding to the respective value at model scale. The molecu-

lar viscosity is a property of the fluid remaining unchanged. Therefore, the free-stream turbulent viscosity remains also unchanged. Due to the increased free-stream velocity and the constant turbulence level, the free-stream turbulent kinetic energy is increased at full-scale giving a significantly increased dissipation of the turbulent kinetic energy, ϵ_∞. This causes a strong dissipation of the turbulent kinetic energy in the boundary layer. The development of the turbulent boundary layer is partly prevented. The turbulent kinetic energy and the turbulent viscosity remain too low (Figs. 4.4 and 4.5). In Table 2, the computed mean skin friction coefficient is presented. It is defined as

$$C_F = \frac{\int_A \tau_{wall} dA}{0.5\rho U_\infty^2 A} \;, \tag{4.6}$$

where A is the wetted surface of the flat plate. The deviation from the value of the semi-empirical Engineering Sciences Data (ESD), *Royal Aeronautical Society (1968)*, is with about 1.5 percent quite low. The Engineering Sciences Data are based on experiments conducted at Reynolds numbers up to 5×10^8. Nevertheless, in the case of a proper solution, the result should be close to the one obtained using FINF2D with Chien's low Reynolds number k-ϵ turbulence model, *Schweighofer (1997)*. The result in Table 2 is obtained using the finest grid, FLATFST. The coarser grid, FLATF, gives a result more than 20 percent lower than the one of the ESD.

Table 2: Comparison of the computed mean skin friction coefficients, C_F, with the ones of the semi-empirical Engineering Science Data (ESD) and an estimation based on a former computation *Schweighofer (1997)*. The computations were performed using the grid, FLATFST, and Chien's low Reynolds number k-ϵ turbulence model.

$\mu_{T\infty}/\mu$	0.01	16.5	Schweighofer, 1997	ESD
$C_F \times 10^3$	1.536	1.650	1.660	1.560
Error, ΔC_F [%]	-1.5	5.8	6.4	

In the second case, the nondimensional turbulent viscosity, $\mu_{T\infty}/\mu$, is set to 16.5 giving almost the same free-stream dissipation of the turbulent kinetic energy, ϵ_∞, as at model scale. The dissipation of the turbulent kinetic energy is assumed to be a material property, which remains unchanged. The computation gives a fully developed boundary layer as it should be (Figs. 4.4 and 4.5). The results with respect to the nondimensional turbulent viscosity and the mean skin friction coefficient are in very good agreement with the ones presented in *Schweighofer (1997)*. Almost exactly the same result is obtained by leaving $\mu_{T\infty}/\mu$ equal to 0.01 and setting I_∞ equal to 0.000157

giving the same free-stream dissipation of the turbulent kinetic energy, ϵ_∞, as at model scale.

In the third case, the nondimensional turbulent viscosity, $\mu_{T\infty}/\mu$, is set to 1.0 giving a little increased free-stream dissipation of the turbulent kinetic energy, ϵ_∞, compared with the one at model scale. The results are almost exactly the same as in the second case.

Using $\mu_{T\infty}/\mu$ equal to 16.5 and I_∞ equal to 0.001, the verification and further validation is carried out in the following.
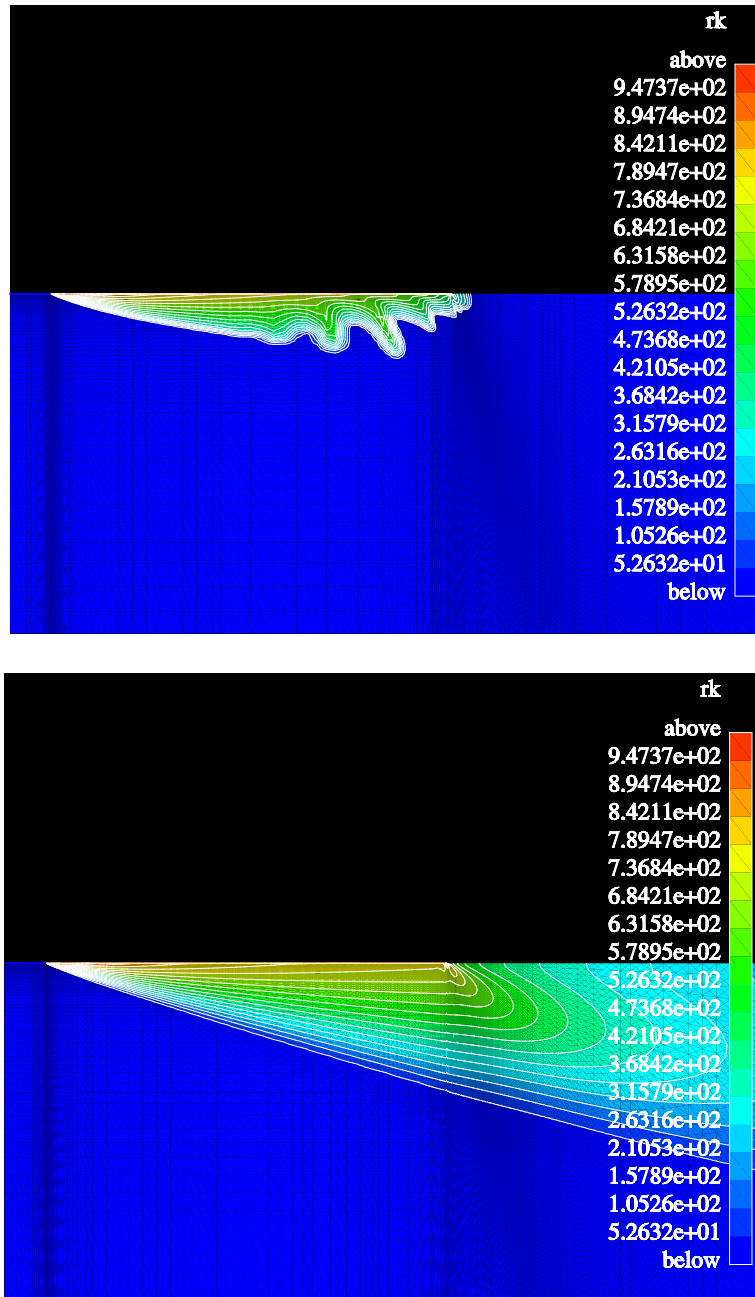
Figure 4.4: Top: Computed kinetic energy of turbulence, ρk, within the boundary layer of the flat plate for $\mu_{T\infty}/\mu = 0.01$. **Bottom:** Computed kinetic energy of turbulence, ρk, within the boundary layer of the flat plate for $\mu_{T\infty}/\mu = 16.5$. The computations were performed using the grid, FLATFST, and Chien's low Reynolds number k-ϵ turbulence model.
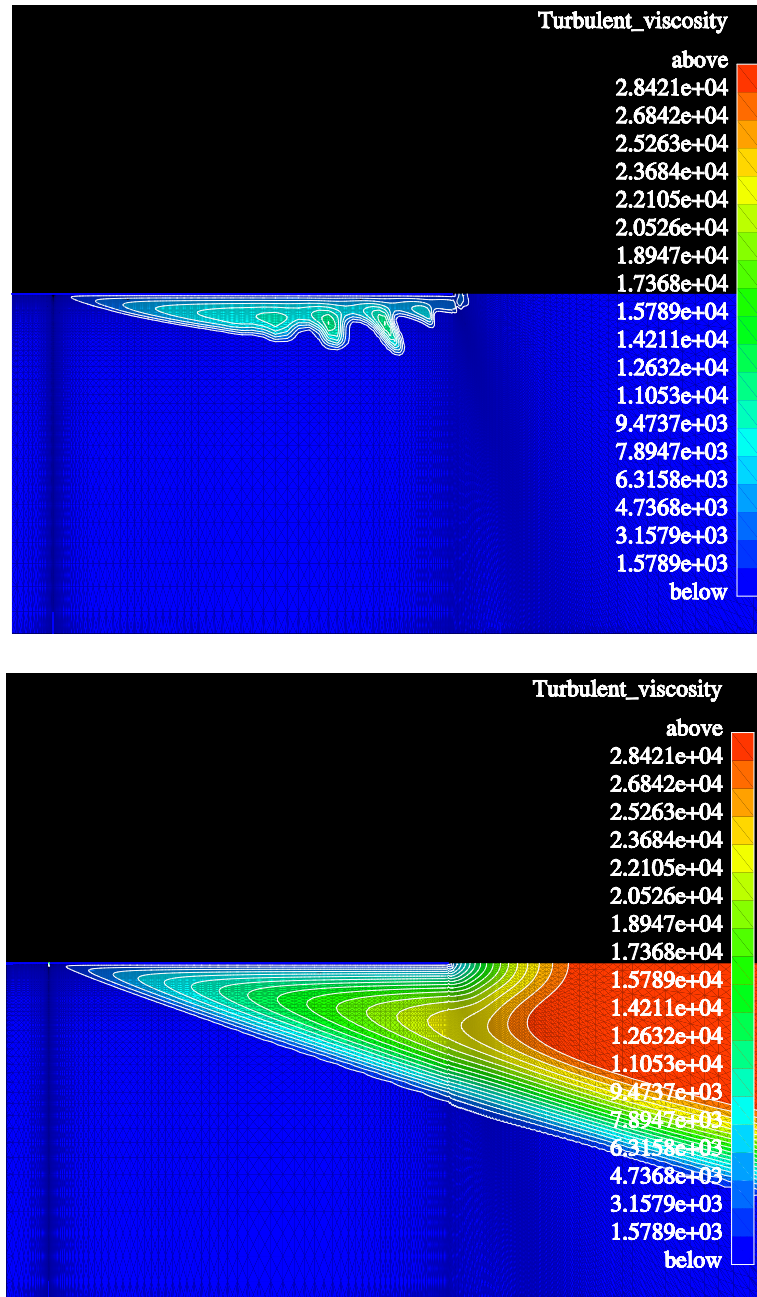
Figure 4.5: Top: Computed turbulent viscosity, μ_T/μ, within the boundary layer of the flat plate for $\mu_{T\infty}/\mu = 0.01$. **Bottom:** Computed turbulent viscosity, μ_T/μ, within the boundary layer of the flat plate for $\mu_{T\infty}/\mu = 16.5$. The computations were performed using the grid, FLATFST, and Chien's low Reynolds number k-ϵ turbulence model.

Skin Friction

The verification meaning the estimation of the discretisation error is carried out using the mean skin friction coefficient. In Table 3, the mean skin friction coefficients obtained with the grids, FLATR, FLATF and FLATFST, are given. They are referred to the value of the Engineering Sciences Data (ESD). The coarsest grid, FLATR, and the finer grid, FLATF, give results with a difference of about 6 percent. The difference between the results derived with the fine grid, FLATF, and the finest one, FLATFST, is less than 0.5 percent. Therefore, the solutions on the grids, FLATF and FLATFST, may be regarded as independent of the grid resolution.

   The result derived with the grid, FLATFST, agrees very well with the one of *Schweighofer (1997)*. With respect to the Engineering Sciences Data (ESD), the result is about six percent too high. Nevertheless, due to a better grid resolution, it is very little improved compared with the one of *Schweighofer (1997)*.

Table 3: Comparison of the computed mean skin friction coefficients, C_F, with the one of *Schweighofer, (1997)*, and the semi-empirical Engineering Science Data (ESD).

	FLATR	FLATF	FLATFST	Schw., 1997	ESD
$C_F \times 10^3$	1.747	1.655	1.650	1.660	1.560
Error, ΔC_F [%]	12.0	6.1	5.8	6.4	

In Fig. 4.6, the local skin friction coefficient obtained from the computation using the grid, FLATFST, and Chien's low Reynolds number k-ϵ turbulence model is given along the flat plate. The computed local skin friction coefficient is defined as

$$C_f = \frac{\tau_{wall}(x)}{0.5\rho U_\infty^2} \ , \qquad (4.7)$$

and $Re_x = U_\infty x/\nu$ is the local Reynolds number, where x is the distance from the leading edge measured in flow direction. With the exeption of the local Reynolds number, in this work, x is always regarded as coordinate of the defined coordinate system (Fig. 3.1). Compared with the semi-empirical Engineering Sciences Data (ESD), the local skin friction coefficient is little overestimated. Compared with the computation of *Schweighofer, (1997)*, the result is improved due to the better resolution of the boundary layer. Nevertheless, over almost the entire length of the plate, the results of both computations deviate from each other by not more than about two percent. The agreement is very good. Close to the local Reynolds number, $Re_x = 10^9$,

the result obtained with the grid, FLATFST, shows a sudden increase of the local skin friction coefficient caused by the application of the mirror boundary condition on the side, five, of the block, BL1 (Figs. 3.1. and 3.5).
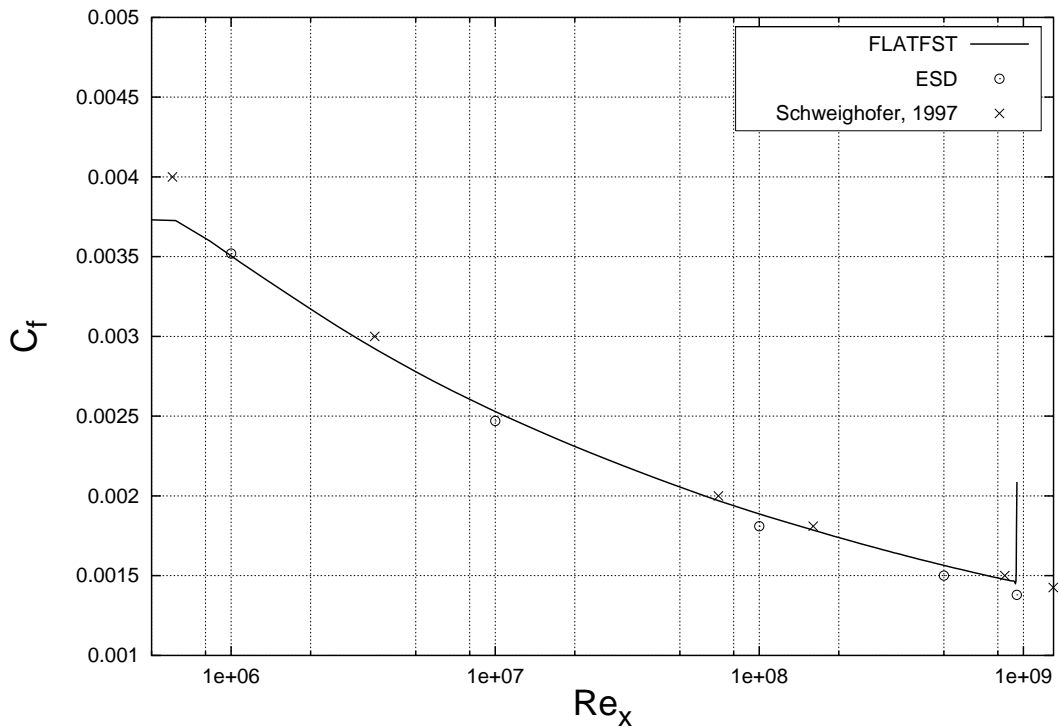

Figure 4.6: Computed local skin friction coefficient (FLATFST), C_f, compared with the semi-empirical Engineering Sciences Data, ESD, and a former computation with the two-dimensional Navier-Stokes solver for compressible flows, FINF2D, *Schweighofer (1997)*. The computations were performed using Chien's low Reynolds number k-ϵ turbulence model.

Nondimensional Velocity Profile

The validation of computations at full-scale ship Reynolds numbers is only to a certain degree possible as sufficient experimental results are very rare. For example, measurements of the mean skin friction coefficient have been carried out only for Reynolds numbers not exceeding the value of 5×10^8.

Regarding the nondimensional velocity profile of a smooth, flat plate in incompressible flow, *Fernholz and Finley (1996)* have shown that the law of the wall and the law of the wake are universal and independent of the Reynolds number for $Re_\Theta \geq 500$, where Re_Θ is the Reynolds number based on the boundary-layer momentum thickness. Therefore, with respect to the nondimensional velocity profile, the validation is expected to be fairly reliable.

The nondimensional velocity, u^+, is obtained from

$$u^+ = \frac{u}{u_\tau} \ , \tag{4.8}$$

and the nondimensional distance from the wall, $|z|^+$, is given by

$$|z|^+ = \frac{u_\tau |z|}{\nu} \ . \tag{4.9}$$

$|z|$ is the dimensional distance from the wall. The absolute value is used as z is negative with respect to the used coordinate system (Fig. 3.1).

In the sublayer extending from the wall to $|z|^+ = 5$, the velocity profile of a flat plate is linear, *White (1991)*, and

$$u^+ = |z|^+ \ . \tag{4.10}$$

The velocity profile is logarithmic for $|z|^+ \geq 30$, *White (1991)*. There, the law of the wall is valid, which is given by

$$u^+ = \frac{1}{\kappa} ln(|z|^+) + C \ , \tag{4.11}$$

where $\kappa = 0.4$ is the Kármán constant and $C = 5.1$ an empirical constant. Using these empirical constants, the law of the wall gives excellent agreement with the measurements of *Winter and Gaudet (1973), Bruns et al. (1992), Fernholz et al. (1995)* and *Petrie et al. (1990)*.

In Fig. 4.7, the computed nondimensional velocity profiles (FLATFST) are compared with the computed results of *Schweighofer (1997)*, the theory (sublayer, law of the wall) and the measurements of *Winter and Gaudet (1973)*. The agreement with the results of *Schweighofer (1997)* is very good. The sublayer is very well reproduced. A moderate deviation from the law of the wall and the measurements of *Winter and Gaudet (1973)* is obtained. All in all, the obtained result is very satisfactory.
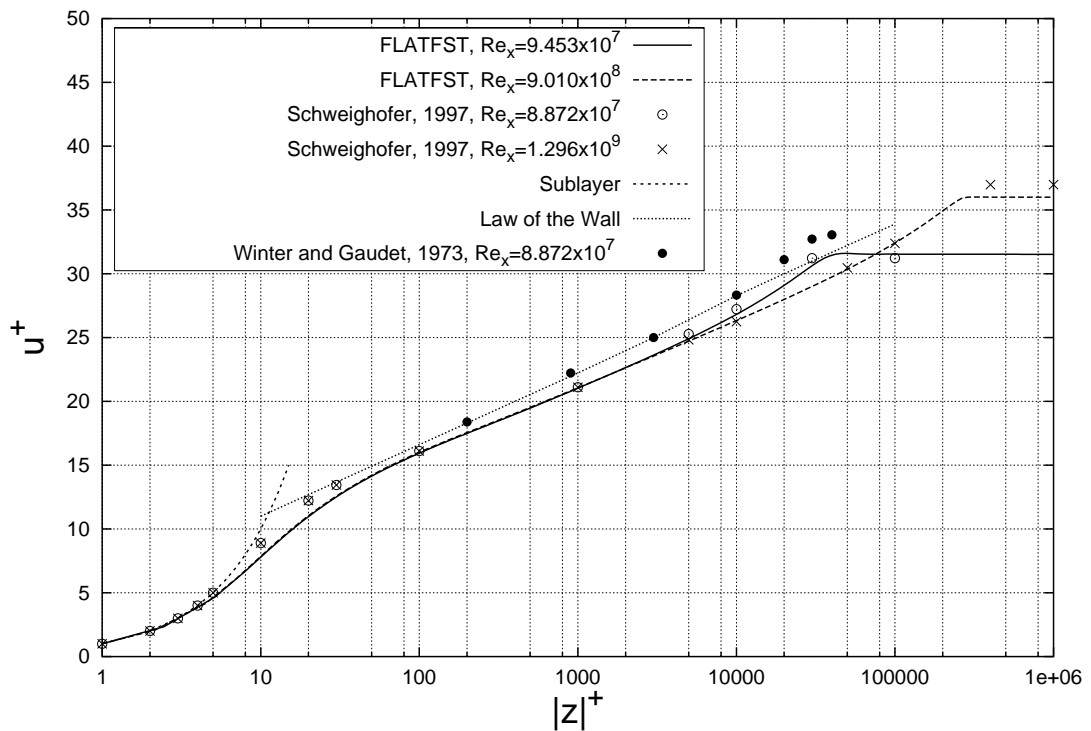
Figure 4.7: Development of the nondimensional velocity, $u^+ = u/u_\tau$, along the nondimensional distance from the wall, $|z|^+ = u_\tau |z|/\nu$, in inner-law scaling. Comparison of the computed results (FLATFST) at the local Reynolds numbers, $Re_x = 9.453 \times 10^7$ and $Re_x = 9.010 \times 10^8$, with the results of a former computation using air as medium at $Re_x = 8.872 \times 10^7$ and $Re_x = 1.296 \times 10^9$, *Schweighofer (1997)*, the theory (sublayer, law of the wall) and the measurements of *Winter and Gaudet (1973)*, at $Re_x = 8.872 \times 10^7$. The computations were performed using Chien's low Reynolds number k-ϵ turbulence model.

Nondimensional Turbulent Viscosity

Regarding the turbulence, a general correlation cannot be found for the fluctuating velocities, *Fernholz and Finley (1996)*. As the turbulent viscosity appears in the Reynolds-stress free-surface boundary conditions (Eqs. 2.41 and 2.42), it should be reproduced with reasonable accuracy.

For the estimation of the correct reproduction of the turbulence, the computed nondimensional turbulent viscosity is used. In Fig. 4.8, it (FLATFST) is compared with the one of the computation of *Schweighofer (1997)*, which has been validated as far as possible giving a good result regarding the reproduction of the turbulence of the flow over a flat plate. The comparison is performed at the local Reynolds numbers, $Re_x = 9.453 \times 10^7$ and 4.226×10^8. In the vicinity of the wall, the results are in very good agreement. In the outer half of the boundary layer, the computation (FLATFST) gives little higher values for the nondimensional turbulent viscosity than the one of *Schweighofer (1997)*. This is due to the different local Reynolds numbers of the comparison and the better resolution of the boundary layer using the grid, FLATFST.

The result of the entire validation with respect to the turbulent flow over a flat plate can be summarized as very good. The agreement of the computed results with the measurements is satisfactory. The computed results (FLATFST) are almost exactly the same as the ones of a former computation of *Schweighofer (1997)*. The incompressible version of FINFLO, used in this work, is able to deal with turbulent flows without a pressure gradient at full-scale ship Reynolds numbers giving fairly accurate results. In the x-direction (Fig. 3.1), the model, *Ile*, of the investigation is flat over a large part. In the z-direction (Fig. 3.1), it may be regarded as very thin. The ratio of the length between the perpendiculars and the draught is about 15, giving a weak pressure gradient. The skin friction and the structure of the turbulence are assumed to be of similar nature as for the plate. Therefore, the incompressible version of FINFLO is suitable for the investigation at full-scale. Nevertheless, a validation of the turbulence below the free-surface is not carried out. As the pressure gradient is weak and no separation with recirculating flow appears, it is assumed that Chien's low Reynolds number k-ϵ turbulence model is sufficient for an approximate treatment of the appearing turbulence within the waves.
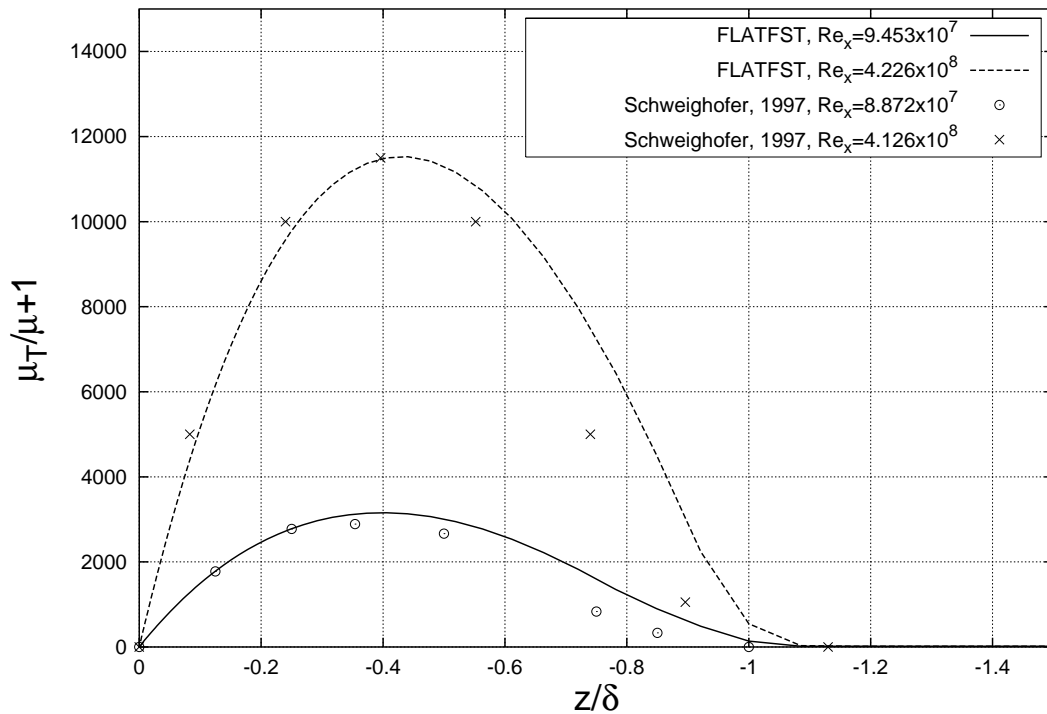
Figure 4.8: Distribution of the nondimensional turbulent viscosity, μ_T/μ, within the boundary layer with the thickness, δ. Comparison of the computed results (FLATFST) at the local Reynolds numbers, $Re_x = 9.453 \times 10^7$ and $Re_x = 4.226 \times 10^8$, with the results of a former computation using air as medium at $Re_x = 8.872 \times 10^7$ and $Re_x = 4.126 \times 10^8$, *Schweighofer (1997)*. The computations were performed using Chien's low Reynolds number k-ϵ turbulence model.

4.2 Multigridding at the Full-Scale Ship Reynolds Number, $Re_l = 9.442 \times 10^8$

The convergence of the computations may be improved by the application of multigridding. The achieved acceleration ranges from 10 to 100 when five grid levels are used, *Ferziger and Perić (1999)*. For diffusion dominated flows where viscostity effects are significant, the biggest savings may be obtained. For convection dominated flows where the Euler equations are solved, the savings are smallest, *Ferziger and Perić (1999)*.

At full-scale ship Reynolds numbers, the influence of viscosity is less pronounced than at model scale, and the flow is closer to the solution of the Euler equations. Therefore, with respect to multigridding, the savings are also smaller. As the application of multigridding may increase the CPU-time for one iteration, the final computational time might be even increased in order to get a converged solution. Regarding multigridding, a huge amount of publications can be found. Nevertheless, in Chapter 1, a summary of existing publications concerning computations at full-scale ship Reynolds numbers is given. These publications give no information about the efficiency of multigridding at full-scale ship Reynolds numbers. In this work, a first estimation of the efficiency and meaningfulness of multigridding at full-scale ship Reynolds numbers is given.

Apart from the general interest in this matter, the investigation is carried out because of practical reasons. Using the current Navier-Stokes solver, FINFLO, the application of multigridding demands a grid consisting of at least two cells in the y-direction. Without multigridding, a grid consisting of only one cell in the y-direction may be used. The application of multigridding will give a lower number of iterations for a converged solution, but the CPU-time for one iteration may be increased due to more operations and the increased number of cells. Further, the free-surface has to be manipulated manually several times increasing the time in order to get a final solution.

The computations are carried out using the grid, FINEFSC, and the Baldwin-Lomax turbulence model under the same conditions as the full-scale computations described in Section 3.3.2. For the application of multigridding, the grid, FINEFSC, consists of two cells in the y-direction. For no application of multigridding, only one cell is needed. In the beginning of the investigation at full scale, Chien's low Reynolds number k-ϵ turbulence model gave false results and instability caused by certain restrictions of the code. Therefore, the investigation of the efficiency of multigridding at full-scale ship Reynolds numbers is carried out using the Baldwin-Lomax turbulence model. The free-surface is kept fixed, and the mirror boundary condition is applied there

(Figs. 3.1 and 3.4). For multigridding, two grid levels with a simple V-cycle are used.

A comprehensive desrciption of the multigrid method used in FINFLO may be found in *Siikonen (1994)*, *Siikonen (1996)* and *Siikonen et al. (1990)*. The multigrid algorithm follows the method of *Jameson and Yoon (1986)*. First, the solution and the respective residual is computed on the finest grid level giving a first approximation for the solution on the next coarser grid level. Then, the solution and respective residual are computed on the coarser grid level at a reduced cost. On the coarser grid level, the number of cells is lower giving a shorter time for one iteration. The applied spatial discretization is of first-order accuracy allowing the use of higher Courant numbers, and the cell dimensions are larger. Therefore, the time step of the computations is increased resulting in an accelerated solution. Once the solution and the respective residual are known on the coarser grid level, they are used as an improved approximation of the solution on the finer grid level, and the respective corrections are carried out when going from the coarser level to the finest one. Apart from the application of the first-order discretization scheme on the coarser level, the computations are performed in exactly the same way on all grid levels. The turbulent viscosity is computed only on the finest grid level, and it is kept unchanged on the coarser grid levels.

In Figs. 4.9 and 4.10, the convergence histories of the drag coefficient and the L_2-norms of the residuals regarding the density and the momentum are presented. In FINFLO, the L_2-norm of a quantity, Φ, is calculated as, *Rahman (1999)*,

$$\|\Phi\|_2 = \sqrt{\frac{\Sigma_{i=1}^{n} \Phi_i^2}{n}} \; , \tag{4.12}$$

where n is the number of control volumes of the computational domain. The drag coefficient is defined as

$$C_D = \frac{R_T}{0.5\rho U_\infty^2 A} \; , \tag{4.13}$$

where R_T is the total resistance, and A is the wetted surface (see Section 3.3.2).

Using multigridding, the computed drag coefficient is 7.701×10^{-3}. No multigridding gives 7.641×10^{-3}. The difference between both solutions is less than one percent. Therefore, the obtained solutions converge to the same value as it is requested. The application of multigridding gives a converged solution after about 13000 iterations whereby one iteration takes 10.53

seconds. The solution is converged after about 136890 seconds. No multi-gridding gives a converged solution after about 30000 iterations, and the CPU-time per iteration is 6.86 seconds giving a converged solution after about 205800 seconds. The application of no multigridding increases the time for a converged solution by the factor 1.5. Therefore, for computations with a frozen free surface, the use of the multigridding method can be recommended. Nevertheless, in this work, the evaluation of the fully developed free-surface demands a certain amount of iterations being roughly independent of the bulk flow. The application of multigridding increases the time for one iteration significantly, and much time has to be used for the manual manipulation of the grid. The gain due to the little faster bulk-flow solution is too small in order to compensate for the increased time required by the evaluation of the free surface. Therefore, in this work, the computations are carried out without the application of multigridding.

Generally, in a three-dimensional case where the amount of cells is the same for the application of multigridding and no multigridding, multigridding will give an at least three times faster convergence. Using more grid levels, the improvement may be even more significant. This holds for viscous flows without the evaluation of the free-surface at full-scale ship Reynolds numbers. In cases where the evaluation of the free-surface is clearly faster than the one of the bulk flow, the application of multigridding will give an improved convergence at full-scale ship Reynolds numbers.
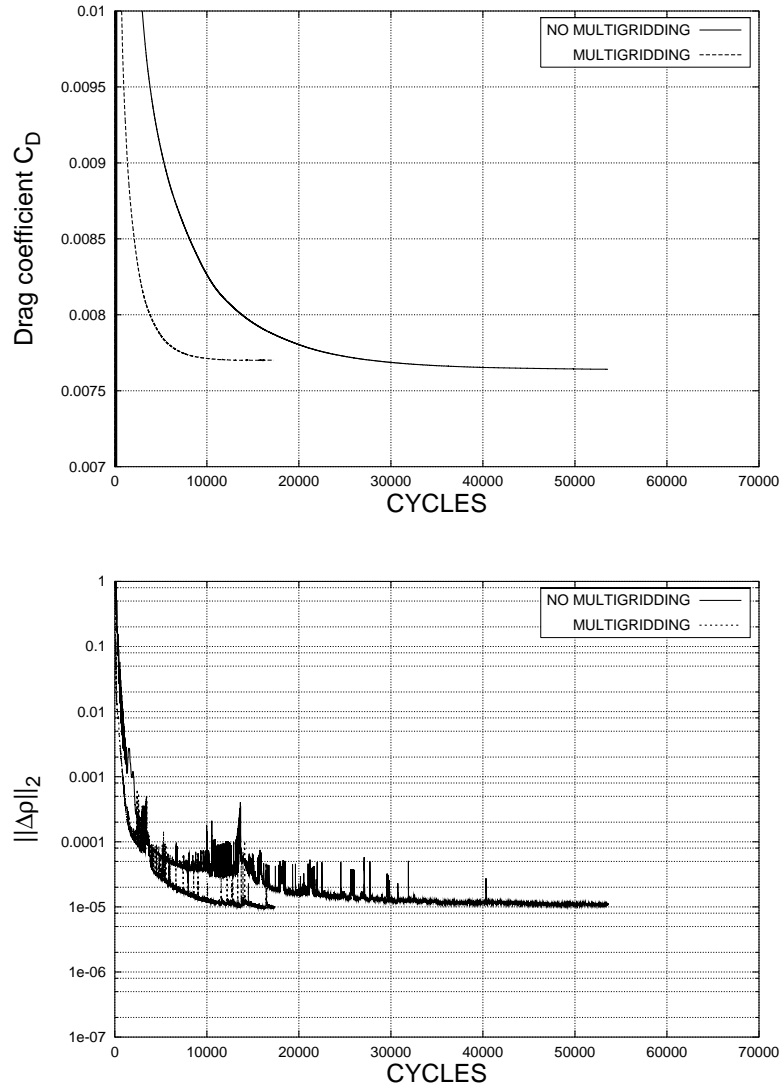
Figure 4.9: The influence of multigridding on the convergence at the full-scale ship Reynolds number, $Re_l = 9.442 \times 10^8$. Convergence histories of the drag coefficient, C_D, and the L_2-norm of the residual of the density, ρ. The computations were performed using the grid, FINEFSC, and the Baldwin-Lomax turbulence model with and without the application of multigridding. The free surface was kept frozen.
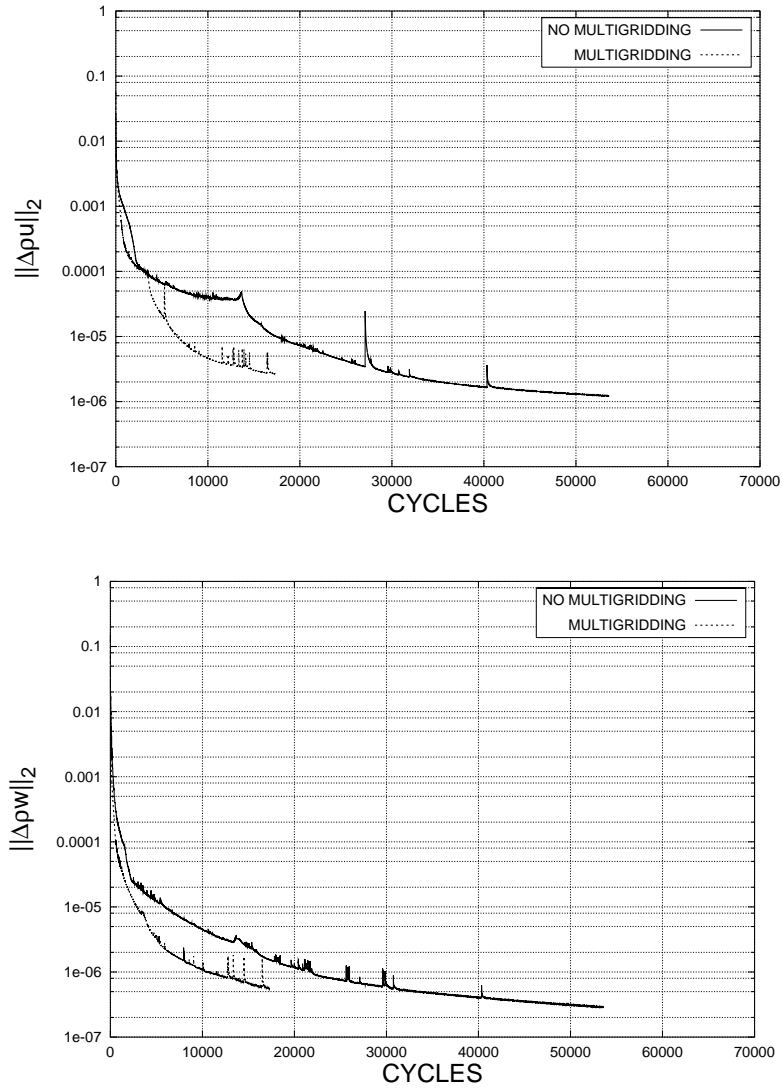
Figure 4.10: The influence of multigridding on the convergence at the full-scale ship Reynolds number, $Re_l = 9.442 \times 10^8$. Convergence histories of the L_2-norms of the residuals of the x-momentum, ρu, and the z-momentum, ρw. The computations were performed using the grid, FINEFSC, and the Baldwin-Lomax turbulence model with and without the application of multigridding. The free surface was kept frozen.

4.3   Froude Number, $Fn_T = 2.8$

In this section, the computed results for the transom wave, the drag coefficient and the convergence are presented for the Froude number, 2.8. The computations were performed solving the Euler and the RaNS equations using Chien's k-ϵ turbulence model and the inviscid mirror and viscous free-surface boundary conditions. Additionally, the wave profiles obtained with the inviscid irrotational, the inviscid flat and the inviscid flat-continuity free-surface boundary conditions are presented. The computations were performed at the Reynolds numbers, $Re_l = 3.732 \times 10^6$ and 9.442×10^8. The used grids were FINE, FINEST, RUOGHFSC and FINEFSC.

4.3.1   Wave Profile, Reynolds Number, $Re_l = 3.732 \times 10^6$

In Fig. 4.11, the computed wave profiles behind the transom of the model, *Ile*, are presented. The used grid was FINEST.

Compared with the viscous free-surface boundary conditions, the application of the inviscid mirror free-surface boundary conditions gives an about 4 percent smaller wave height at the transom and a much stronger damping of the waves farther downstream. Using the inviscid mirror free-surface boundary conditions, the solutions of the Euler and RaNS equations show only little difference. The viscosity of the flow causes only a slight phase shift and almost no damping of the waves behind the transom. The solutions of the RaNS equations using the tangential- and Reynolds-stress free-surface boundary conditions are almost identical. Therfore, the inclusion of the Reynolds stresses into the pressure equation (Eqs. 2.41 and 2.42) has almost no influence on the solution. This is in good agreement with the measurements of *Saisto (1995)*. There, only very small oscillations of the free surface was observed for the Froude number, 2.8., and the draught, 0.1 m. If the Reynolds-stress free-surface boundary conditions gave a significant deviation from the result obtained with the tangential-stress free-surface boundary conditions, this would mean that the Reynolds-stresses in the z-direction are large, and therefore, a remarkable oscillation of the wave profile, as the breaking of waves, should be observed. The application of the Boussinesq approximation seems to work in this particular case.

Influence of the Numerical Scheme Applied to the Calculation of the Velocity Derivatives on the Wave Profile

In Fig. 4.12, the influence of the calculation of the velocity derivatives at the free surface on the wave profile is investigated. The velocity derivatives are

computed according to a two-point upwind scheme of first-order accuracy in the first case and a central difference scheme of second-order accuracy in the second case (see Section 2.4.4). Here, the used schemes for the computation of the velocity derivatives at the free surface give no difference. Therefore, the two-point upwind scheme is accurate enough for the solution of the problem. In all following presented results, it has been applied in association with the additional inviscid and viscous free-surface boundary conditions.
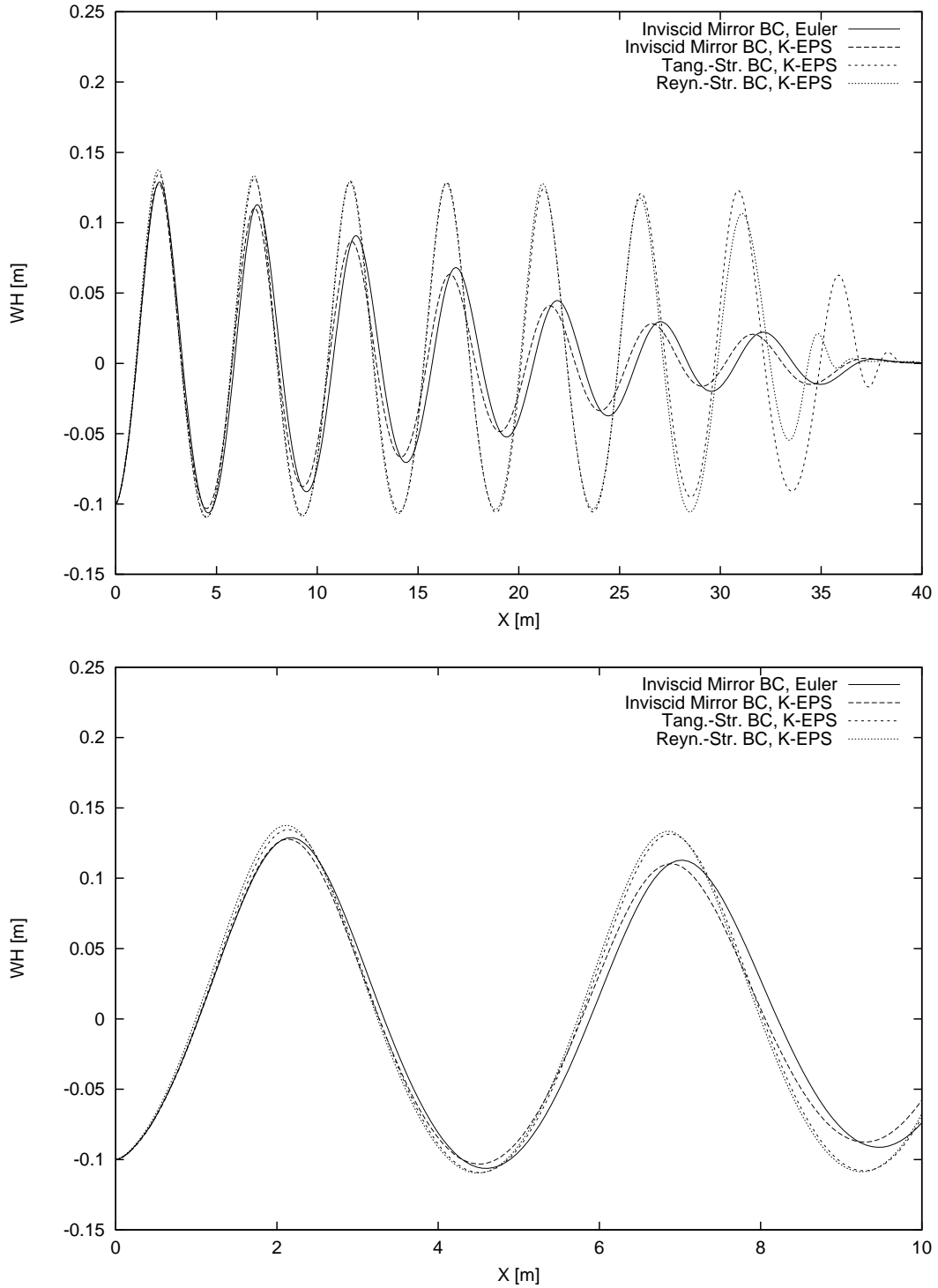
Figure 4.11: Computed wave profiles behind the transom of the model, *Ile*. The computations were carried out solving the Euler and the RaNS equations using Chien's k-ϵ turbulence model and the inviscid mirror and viscous free-surface boundary conditions. The used grid was FINEST. $Fn_T = 2.8$. $Re_l = 3.732 \times 10^6$.
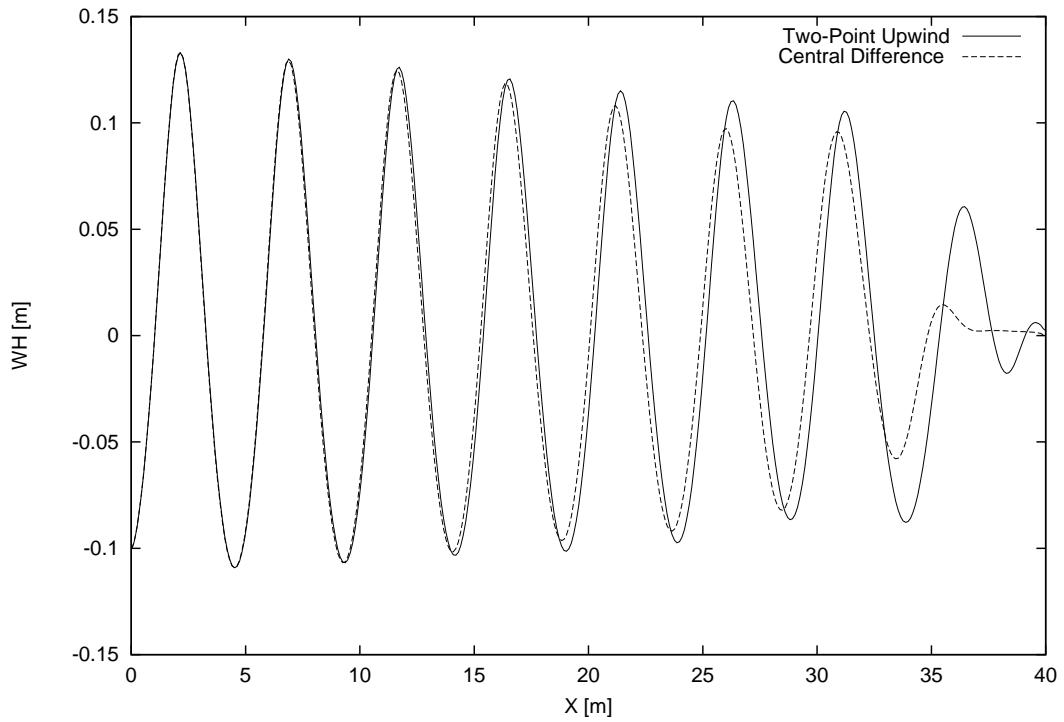
Figure 4.12: Computed wave profiles behind the transom of the model, *Ile*. The computations were carried out solving the RaNS equations using Chien's k-ϵ turbulence model and the tangential-stress free-surface boundary condition. The velocity derivatives at the free surface were calculated according to a two-point upwind and a central-difference scheme. The used grid was FINE. $Fn_T = 2.8$. $Re_l = 3.732 \times 10^6$.

Additional Computations of the Wave Profile

In order to clarify the reason for the deviation of the results associated with the inviscid mirror and viscous free-surface boundary conditions, additional computations are carried out (Fig. 4.13).

In the first case, the Euler equations are solved using the tangential-stress free-surface boundary conditions. In order to obtain a stable solution, the Courant number and DTWMAX are reduced to 3.0 and 0.0003, respectively. Applying the tangential-stress free-surface boundary conditions, the solution of the Euler and RaNS equations gives only a small difference. It can be conducted that the damping of the waves due to the viscosity of the flow is very small. This is consistent with the results obtained for the inviscid mirror free-surface boundary conditions. Therefore, the damping of the waves is caused mainly by the inviscid mirror free-surface boundary conditions.

This is confirmed by the second investigated case (Tang.-Str., Zero Grad. BC) where the tangential-stress free-surface boundary conditions are applied (Eqs. 2.54 and 2.55). Here, additionally, the velocity components are mirrored from the computational domain to the ghost cells according to Eqs. (2.51 and 2.52). Close to the transom, the computed wave profile is almost identical with the one obtained using the inviscid mirror free-surface boundary conditions. Also the damping behaviour is quite similar. Therefore, the calculation of the free-surface velocity components according to the expressions for the tangential free-surface boundary conditions has no influence on the damping behaviour of the waves. The damping is caused by the different velocities in the ghost cells with respect to the different free-surface boundary conditions.

In the third case, the continuity equation was applied for the extrapolation of the velocity component in the z-direction to the free-surface and the ghost cells (Eqs. 2.55, 2.58 and 2.59). The velocity component in the x-direction was extrapolated according to a zero-gradient condition to the free-surface and the ghost cells (Eqs. 2.48, 2.51 and 2.52). The computation gives an unphysical behaviour of the transom wave. Beginning from the transom, it becomes increasingly higher, which might be a result of contradictionary boundary conditions.

Influence of the Alternative Inviscid Free-Surface Boundary Conditions on the Wave Profile

A physically correct solution for the transom wave in viscous flow is characterized by a constant wave steepness and almost no damping of the wave profile. The wave height and the wave length will remain almost constant
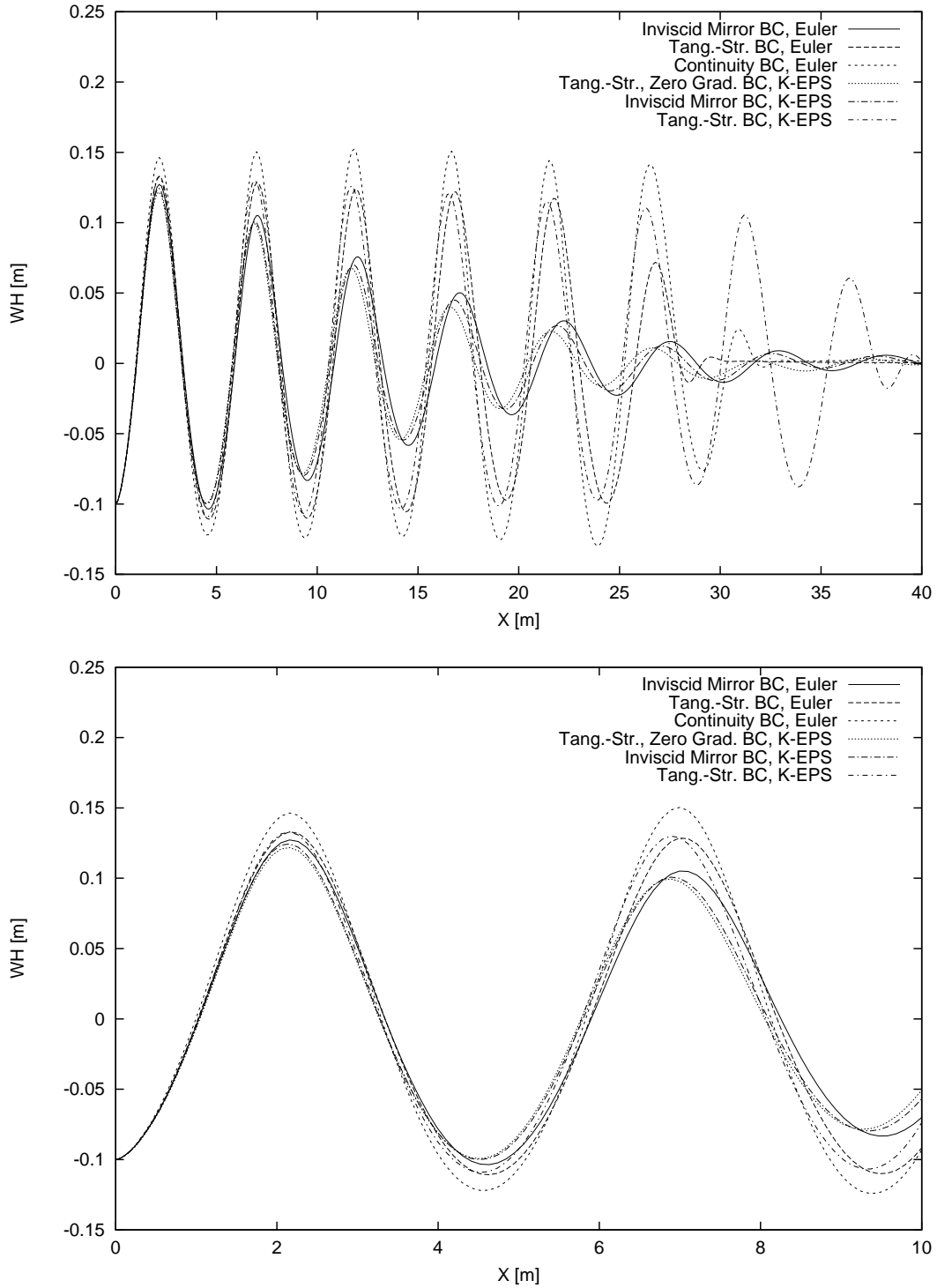
Figure 4.13: Computed transom-wave profiles of the model, *Ile*. The Euler and the RaNS equations were solved using Chien's k-ϵ turbulence model and the inviscid mirror and viscous free-surface boundary conditions. The continuity equation and the tangential-stress boundary condition with a zero-gradient condition for the free-surface velocities were used as additional free-surface boundary conditions. Grid, FINE. $Fn_T = 2.8$. $Re_l = 3.732 \times 10^6$.

away from the intermediate neighborhood of the transom. Qualitatively, this is shown in *Gentaz et al. (2000)* where a proceeding wave is not dampened in a two-dimensional wave tank until it is enforced. The potential-flow solutions indicate the same behaviour. Also, the computations show that the influence of the viscosity on damping is very little. Therefore, the flow away from the transom should show an inviscid behaviour, which means no damping is expected to occur.

The viscous free-surface boundary conditions give a physically correct solution for the wave profile. The currently applied inviscid mirror free-surface boundary conditions give a solution which is physically not correct. The differences between both solutions are only due to the free-surface boundary conditions. Using the inviscid mirror free-surface boundary conditions, there is a contradiction between the obtained dampened result for the wave profile and the ones given in Refs., *Kuk-Jin (1996)* and *Vogt (1998)*. In the mentioned references, the computed wave profile was not dampened although inviscid free-surface boundary conditions were used. The reason for this contradiction may be traced to the different ways of the realization of the inviscid free-surface boundary conditions in the respective code.

In order to get a physically correct solution for the computed wave profile, three alternative inviscid free-surface boundary conditions are implemented into FINFLO and investigated. A detailed describtion of the alternative inviscid free-surface boundary conditions is given in Section 2.4.

In Fig. 4.14, the computed wave profiles behind the transom of the model, *Ile*, are presented. The RaNS equations are solved using Chien's k-ϵ turbulence model and the inviscid mirror and viscous free-surface boundary conditions. Additionally, the inviscid irrotational, the inviscid flat and the inviscid flat-continuity free-surface boundary conditions are used (see Section 2.4). The used grid is FINE.

The viscous, the inviscid irrotational and the inviscid flat-continuity free-surface boundary conditions give almost no difference with respect to the wave profile. The solutions are physically correct. Therefore, the solutions obtained for these inviscid boundary conditions are assumed to be correct.

The inviscid flat free-surface boundary conditions give an even more pronounced damping for the wave profile than the inviscid mirror ones, which is physically not correct.
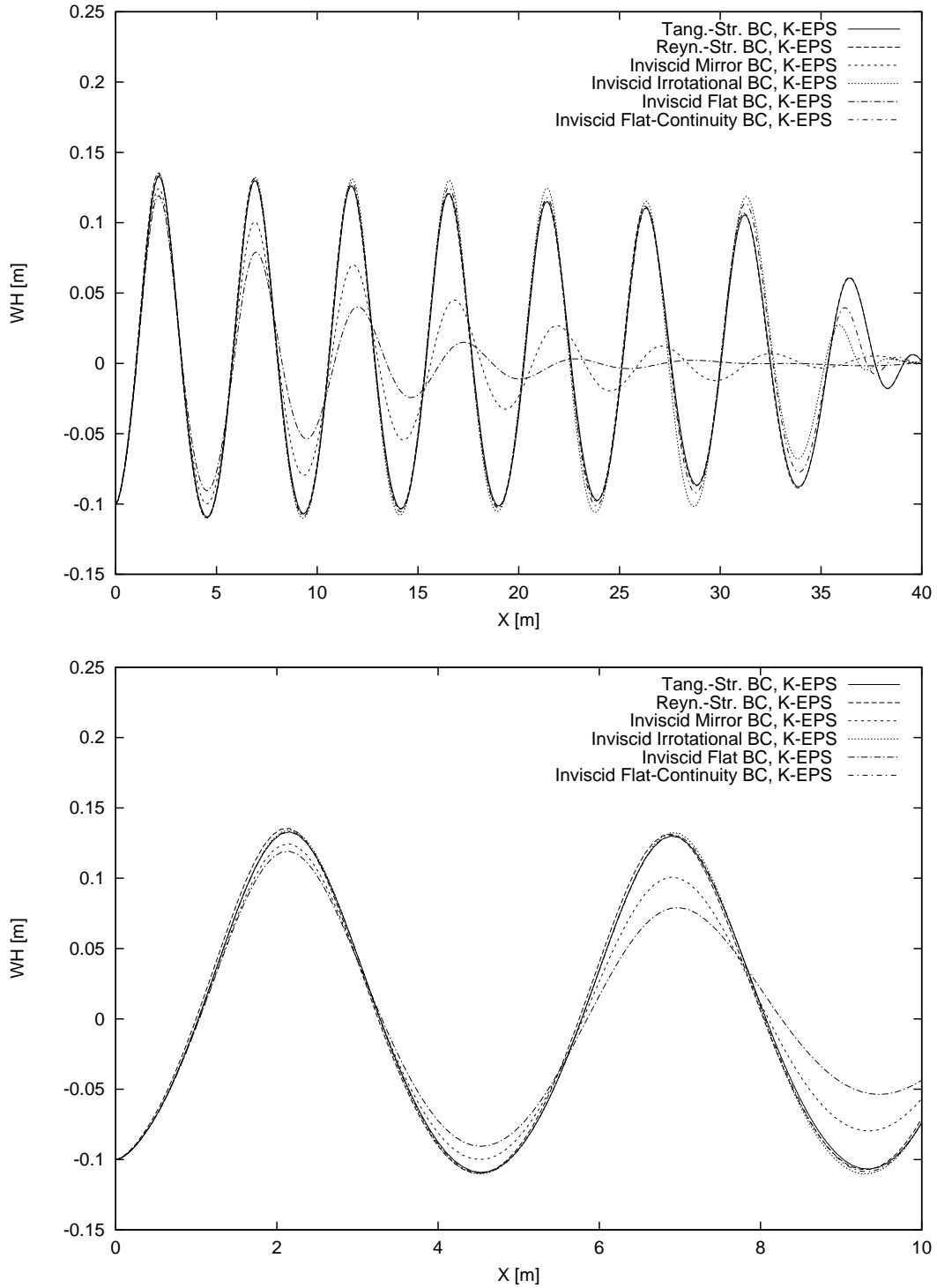
Figure 4.14: Computed wave profiles behind the transom of the model, *Ile*. The RaNS equations were solved using Chien's k-ϵ turbulence model and the inviscid mirror and viscous free-surface boundary conditions. Additionally, the inviscid irrotational, the inviscid flat and the inviscid flat-continuity free-surface boundary conditions were used. The used grid was FINE. $Fn_T = 2.8$. $Re_l = 3.732 \times 10^6$.

The only difference between the tangential-stress and inviscid irrotational free-surface boundary conditions is given by the way how the derivative, $\partial u/\partial z$, is calculated. Using the tangential-stress free-surface boundary conditions, $\partial u/\partial z = -\partial w/\partial x$. Using the inviscid irrotational free-surface boundary conditions, $\partial u/\partial z = \partial w/\partial x$. For both free-surface boundary conditions, the results are almost identical. This can be the case only when $\partial u/\partial z dz = -\partial w/\partial x dz \approx \partial w/\partial x dz$ are very small with respect to the velocity, u, close to the free surface. dz is the distance between the centre points of the cells immediately below and above the free surface, respectively.

The inviscid flat and the inviscid flat-continuity free-surface boundary conditions are different only with respect to the calculation of the derivative, $\partial w/\partial z$. In the first case, $\partial w/\partial z$ is set equal to zero. In the second case, it is calculated from the continuity equation giving $\partial w/\partial z = -\partial u/\partial x$. The difference between the obtained solutions is caused by the calculation of the derivative, $\partial w/\partial z$. Due to the strongly dampened solution obtained with the inviscid flat free-surface boundary conditions, the assumption of $\partial w/\partial z = 0$ seems to be incorrect. The inviscid flat-continuity free-surface boundary conditions give a physically correct solution. Therefore, it may be assumed that $\partial w/\partial z = -\partial u/\partial x \neq 0$. Similarly to the inviscid flat free-surface boundary conditions, the inviscid mirror free-surface boundary conditions give also $\partial w/\partial z = 0$. Therefore, the solution is dampened. Nevertheless, the dampening is not as strong as for the inviscid flat free-surface boundary conditions anymore. This is caused by the different values of the velocity components in the second ghost-cell row above the free surface, which modify the flow field close to the free surface.

Influence of the Grid Resolution on the Wave Profile

In Fig. 4.15, the influence of the grid resolution on the wave profile is evaluated. The solution for the viscous free-surface boundary conditions is widely grid independent. The numerical dissipation caused by the discretization error is very little. The inviscid mirror free-surface boundary conditions give a solution which is still clearly dependent on the resolution of the grid. The amount of numerical dissipation is also higher than in the viscous case. Therefore, a grid-independent solution can be obtained with less computational cells per wave length using the viscous free-surface boundary conditions instead of the inviscid mirror ones. This may result in less computational effort and CPU-time. Nevertheless, close to the transom, the solution obtained with the inviscid mirror free-surface boundary conditions is independent of the grid resolution. Therefore, the dampened solution, there, is due to the

influence of the inviscid mirror free-surface boundary conditions on the flow field.
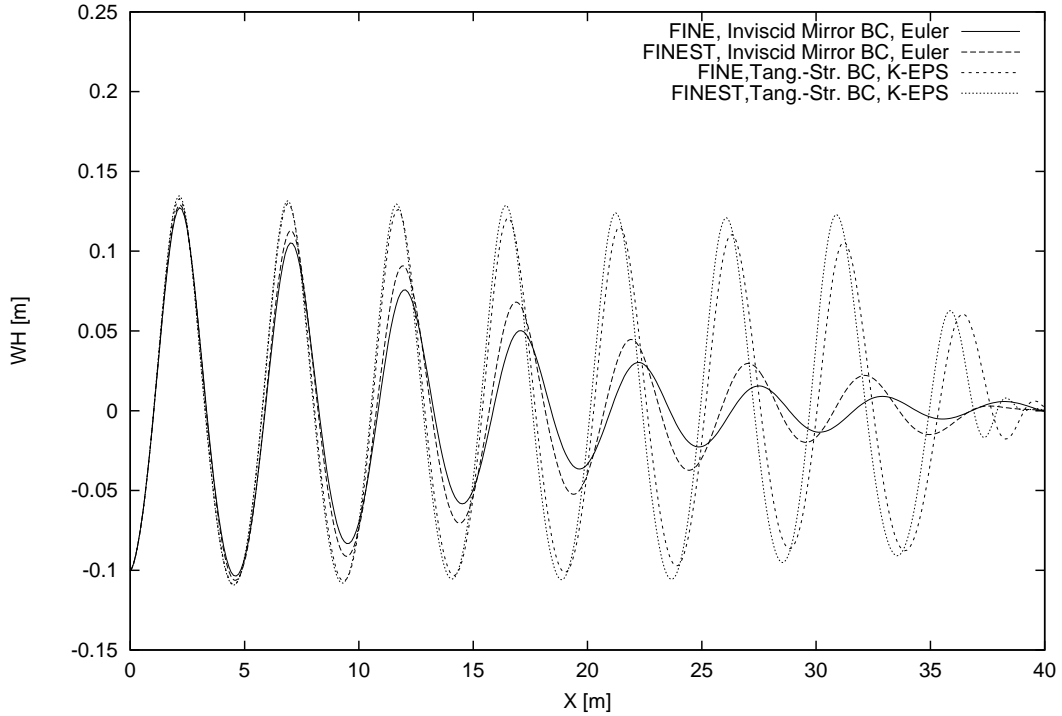

Figure 4.15: Computed wave profiles behind the transom of the model, *Ile*. The computations were carried out solving the Euler and the RaNS equations using Chien's k-ϵ turbulence model and the inviscid mirror and tangential-stress free-surface boundary conditions. The used grids were FINE and FINEST. $Fn_T = 2.8$. $Re_l = 3.732 \times 10^6$.

For the investigated case, it may be concluded that the computed wave profile is not affected by the physics associated with the viscous free-surface boundary conditions. The respective inviscid and viscous free-surface boundary conditions give almost the same result for the wave profile. Nevertheless, it makes a significant difference in which way the inviscid free-surface boundary conditions are realized. Regarding the calculation of the derivative, $\partial w / \partial z$, the assumption, $\partial w / \partial z = 0$, should be avoided, and the application of the continuity equation is recommended. The strongly dampened solution obtained with the inviscid mirror free-surface boundary conditions and the inviscid flat free-surface boundary conditions is caused by the modification of the flow field close to the free-surface and the strong numerical dissipation due to the discretization error.

The expressions associated with the viscous free-surface boundary conditions are not much more complicated than the ones associated with the respective inviscid free-surface boundary conditions giving a physically correct solution. By nature, it is physically more correct to use the viscous free-surface boundary conditions instead of the inviscid ones, and in certain cases, the accuracy of the solution might be improved. Therefore, with respect to the computation of the wave profile, the implementation of the viscous free-surface boundary conditions is justified. Nevertheless, the application of the viscous free-surface boundary conditions causes almost no or very little damping of the waves, which is not always a desired result. In order to avoid the reflection of the waves from the boundaries, it might be necessary to introduce artifical damping zones provided the numerical dissipation due to the grid resolution is not sufficient enough.

4.3.2   Wave Profile, Reynolds Number, $Re_l = 9.442 \times 10^8$

In Fig. 4.16, the computed wave profiles behind the transom of the model, *Ile*, are presented. The used grid was FINEFSC. The computations were performed using Chien's k-ϵ turbulence model and the inviscid irrotational, the Reynolds-stress and the inviscid mirror free-surface boundary conditions at the full-scale ship Reynolds number, $Re_l = 9.442 \times 10^8$.

The results are very similar to the ones at model scale. The inviscid irrotational and the Reynolds-stress free-surface boundary conditions give almost identical results. Therefore, the flow is almost irrotational close to the free surface, and the significantly increased turbulent viscosity has no influence on the wave profile through the free-surface boundary conditions. The inviscid mirror free-surface boundary conditions give again a strongly dampened solution.

Influence of the Grid Resolution on the Wave Profile

In Fig. 4.17, the influence of the grid resolution on the wave profile is estimated. The computations were carried out using the coarse grid, ROUGHFSC, and the fine grid, FINEFSC.

Using the grid, FINEFSC, the inviscid irrotational and the Reynolds-stress free-surface boundary conditions give a solution being approximately independent of the grid resolution. Close to the transom, the results obtained with the grids, ROUGHFSC and FINEFSC, differ only by less than three percent. Therefore, a further refinement of the grid, FINEFSC, will improve the result only very little. Using the grid, FINEFSC, the inviscid mirror

free-surface boundary conditions give a result being still dependent on the grid resolution. Close to the transom the results obtained with the two grids differ only by less than three percent. Therefore, there, the grid resolution of the grid, FINEFSC, may be assumed as sufficient.

Influence of the Reynolds Number on the Wave Profile

In Fig. 4.18, the wave profiles obtained at the Reynolds numbers, $Re_l = 3.732 \times 10^6$ (MSC) and 9.442×10^8 (FSC), are presented. The wave height, WH, and the distance from the transom in the positive x-direction, X, are made nondimensional by referring the respective dimensional value to $L/2$ where L is the length overall. $L/2$ is 1 m and 40 m at $Re_l = 3.732 \times 10^6$ and 9.442×10^8, respectively.

For the full-scale ship Reynolds number, $Re_l = 9.442 \times 10^8$, the solutions are slightly dampened for all presented free-surface boundary conditions compared with the results regarding $Re_l = 3.732 \times 10^6$. Close to the transom, the difference accounts for about five percent. Therefore, the dampened solution is not due to the free-surface boundary conditions. It is either a result of the different flow situation because of the increased Reynolds number or it is due to the different grids, FINE and FINEFSC. In Figs. 4.11, 4.13 and 4.29, it is shown that the viscosity of the flow has only very little influence on the wave profile close to the transom. The solutions of the RaNS and Euler equations are very close. At full scale, the influence of viscosity is less pronounced than at model scale, and the solution of the RaNS equations is expected to be closer to the one of the Euler equations. Therefore, the computed wave profiles should be very similar to the ones of the model-scale computations at $Fn_T = 2.8$. The difference between the solutions at model and full scale is caused by the different used grids. The grid resolution will cause only a difference of one or two percent with respect to the computed wave height close to the transom. This is not sufficient in order to provide an entire explanation for the obtained difference. The block, BL1, of the grid, FINEFSC, is to a higher degree nonorthogonal than the one of the grid, FINE. In BL1 of FINEFSC, the maximum deviation from the orthogonality is about twenty degrees. In FINE, it is only about ten degrees. The deviation of the nonorthoganility causes a numerical error and, therefore, a different solution. *Saisto and Sundell (1996)*, computed the turbulent flow over the HSVA-1 tanker using two grids of different orthogonality. With Chien's k-ϵ turbulence model, regarding the resistance coefficient, the results were by about 4 percent different from each other showing the significance of the grid orthogonality on the results.

In Fig. 4.19, the computed transom waves obtained with the grid, FINE, at model scale, the grid, FINEFSC, and the improved grid, FINEFSC, at full scale are compared with each other. The grid, FINEFSC, was improved with respect to the orthogonality of BL1. The maximum deviation from the orthogonality accounts only for about ten percent similarly to the grid, FINE. The computations were performed using Chien's k-ϵ turbulence model and the inviscid irrotational free-surface boundary conditions. Close to the transom, the wave height is increased by about two percent using the improved version of the grid, FINEFSC. Taking into account the influence of the grid resolution on the computed wave profiles, close to the transom, the difference between the results at model and full scale is between one or two percent. Farther away from the transom, an estimation of the deviation is more difficult as the grids differ much from each other there. Summarized it may be concluded that the wave profiles are almost the same at model and full scale. In this case, the Reynolds number has a negligible effect on the transom wave close to the stern.
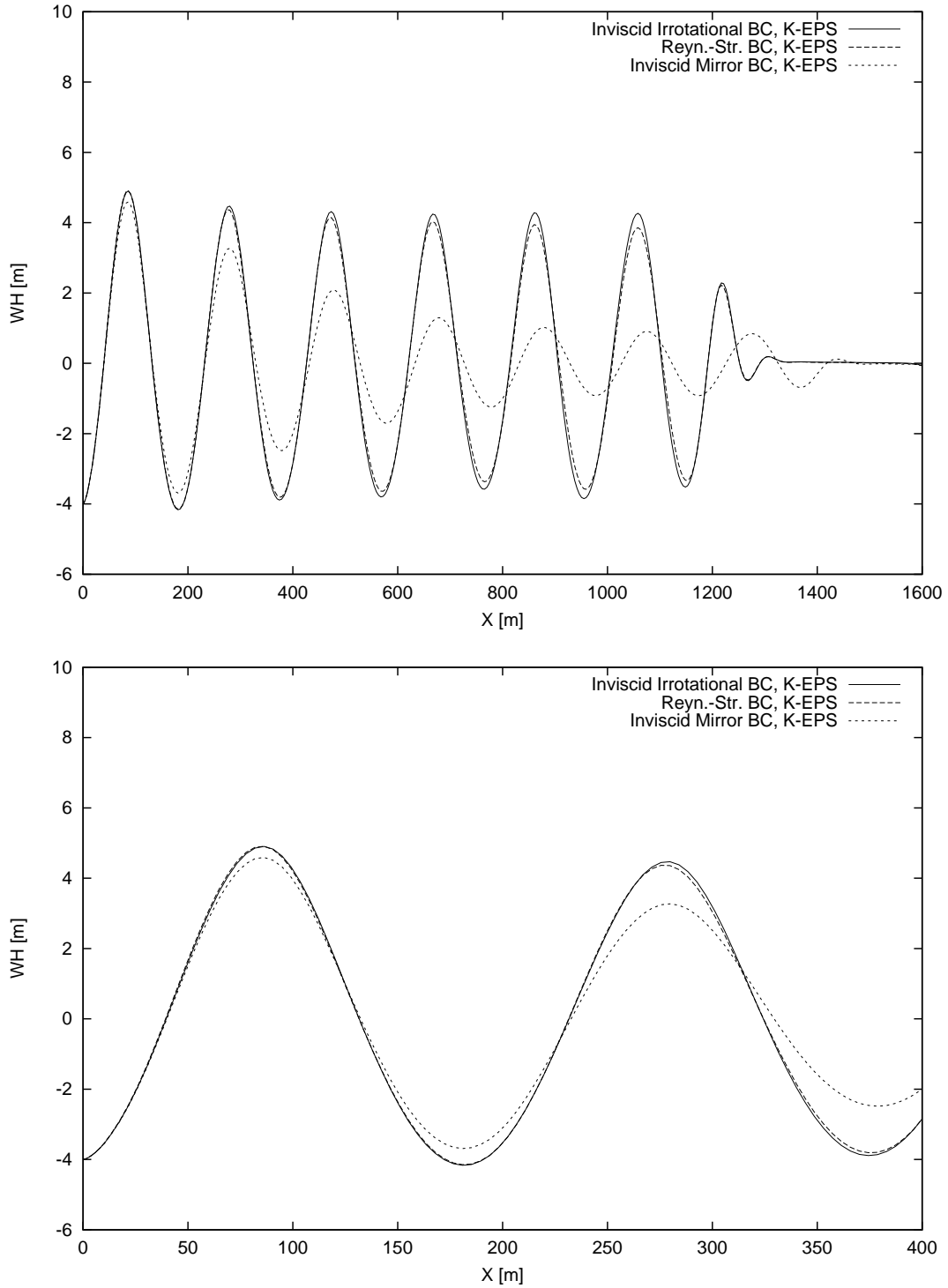
Figure 4.16: Computed wave profiles behind the transom of the model, *Ile*. The computations were carried out solving the RaNS equations using Chien's k-ϵ turbulence model and the inviscid irrotational, the Reynolds-stress and the inviscid mirror free-surface boundary conditions. The used grid was FINEFSC. $Fn_T = 2.8$. $Re_l = 9.442 \times 10^8$.
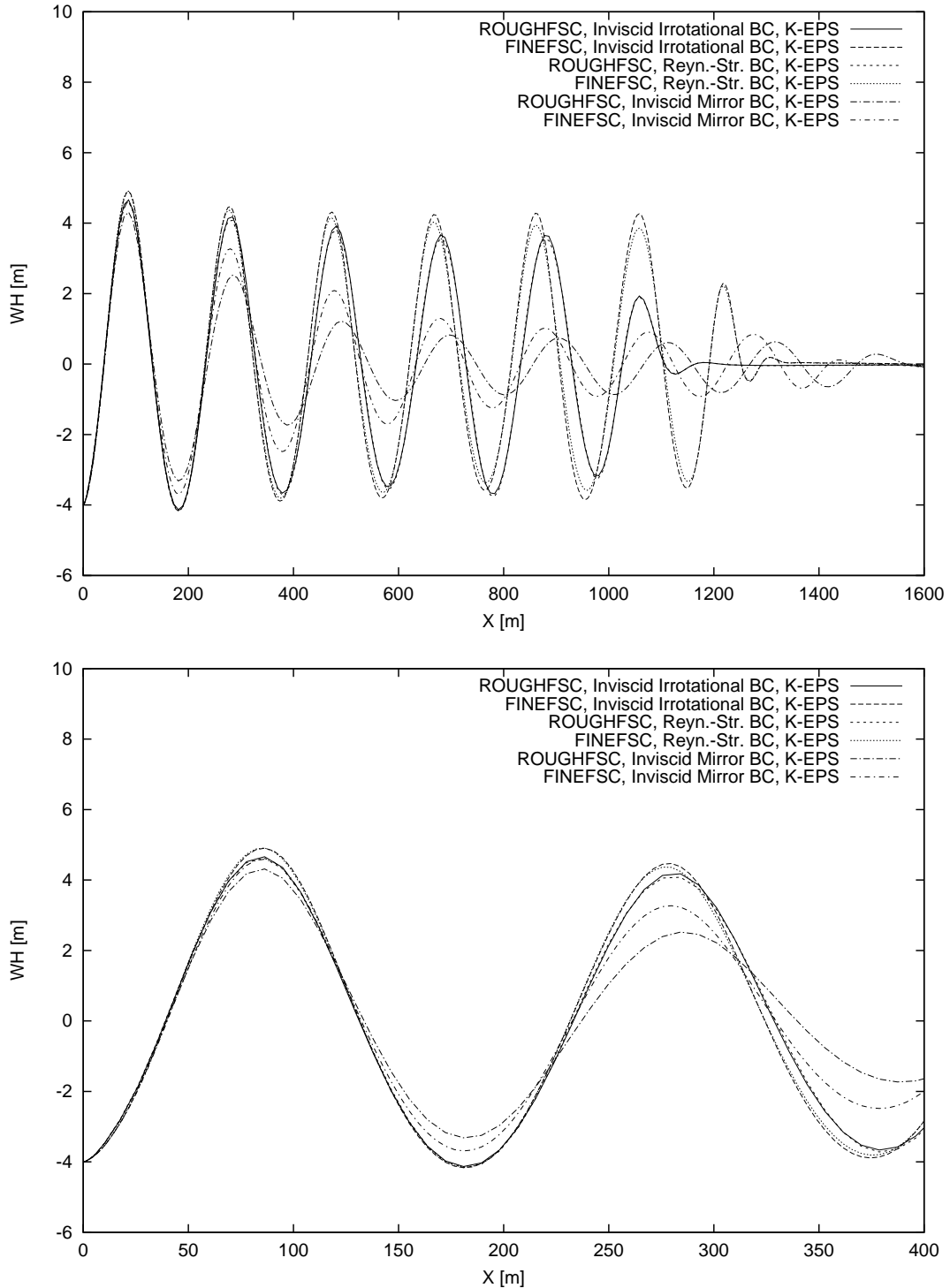
Figure 4.17: Computed wave profiles behind the transom of the model, *Ile*. The RaNS equations were solved using Chien's k-ϵ turbulence model and the inviscid irrotational, the Reynolds-stress and the inviscid mirror free-surface boundary conditions. The used coarse grid was ROUGHFSC, and the finer one was FINEFSC. $Fn_T = 2.8$. $Re_l = 9.442 \times 10^8$.
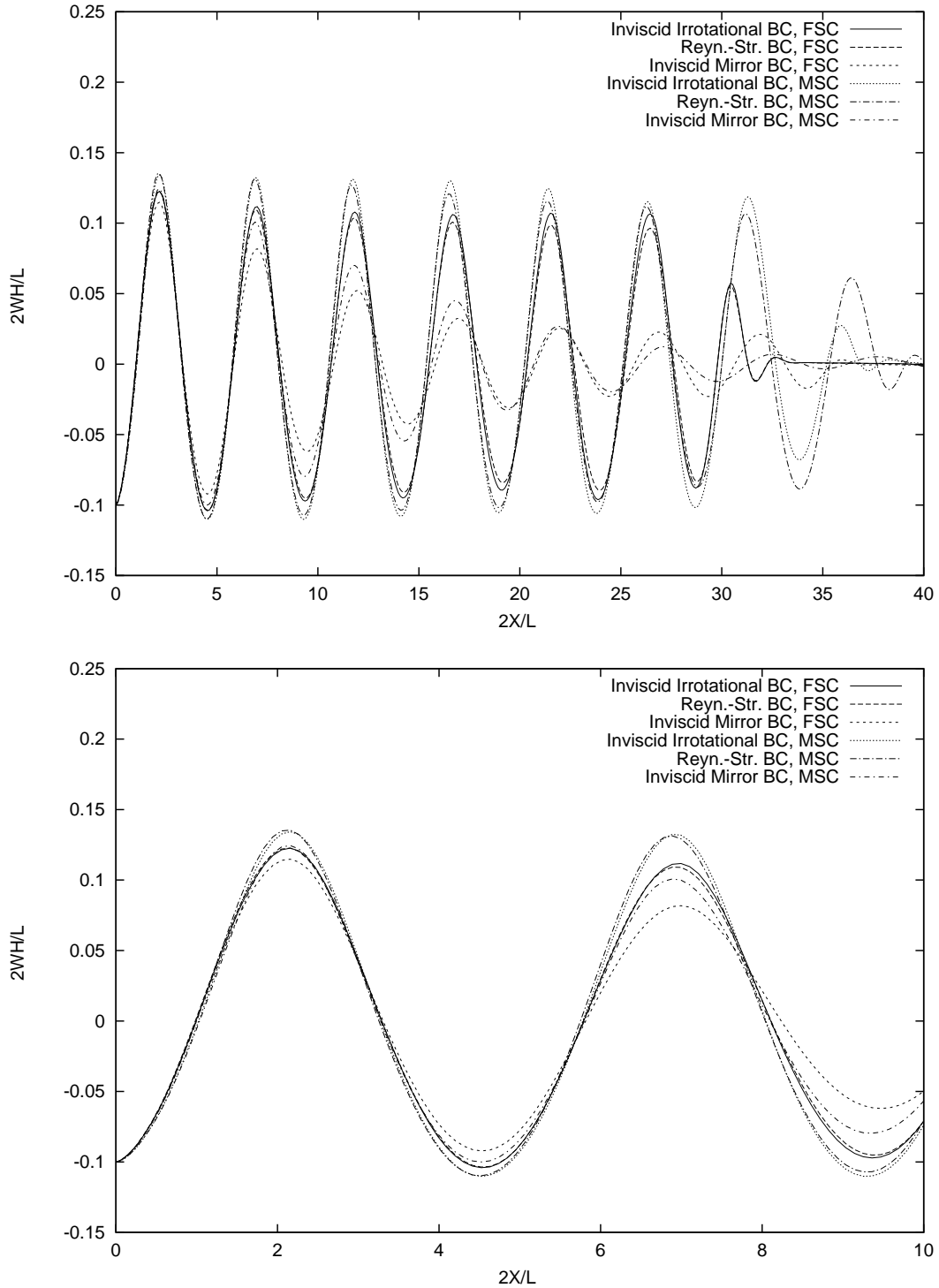
Figure 4.18: Computed wave profiles behind the transom of the model, *Ile*, at model scale (MSC, $Re_l = 3.732 \times 10^6$) and full scale (FSC, $Re_l = 9.442 \times 10^8$). The computations were carried out solving the RaNS equations using Chien's k-ϵ turbulence model and the inviscid irrotational, the Reynolds-stress and the inviscid mirror free-surface boundary conditions. $Fn_T = 2.8$.
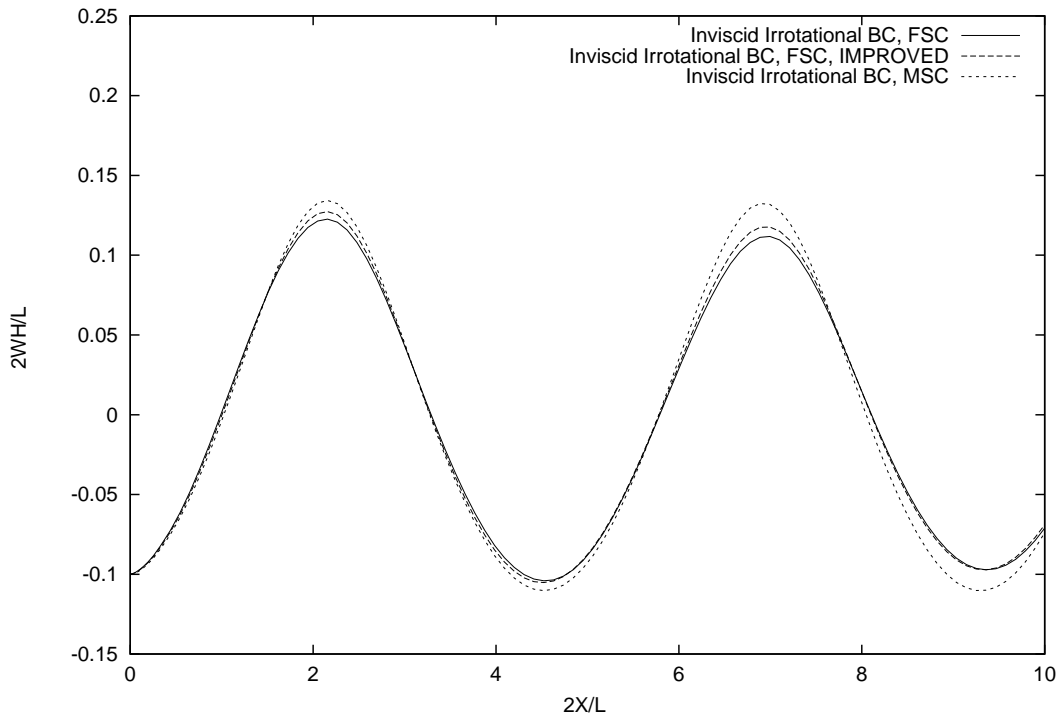
Figure 4.19: Computed wave profiles behind the transom of the model, *Ile*, at model scale (MSC, $Re_l = 3.732 \times 10^6$) and full scale (FSC, $Re_l = 9.442 \times 10^8$). The computations were carried out solving the RaNS equations using Chien's k-ϵ turbulence model and the inviscid irrotational free-surface boundary conditions. The grid, FINEFSC, was improved with respect to its orthogonality. $Fn_T = 2.8$.

Influence of the Reynolds Number on the Flow Field

In Figs. 4.20 up to 4.25, quantities of the flow field close to the transom are given for the Reynolds numbers, $Re_l = 3.732 \times 10^6$ and 9.442×10^8. The computations were conducted solving the RaNS equations using Chien's k-ϵ turbulence model, the Reynolds-stress free-surface boundary conditions and the grids, FINE and FINEFSC. The momentum, $\rho|\vec{V}|$, the turbulent kinetic energy, ρk, and the vorticity, $\partial u/\partial z - \partial w/\partial x$, are made nondimensional by referring them to ρU_∞, ρU_∞^2 and $U_\infty/0.5L$, respectively.

The results with respect to the nondimensional momentum (Fig. 4.20) show no significant difference. At full scale, the boundary layer at the transom is clearly thinner than the one at model scale, and the extension of low-velocity regions is less pronounced.

The nondimensional turbulent kinetic energy is significantly increased at model scale (Fig. 4.21). It is convected from the boundary layer of the model, *Ile*, into the waves behind the transom. Due to the velocity gradient and the convected turbulence, the waves cause a production of the turbulent kinetic energy according to Eq. (2.10). Therefore, the convected turbulent kinetic energy is amplified below the wave crest. At full scale, in the transom wave, the dimensional value of the turbulent kinetic energy is increased by 10 to 15 times compared with the one at model scale. In association with a lower surface tension, this might be one cause for small instabilities at full scale resulting in an breaking wave which does not appear at model scale.

The nondimensional turbulent viscosity, μ_T/μ, is significantly increased in the waves both at model and full scale (Fig. 4.23) compared with the one in the boundary layer at the wall of the model, *Ile*. Its maximum value is not located there where the turbulent kinetic energy is highest. As the turbulent viscosity is also dependent on the dissipation of the turbulent kinetic energy, its maximum value is located there where k^2/ϵ is highest.

The nondimensional vorticity distributions are quite similar at model and full scale (Fig. 4.24). At model scale, due to the increased influence of the viscosity on the flow, the extension of the nondimensional vorticity is little larger than at full scale. A significant difference is observed at the immediate vicinity of the transom (Fig. 4.25). There, at full scale, the nondimensional vorticity is about 100 times higher than the one at model scale, which is a result of the very high velocity gradient at the wall. Therefore, in this region, an oscillating behaviour of the flow might be possible at full scale which would not appear in model scale.
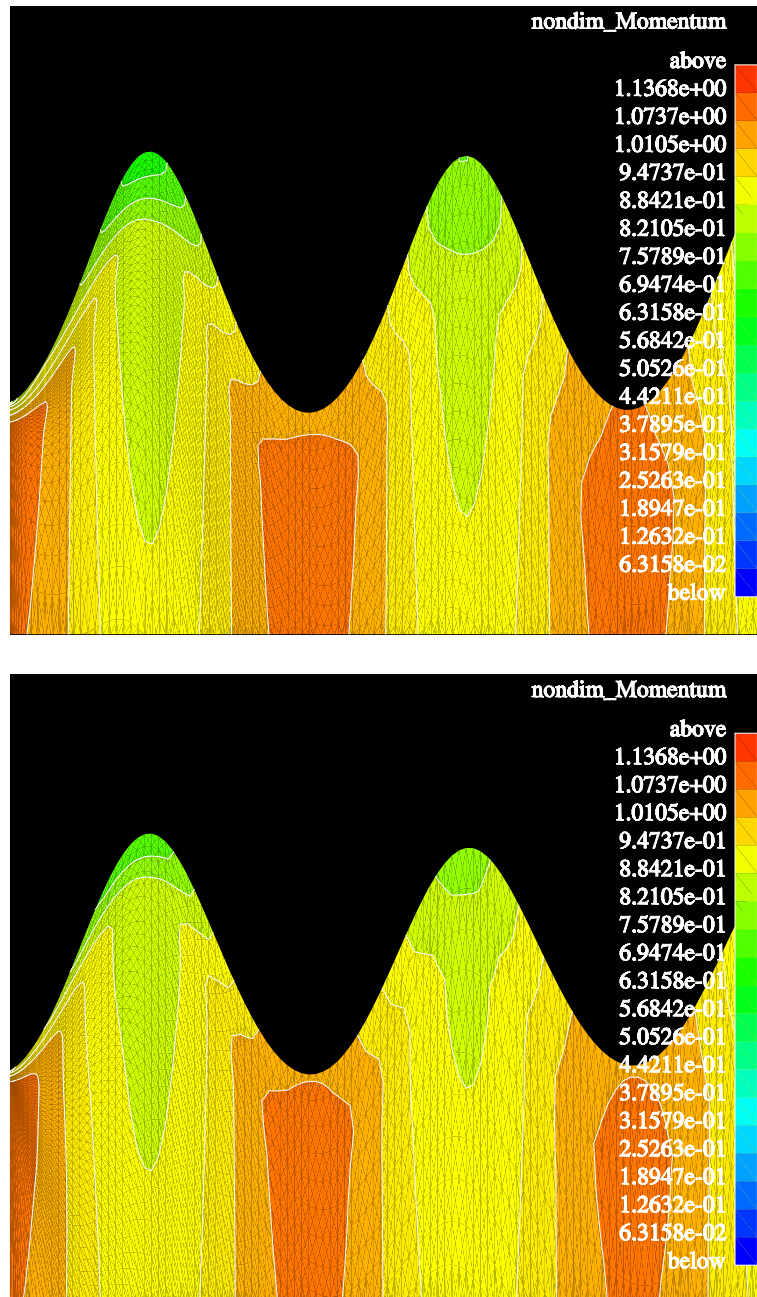
Figure 4.20: Computed nondimensional momentum behind the transom of the model, *Ile*, at model scale (Re_l =3.732×10^6, **top**) and full scale (Re_l =9.442×10^8, **bottom**). The computations were carried out solving the RaNS equations using Chien's k-ϵ turbulence model and the Reynolds-stress free-surface boundary conditions. $Fn_T = 2.8$. The pictures were compressed in the horizontal direction.
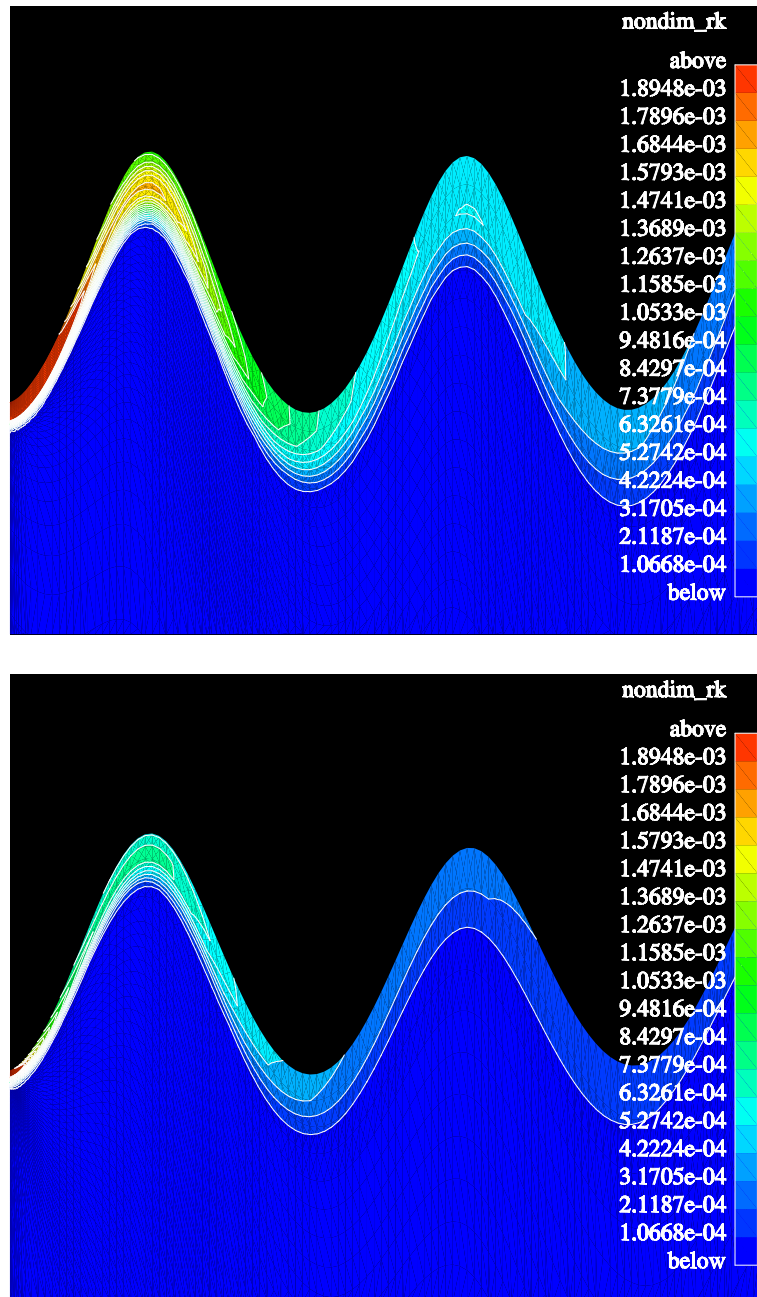
Figure 4.21: Computed nondimensional turbulent kinetic energy, $\rho k/(\rho U_\infty^2)$, behind the transom of the model, *Ile*, at model scale (Re_l =3.732×10^6, **top**) and full scale (Re_l =9.442×10^8, **bottom**). The computations were carried out solving the RaNS equations using Chien's k-ϵ turbulence model and the Reynolds-stress free-surface boundary conditions. $Fn_T = 2.8$. The pictures were compressed in the horizontal direction.

Figure 4.22: Computed turbulent kinetic energy, ρk, behind the transom of the model, *Ile*, at model scale ($Re_l =3.732\times10^6$, **top**) and full scale ($Re_l =9.442\times10^8$, **bottom**). The computations were carried out solving the RaNS equations using Chien's k-ϵ turbulence model and the Reynolds-stress free-surface boundary conditions. $Fn_T = 2.8$. The pictures were compressed in the horizontal direction.
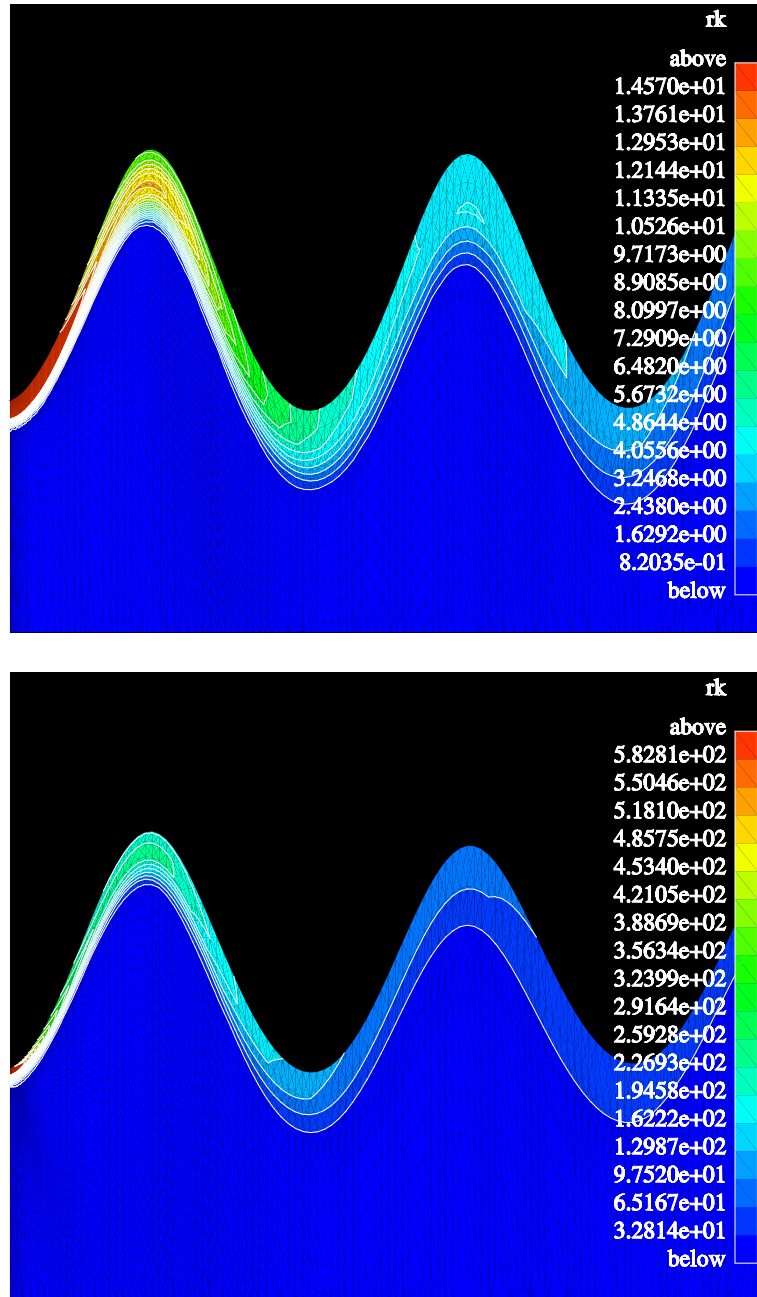
Figure 4.23: Computed nondimensional turbulent viscosity, μ_T/μ, behind the transom of the model, *Ile*, at model scale ($Re_l = 3.732 \times 10^6$, **top**) and full scale ($Re_l = 9.442 \times 10^8$, **bottom**). The computations were carried out solving the RaNS equations using Chien's k-ϵ turbulence model and the Reynolds-stress free-surface boundary conditions. $Fn_T = 2.8$. The pictures were compressed in the horizontal direction.
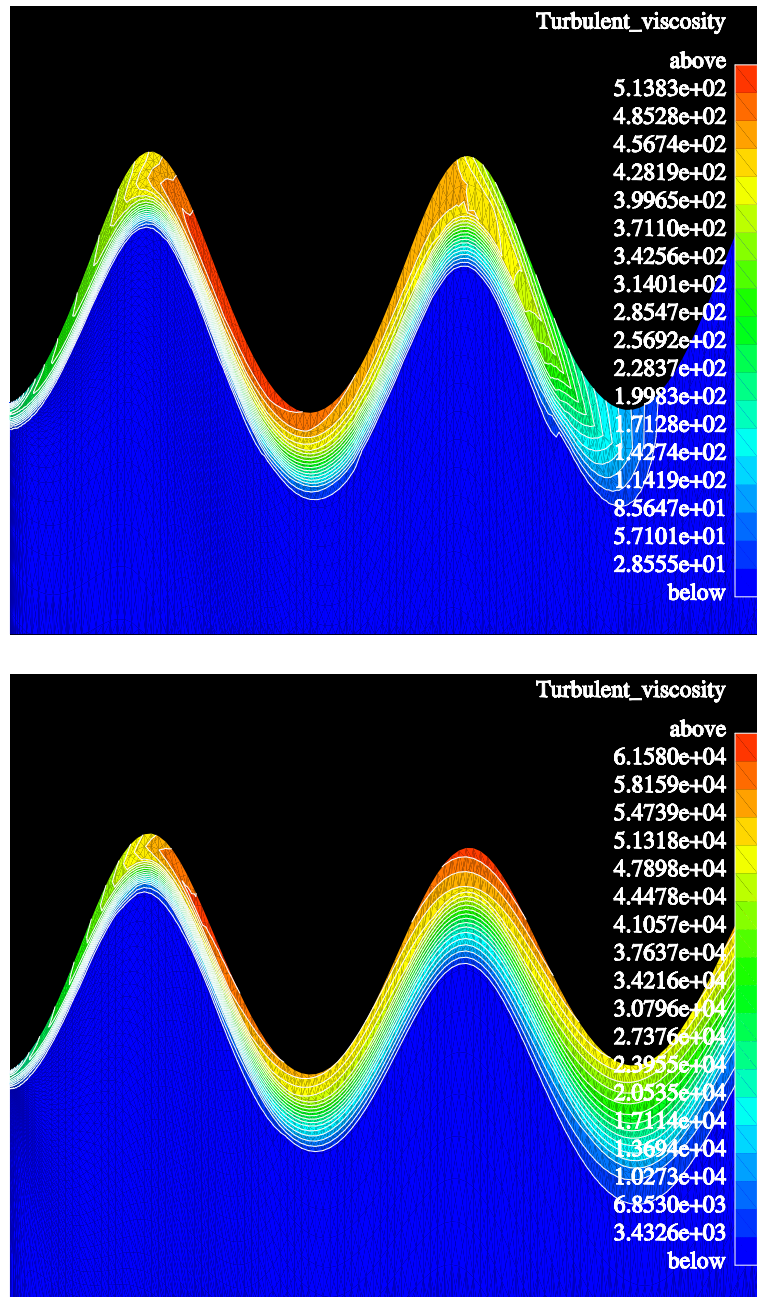
Figure 4.24: Computed nondimensional vorticity, γ^*, behind the transom of the model, *Ile*, at model scale ($Re_l = 3.732 \times 10^6$, **top**) and full scale ($Re_l = 9.442 \times 10^8$, **bottom**). The computations were carried out solving the RaNS equations using Chien's k-ϵ turbulence model and the Reynolds-stress free-surface boundary conditions. $Fn_T = 2.8$. The pictures were compressed in the horizontal direction.
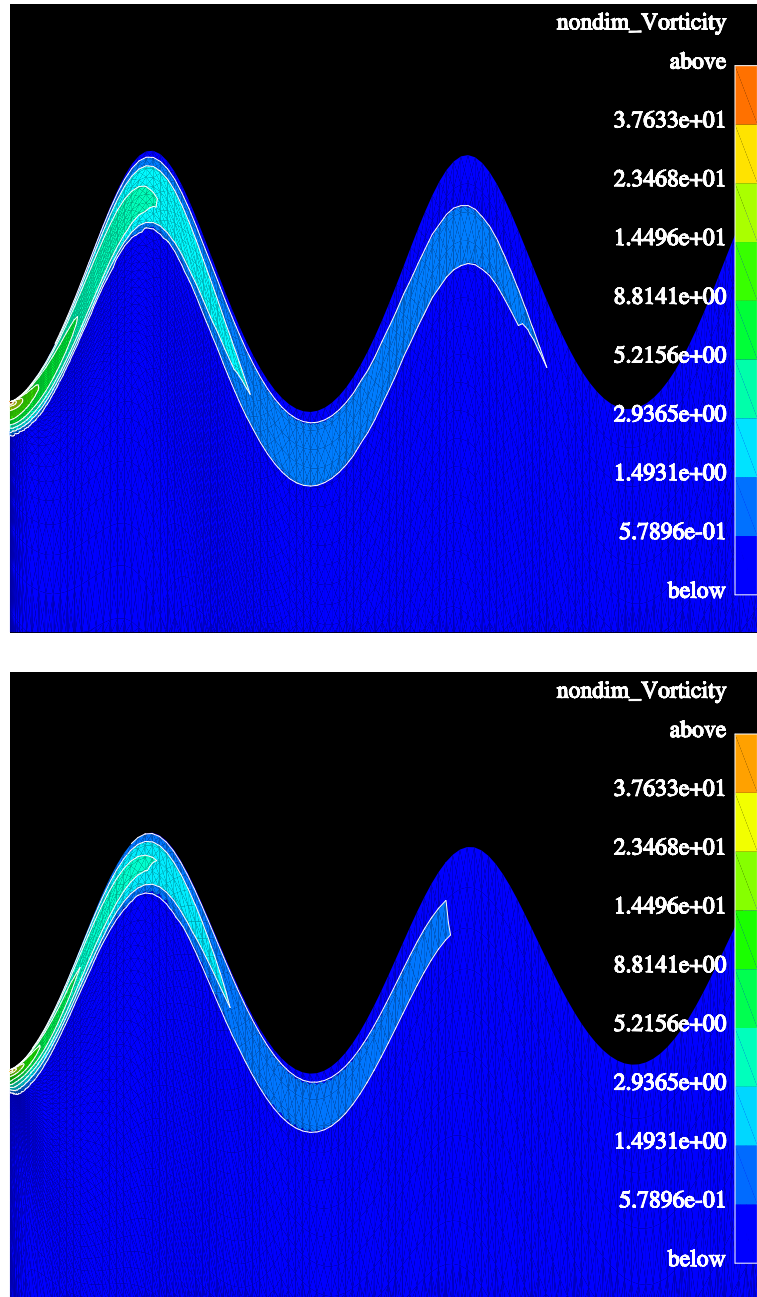
Figure 4.25: Computed nondimensional vorticity, γ^*, at the transom of the model, *Ile*, at model scale ($Re_l = 3.732 \times 10^6$, **top**) and full scale ($Re_l = 9.442 \times 10^8$, **bottom**). The computations were carried out solving the RaNS equations using Chien's k-ϵ turbulence model and the Reynolds-stress free-surface boundary conditions. $Fn_T = 2.8$. The pictures were compressed in the horizontal direction.
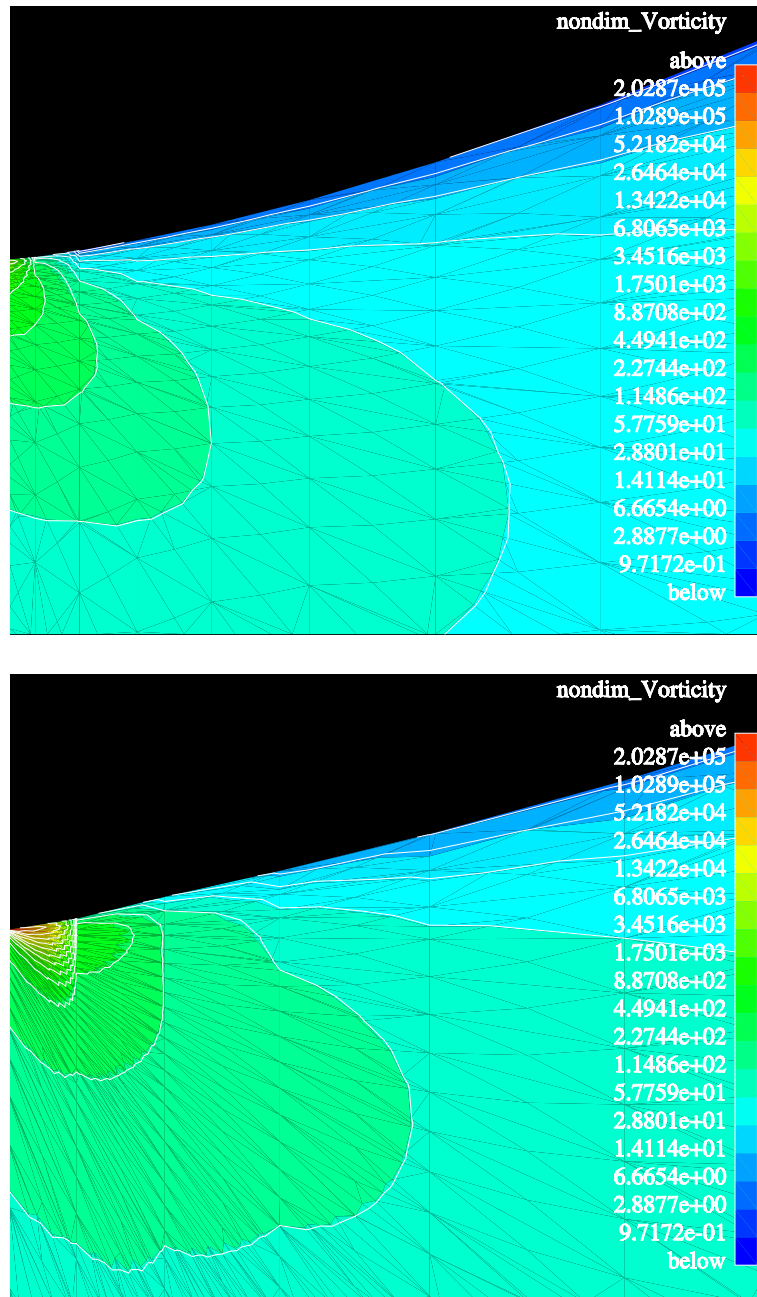
4.3.3 Resistance

In Table 4, the computed drag, the pressure resistance and the mean skin friction resistance coefficients are presented for the Reynolds number, $Re_l = 3.732 \times 10^6$. The respective Froude number, Fn_T, is equal to 2.8. The measured drag coefficient, *Aho and Schweighofer (1995)*, is given in the last row.

The drag coefficient is defined as

$$C_D = \frac{R_T}{0.5\rho U_\infty^2 A} \ , \tag{4.14}$$

where R_T is the total resistance, and A is the wetted surface. In naval applications, the drag coefficient, C_D, is denoted as total resistance coefficient, C_T. The pressure coefficient is defined as

$$C_P = \frac{R_P}{0.5\rho U_\infty^2 A} = \frac{\int_A -p_{wall}n_x dA}{0.5\rho U_\infty^2 A} \ , \tag{4.15}$$

where R_P is the pressure resistance of the model. p_{wall} is the pressure acting on the wall, and n_x is the x-component of the unit normal vector pointing from the wall into the computational domain. The computed mean skin friction coefficient is defined as

$$C_F = \frac{R_F}{0.5\rho U_\infty^2 A} = \frac{\int_A \tau_{wall}t_x dA}{0.5\rho U_\infty^2 A} \ , \tag{4.16}$$

where R_F is the mean skin friction resistance of the model. t_x is the x-component of the tangential unit vector on the hull pointing backwards from the bow to the stern.

The computed total, pressure and skin friction coefficients obtained with different free-surface boundary conditions at model scale are given for the coarse grid, FINE, and the finer one, FINEST (Table 4). In Table 5, the respective full-scale results for $Re_l = 9.442 \times 10^8$, are given for the coarse grid, ROUGHFSC, and the finer one, FINEFSC. In the following, the influence of the grid resolution on the results is evaluated, and the effect of the different free-surface boundary conditions on the resistance coefficients is discussed.

At model scale, the resistance coefficients obtained from the computations for the grids, FINE and FINEST, do not differ more than about one percent (Table 4). Therefore, these resistance coefficients may be regarded as independent of the grid resolution. The computed total resistance coefficents obtained with Chien's k-ϵ turbulence model are about 60 percent lower than the experimental one, *Aho and Schweighofer (1995)*. The reason for this remarkable difference is given by the fact that in the experiment the bow wave

was present and in the computations not. This confirms again the significant influence of the bow wave on the results. The viscous and inviscid irrotational free-surface boundary conditions give a very small difference between the computed resistance coefficients. Comparing the results for the viscous and inviscid irrotational free-surface boundary conditions with the ones for the inviscid mirror ones, a moderate difference of three percent is obtained.

At full scale, the mean skin friction resistance coefficients, C_F, obtained from the computations for the grids, ROUGHFSC and FINEFSC, do not differ more than about five percent (Table 5). The grid, FINEFSC, is very similar to the grid, FLATF, of the flat-plate computations (Section 4.1.2). The grid, FLATF, was already sufficient for a grid independent solution. Therefore, it may be expected that a refinement of the grid, FINEFSC, will have a negligible effect on the computation of the mean skin friction coefficient. The pressure resistance coefficients, C_P, obtained from the computations for the grids, ROUGHFSC and FINEFSC, do not differ more than by about seven percent (Table 5). Close to the transom, the computed wave profile may be assumed as independent of the grid resolution for the grid, FINEFSC (Fig. 4.17). The pressure along the hull is mainly determined by the convection terms of the RaNS equations. The convection terms are discretized by a scheme of third-order accuracy. Therefore, a refinement of the grid, FINEFSC, will cause a very small change of the pressure resistance coefficient. All in all, the resistance coefficients obtained for the grid, FINEFSC, may be regarded as almost independent of the grid resolution. The viscous and the inviscid irrotational free-surface boundary conditions give almost the same results. The difference between these boundary conditions and the inviscid mirror ones accounts for about three percent, similarly to the computations at model scale.

Table 4: Resistance coefficients obtained from the computations for the grids, FINE and FINEST. The computations were performed using Chien's k-ϵ turbulence model and the inviscid and viscous free-surface boundary conditions. The experimental value was taken from *Aho and Schweighofer (1995)*. $Fn_T = 2.8$. $Re_l = 3.732 \times 10^6$.

Case	FINE			FINEST		
Resistance coeff., $\times 10^3$	C_D	C_P	C_F	C_D	C_P	C_F
Euler, inviscid mirror BC	5.865	5.865		5.875	5.875	
Euler, tang.-str. BC	6.038	6.038				
k-ϵ, inviscid mirror BC	10.13	6.143	3.986	10.205	6.228	3.978
k-ϵ, inviscid irrot. BC	10.454	6.466	3.988			
k-ϵ, tang.-str. BC	10.443	6.455	3.988	10.456	6.475	3.982
k-ϵ, Reyn.-str. BC	10.417	6.420	3.997	10.424	6.456	3.968
Experiment	27.72			27.72		

Table 5: Resistance coefficients obtained from the computations for the grids, ROUGHFSC and FINEFSC. The computations were performed using Chien's k-ϵ turbulence model and the inviscid and the Reynolds-stress free-surface boundary conditions. $Re_l = 9.442 \times 10^8$.

Case	ROUGHFSC			FINEFSC		
Resistance coefficient, $\times 10^3$	C_D	C_P	C_F	C_D	C_P	C_F
k-ϵ, inviscid mirror BC	8.560	6.510	2.050	7.961	6.019	1.942
k-ϵ, inviscid irrot. BC	8.765	6.717	2.047	8.145	6.203	1.942
k-ϵ, inv. irrot. BC, improv.				8.192	6.251	1.940
k-ϵ, Reyn.-str. BC	8.665	6.617	2.048	8.112	6.168	1.943

Comparison of the Computed Resistance with the ITTC-57 Extrapolation Method

In Table 6, the computed resistance coefficients are compared with the ones of the ITTC-57 extrapolation method, *The Society of Naval Architects and Marine Engineers (1988)*. The computations were performed using Chien's k-ϵ turbulence model and the inviscid irrotational free-surface boundary conditions at $Re_l = 3.732 \times 10^6$ (MSC) and 9.442×10^8 (FSC). As the inviscid irrotational free-surface boundary conditions gave almost the same result as

the Reynolds-stress free-surface boundary conditions, and the numerical error is the smallest for the improved version of the grid, FINEFSC, these results may be used for the evaluation of the scaling process. The grids, FINE and FINEFSC, were used because of their similar resolutions in the x-directions giving the same accuracy for the computation of the pressure distribution along the hull. At model scale, the total resistance coefficient, C_D, of the ITTC-57 extrapolation method is equal to the computed total resistance coefficient. The mean skin friction coefficient according to the ITTC-57 model-ship correlation line, *The Society of Naval Architects and Marine Engineers (1988)*, is calculated from

$$C_{F,ITTC-57} = \frac{0.075}{(lgRe_l - 2)^2} \ . \tag{4.17}$$

Using the computed total resistance coefficient, C_D, and the calculated mean skin friction coefficient, $C_{F,ITTC-57}$, the residual resistance coefficient, C_R, of the ITTC-57 extrapolation method is calculated as

$$C_R = C_D - C_{F,ITTC-57} \ . \tag{4.18}$$

C_R is the same at model and full scale. At full scale, the total resistance coefficient of the ITTC-57 extrapolation method is calculated as

$$C_D = C_R + C_{F,ITTC-57} \ . \tag{4.19}$$

In the following, the first two lines of Table 6 are considered. At full scale, the total resistance coefficient, C_D, is overestimated by only two percent using the ITTC-57 extrapolation method. The agreement with the computed result is very good. Nevertheless, this result must be taken with caution.

At model scale, the flow was laminar over a range of about 2.5 percent of the model length, and transition took place within a region of 2.5 percent and 10.5 percent of the model length measured from the fore perpendicular in the positive x-direction. Generally, when using the ITTC-57 extrapolation method, the flow has to be fully turbulent at model and full scale. Therefore, at model scale, the computed result has to be corrected with respect to a fully turbulent flow. For the evaluation of the necessary correction with respect to a from the fore perpendicular fully turbulent flow, the local skin friction curves of *White (1991), Schweighofer (1997)*, and Blasius, *White (1991), Schweighofer (1997)*, are used. The curve of White is related to the fully turbulent flow over a smooth flat plate. The one of Blasius is related to the laminar flow over a smooth flat plate. Using these curves, the increase of the

the computed mean skin friction coefficient is obtained from

$$\Delta C_F = \frac{\int_0^{0.065 L_{pp}} (C_{f,White} - C_{f,Blasius}) dx}{L_{pp}} = 0.32 \times 10^{-3} \ , \qquad (4.20)$$

and the corrected total and mean skin friction resistance coefficients become

$$C_{D,Fullyturb.} = C_D + \Delta C_F \qquad (4.21)$$

and

$$C_{F,Fullyturb.} = C_F + \Delta C_F \ , \qquad (4.22)$$

respectively. The corrected results are presented in the third line of Table 6. In the last line, the full-scale results with respect to the corrected model-scale results are presented. There, the ITTC-57 extrapolation method gives a total resistance coefficient, C_D, being overestimated by about 6.5 percent compared with the one of the full-scale computation.

Recognizable differences are obtained for the computed pressure and mean skin friction resistance coefficients compared with the residual and mean skin friction resistance coefficients of the ITTC-57 extrapolation method. At model scale, in the partly laminar case, the residual resistance coefficient, C_R, is about five percent greater than the computed pressure resistance coefficient, C_P (first line of Table 6). The value for the fully turbulent case is even about eleven percent greater (third line of Table 6). At full scale, the differences are more pronounced. With respect to the partly laminar case at model scale, it is about ten percent (second line of Table 6). With respect to the fully turbulent case at model scale, it is about fifteen percent (last line of Table 6). Therefore, the residual resistance coefficient includes a certain amount of viscosity effects, which are little more pronounced at full scale than at model scale.

The skin friction coefficient of the ITTC-57 model-ship correlation line is of a smaller value than the computed ones, and, at model scale, it is about four percent greater than the one of a flat plate. At full scale, its deviation from the value of a flat plate is about one percent.

The pressure resistance coefficient of the computations, C_P, changes very little with the Reynolds number. The difference is about three percent. It is explained partly by the influences of the different grids. Another reason is given by the boundary-layer effect, *Schlichting (1979)*, which causes a less pronounced pressure peak at the shoulder at model scale. At full scale and particularly for the solution of the Euler equations (see Table 4), the pressure reaches a greater negative value at the shoulder. Therefore, the pressure

resistance coefficient is also smaller compared with the one at model scale, which is physically correct.

Table 6: Resistance coefficients obtained from the computations for the grid, FINE, and the improved grid, FINEFSC. Further, the resistance coefficients with respect to the ITTC-57 extrapolation method are given. The computations were performed using Chien's k-ϵ turbulence model and the inviscid irrotational free-surface boundary conditions. $Re_l = 3.732 \times 10^6$ (MSC) and 9.442×10^8 (FSC). At model scale, the computed result was corrected with respect to a fully turbulent flow (Fully turb., comp., MSC). The respective results are given in the last two rows.

Case	Computation			ITTC-57		
Resistance coeff., $\times 10^3$	C_D	C_P	C_F	C_D	C_R	C_F
k-ϵ, inv. BC, MSC	10.454	6.466	3.988	10.454	6.866	3.588
k-ϵ, inv. BC, imp., FSC	8.192	6.251	1.940	8.408	6.866	1.542
Fully turb., comp., MSC	10.774	6.466	4.308	10.774	7.186	3.588
k-ϵ, inv. BC, imp., FSC	8.192	6.251	1.940	8.728	7.186	1.542

Comparison of the Computed Resistance with the ITTC-78 Extrapolation Method

In Table 7, the computed resistance coefficients are compared with the ones of the ITTC-78 extrapolation method, *The Society of Naval Architects and Marine Engineers (1988)*. The computed results are the same as the ones of the discussion with respect to the ITTC-57 extrapolation method. At model scale, the resistance coefficients of the ITTC-78 extrapolation method are equal to the ones of the partly laminar computation (first line of Table 7) and the corrected computation with respect to a fully turbulent flow (third line of Table 7). The viscous resistance coefficient,

$$C_v = (1 + k)C_{F,ITTC-57} \; , \tag{4.23}$$

of the ITTC-78 extrapolation method is replaced by the skin friction resistance coefficient,

$$C_F = (1 + k)C_{F,ITTC-57} \; . \tag{4.24}$$

The form factor, k, takes into account the influence of the hull form on the frictional resistance only. This is not exactly in agreement with the ITTC-78

extrapolation method of *The Society of Naval Architects and Marine Engineers (1988)*. There, also the form influence on the pressure resistance due to the viscosity of the flow is taken into account by the form factor determined by several model tests. Nevertheless, it was not possible to carry out reliable computations at very low Froude numbers. Therefore, an estimation of the form factor according to the rules is not possible, and instead, the deviation of the computed skin friction resistance coefficient from the ITTC-57 model-ship correlation line is used for the estimation of the form factor. The form factor, k, is obtained from

$$k = \frac{C_F}{C_{F,ITTC-57}} - 1 \ , \tag{4.25}$$

where C_F is the computed mean skin friction coefficient, and $C_{F,ITTC-57}$ is the mean skin friction coefficient according to the ITTC-57 model-ship correlation line, *The Society of Naval Architects and Marine Engineers (1988)*, given by Eq. (4.17). As the total resistance and the mean skin friction resistance coefficients of the computation and the ITTC-78 extrapolation method are the same at model scale, the residual resistance coefficient, C_R, is equal to the pressure resistance coefficient, C_P, of the computations. Therefore, very little viscosity influences are contained in the residual resistance coefficient. The residual resistance coefficient is the same at model and full scale. In the partly laminar case, the form factor, k, accounts for 0.111 (first line of Table 8), and it is the same at model and full scale. The correction for a from the fore pendicular fully turbulent flow gives the form factor, $k = 0.201$ (second line of Table 8). At full scale, the total resistance coefficient, C_D, of the ITTC-78 extrapolation method is obtained from

$$C_D = C_R + C_F \ , \tag{4.26}$$

where C_R is the residual resistance coefficient of the model, and C_F is calculated from Eq. (4.24) using the form factor, k, of the model. The obtained total resistance coefficient, C_D, is almost exactly the same as the one of the computation. The corrected value is about 1.5 percent greater than the one of the computation (last line of Table 7). At full scale, the residual resistance coefficient is about three percent greater than the computed pressure coefficient (last line of Table 7). Therefore, a very small amount of additional viscosity influences are included in the residual resistance coefficient. For the fully turbulent case, the computed mean skin friction coefficient and the one of the ITTC-78 extrapolation method are with about 4.5 percent very close to each other (last line of Table 7).

In Table 8, the form factors with respect to the ITTC-57 model-ship correlation line, *The Society of Naval Architects and Marine Engineers (1988)*, and the mean skin friction curve of a fully turbulent flow over a flat plate (ESD), *Royal Aeronautical Society (1968)*, are given. Using the ITTC-57 model-ship correlation line for the evaluation of $C_{F,ITTC-57}$ in Eq. (4.25), the form factor is different at model and full scale. The laminar flow at the bow is one cause for the obtained difference (first line of Table 8). Having corrected the result for a fully turbulent flow (second line of Table 8), the form factors at model and full scale are quite close to each other. The remaining difference is caused by the nature of the ITTC-57 model-ship correlation line, which includes already a certain form factor at model scale. Therefore, at model scale, the form factor is little smaller than the one at full scale. This is confirmed by the obtained results with respect to the mean skin friction curve of a flat plate. There, the respective mean skin friction coefficients of the ESD were used in Eq. (4.25) instead of $C_{F,ITTC-57}$. The obtained form factor is almost exactly the same at model and full scale (second row and last two lines of Table 8). Again, the influence of the laminar region at the bow causes a smaller mean skin friction coefficient and, therefore, a smaller form factor (second row and first line of Table 8).

For the full-scale ship, the agreement of the computed total resistance coefficient with the one of the modified ITTC-78 extrapolation method is excellent. The ITTC-57 extrapolation method gives a slightly overpredicted value. Taking into account that the computed result will be little increased when the grid influences vanish, the computed result is improved with respect to the used extrapolation methods. The used extrapolation methods are assumed to work well for simple cases. The computed case is simple as no flow separation with backflow occurs. Also, the hull is rather thin in the z-direction, and the influence of the viscosity on the pressure resistance is very small. Therefore, the used extrapolation methods may be assumed to be appropriate for this particular case, and the scaling of the resistance coefficients may be assumed as quite well reproduced.

Table 7: Resistance coefficients obtained from the computations for the grid, FINE, and the improved grid, FINEFSC. Further, the resistance coefficients with respect to the ITTC-78 extrapolation method are given. The computations were performed using Chien's k-ϵ turbulence model and the inviscid irrotational free-surface boundary conditions. $Re_l = 3.732 \times 10^6$ (MSC) and 9.442×10^8 (FSC). At model scale, the computed result was corrected with respect to a fully turbulent flow (Fully turb., comp., MSC). The respective results are given in the last two rows.

Case	Computation			ITTC-78		
Resistance coeff., $\times 10^3$	C_D	C_P	C_F	C_D	C_R	C_F
k-ϵ, inv. BC, MSC	10.454	6.466	3.988	10.454	6.466	3.988
k-ϵ, inv. BC, imp., FSC	8.192	6.251	1.940	8.179	6.466	1.713
Fully turb., comp., MSC	10.774	6.466	4.308	10.774	6.466	4.308
k-ϵ, inv. BC, imp., FSC	8.192	6.251	1.940	8.317	6.466	1.851

Table 8: The form factor, k, with respect to the ITTC-57 model-ship correlation line, *The Society of Naval Architects and Marine Engineers (1988)* and the mean skin friction line of a flat plate (ESD), *Royal Aeronautical Society (1968)*. The computations were performed using Chien's k-ϵ turbulence model and the inviscid irrotational free-surface boundary conditions. $Re_l = 3.732 \times 10^6$ (MSC) and 9.442×10^8 (FSC). At model scale, the computed result was corrected with respect to a fully turbulent flow (Fully turbulent, comp., MSC).

	Form factor, k	
Reference	ITTC-57	Flat plate, ESD
k-ϵ, inv. irrot. BC, MSC	0.111	0.156
Fully turbulent, comp., MSC	0.201	0.249
k-ϵ, inv. irrot. BC, imp., FSC	0.258	0.244

4.3.4 Convergence

In Figs. 4.26 and 4.27, the convergence histories of the computations associated with the inviscid mirror and Reynolds-stress free-surface boundary conditions are presented. The computations were carried out at model scale. Considering the drag coefficient, C_D, and the L_2-norms of the turbulence quantities, no difference in the convergence duration can be observed. For the L_2-norms of the density, the x-momentum and the z-momentum, the inviscid mirror free-surface boundary conditions give a faster convergence than the Reynolds-stress free-surface boundary conditions. The ship hydrodynamicist is mainly interested in the converged result for the drag coefficient. Therefore, concerning the convergence, it makes no difference whether the inviscid mirror or the viscous free-surface boundary conditions are used. This holds also for the inviscid irrotational free-surface boundary conditions.

At full scale, the change of the drag coefficient shows no change anymore. The L_2-norms of the density, the x-momentum and the z-momentum are reduced to 1×10^{-5}, 3×10^{-7} and 1×10^{-7}, respectively. The L_2-norms of the turbulent kinetic energy and the dissipation of the turbulent kinetic energy are reduced to 4×10^{-8} and 1×10^{-4}, respectively. The maximum change of the pressure in the flow field is reduced from 1.5×10^6 to 4×10^{-1}.
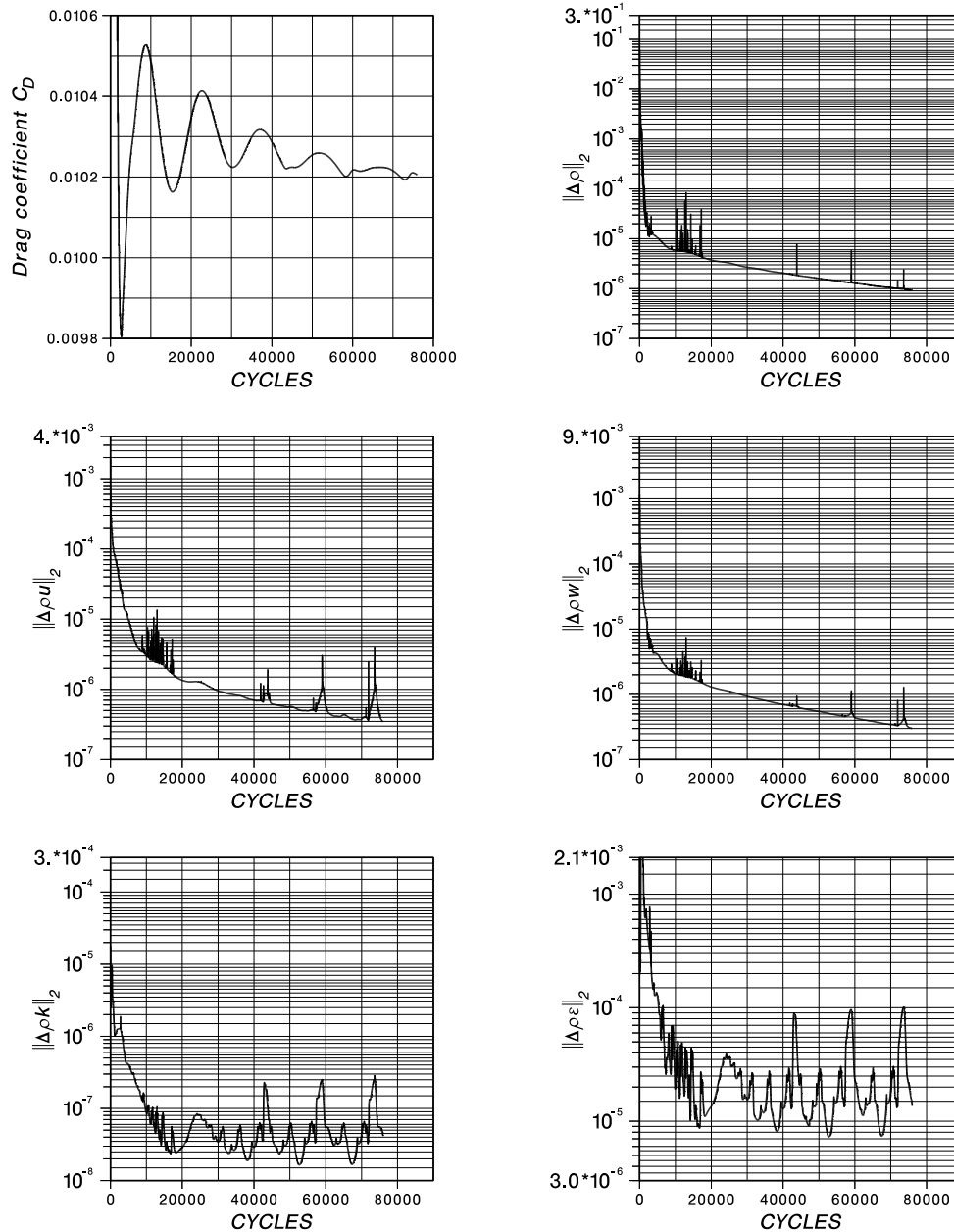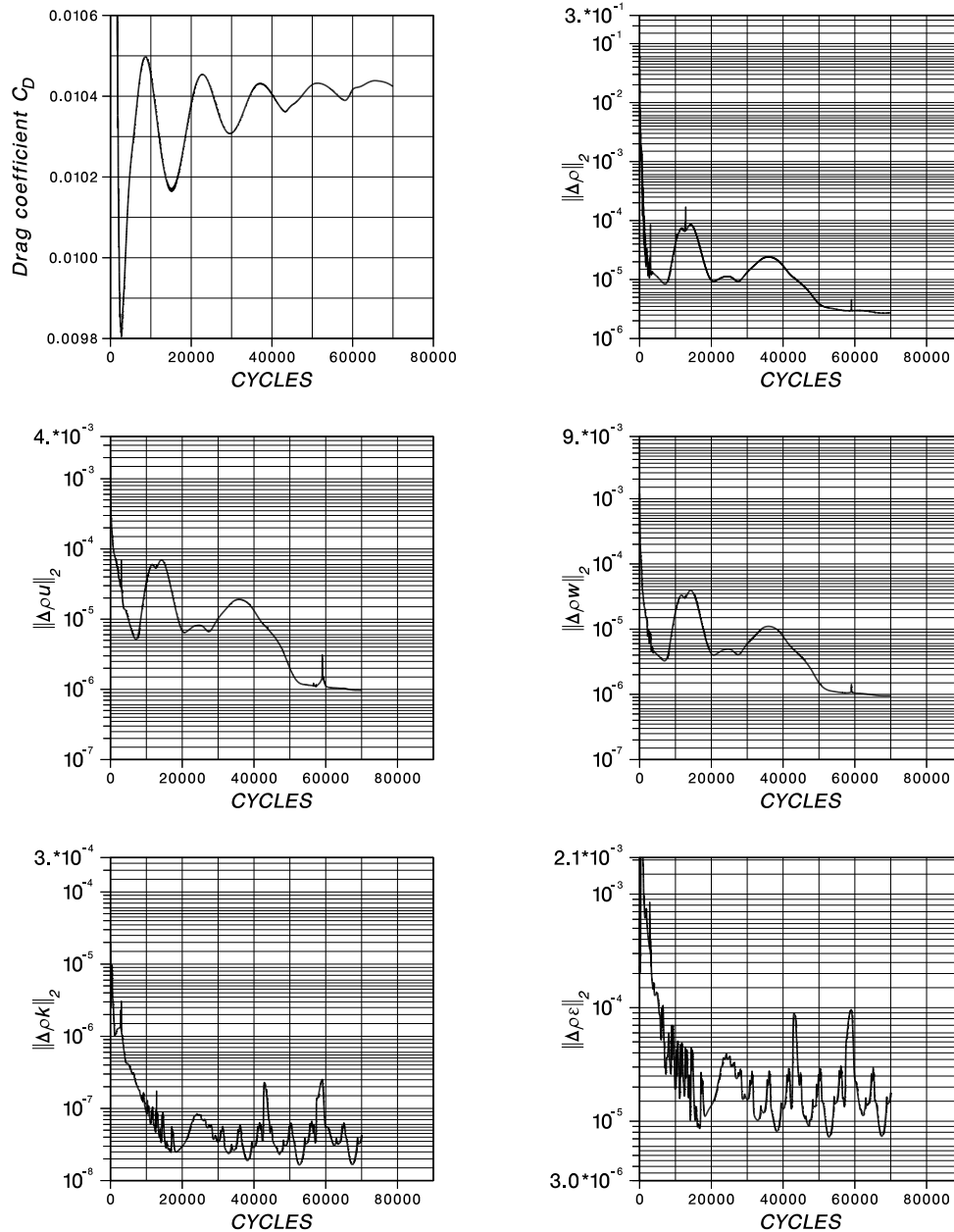
Figure 4.26: Convergence history for the model, *Ile*. The computation was performed solving the RaNS equations using Chien's k-ϵ turbulence model and the inviscid mirror free-surface boundary conditions. The used grid was FINEST. C_D is the drag coefficient. The other quantities are the L_2-norms of the residuals of the density, ρ, the x-momentum, ρu, the z-momentum, ρw, the turbulent kinetic energy, k, and the dissipation of the turbulent kinetic energy, ϵ. $Fn_T = 2.8$. $Re_l = 3.732 \times 10^6$.

Figure 4.27: Convergence history for the model, *Ile.* The computation was performed solving the RaNS equations using Chien's k-ϵ turbulence model and the Reynolds-stress free-surface boundary conditions. The used grid was FINEST. C_D is the drag coefficient. The other quantities are the L_2-norms of the residuals of the density, ρ, the x-momentum, ρu, the z-momentum, ρw, the turbulent kinetic energy, k, and the dissipation of the turbulent kinetic energy, ϵ. $Fn_T = 2.8$. $Re_l =3.732 \times 10^6$.

4.4   Froude Number, $Fn_T = 2.3$

In this section, the computed results for the transom wave, the drag coefficient and the convergence are presented for the Froude number, 2.3. The computations were performed solving the Euler and the RaNS equations using Chien's k-ϵ turbulence model and the inviscid and viscous free-surface boundary conditions. The used grid was FINE. The Reynolds number was 3.066×10^6.

4.4.1   Wave Profile

In Fig. 4.28, the computed wave profiles behind the transom of the model, *Ile*, are presented. With the exception of the inviscid irrotational free-surface boundary conditions, qualitatively, the results are similar to the ones obtained for the Froude number, 2.8. Compared with the viscous free-surface boundary conditions, the application of the inviscid mirror free-surface boundary conditions gives an about 5 percent smaller wave height at the transom and a much stronger damping of the waves farther downstream. The reduction of both the Froude number and the Reynolds number increases the influence of the viscosity on the results. This can be observed very well in the case of the inviscid mirror free-surface boundary conditions (Figs. 4.28 and 4.29). There, the viscosity of the flow causes a higher and steeper wave at the transom than the solution of the Euler equations. Also the appearing phase shift and damping are more strongly pronounced. The difference between the solutions of the RaNS equations with the viscous and inviscid mirror free-surface boundary conditions and the solution of the Euler equations with the inviscid mirror free-surface boundary conditions is caused by the different boundary conditions and the viscous terms appearing in the RaNS equations. For the Froude number, 2.8, the influence of the viscosity terms was very small (Fig. 4.29).

The solutions of the RaNS equations using the tangential- and Reynolds-stress free-surface boundary conditions are again almost identical. Therefore, the inclusion of the Reynolds stresses into the pressure equation (Eqs. 2.41 and 2.42) has also in this case almost no influence on the solution.

For the Froude number, 2.8, the inviscid irrotational free-surface boundary conditions gave almost exactly the same result as the viscous free-surface boundary conditions (Fig. 4.29). For the Froude number, 2.3, a moderate difference is obtained. The inviscid irrotational free-surface boundary conditions give an about four percent higher wave profile at the transom than the viscous ones, and the solution is less dampened farther downstream. The in-

fluence of the viscosity through the free-surface boundary conditions on wave making is obvious, and it makes a slight difference whether the free-surface is treated as the free surface of an inviscid or viscous flow. The obtained result is in agreement with the finding of *Jeong and Doi (1995)*. They pointed out that a high curvature of the bow wave will give a dampened wave when the tangential stresses are set to zero on the free surface in comparison with the zero-gradient condition. *Hinatsu (1992)* points out that the application of the zero-stress condition is essential for waves at intermediate Reynolds numbers. In Fig. 4.28, it is shown that it is essential at even relatively high Reynolds numbers.

Influence of the Froude Number on the Wave Profile

In Figs. 4.29 and 4.30, the influence of the Froude number on the wave profile is investigated.

A reduction of both the Froude number and the Reynolds number increases the wave height and the steepness of the waves (Fig. 4.29). The influence of the viscosity terms appearing in the RaNS equations becomes more pronounced. From Eq. (4.1), it is obvious that a decreased Froude number gives a shorter wave length. For both presented Froude numbers, the computations are performed using the grid, FINE. Therefore, the resolution of the wave is lower for the Froude number, 2.3, than for the Froude number, 2.8. This causes also the stronger numerical damping of the solution at the lower Froude number.

In Fig. 4.30, the computed transom waves are presented for the Froude numbers, 2.1, 2.2, 2.3 and 2.8. The computations were performed solving the RaNS equations using Chien's k-ϵ turbulence model and the inviscid irrotational and Reynolds-stress free-surface boundary conditions. The results with respect to the Froude numbers 2.1 and 2.2 must be taken with caution as the applied boundary condition at the transom is not correct anymore, and the grid resolution is too poor. According to the measurements of *Saisto (1995)*, the wave height at the transom is not equal to the draught of the transom anymore. For the Froude number 2.1, the entire wave pattern could not be computed due to the appearance of instability at a certain stage of the computations. Nevertheless, the results may be used for a qualitative statement. The lower the Froude number is, the more significant is the difference between the results obtained with the different free-surface boundary conditions. For the Froude number, 2.8, the viscosity has no influence on the transom wave through the free-surface boundary conditions. For the lower Froude numbers, the steepness and curvature of the transom waves

are increased, and the influence of the viscosity on wave making through the free-surface boundary conditions is already very obvious. Also the departure of the sinus and trochoidal form of the waves in direction to an overturning one may be clearly observed.
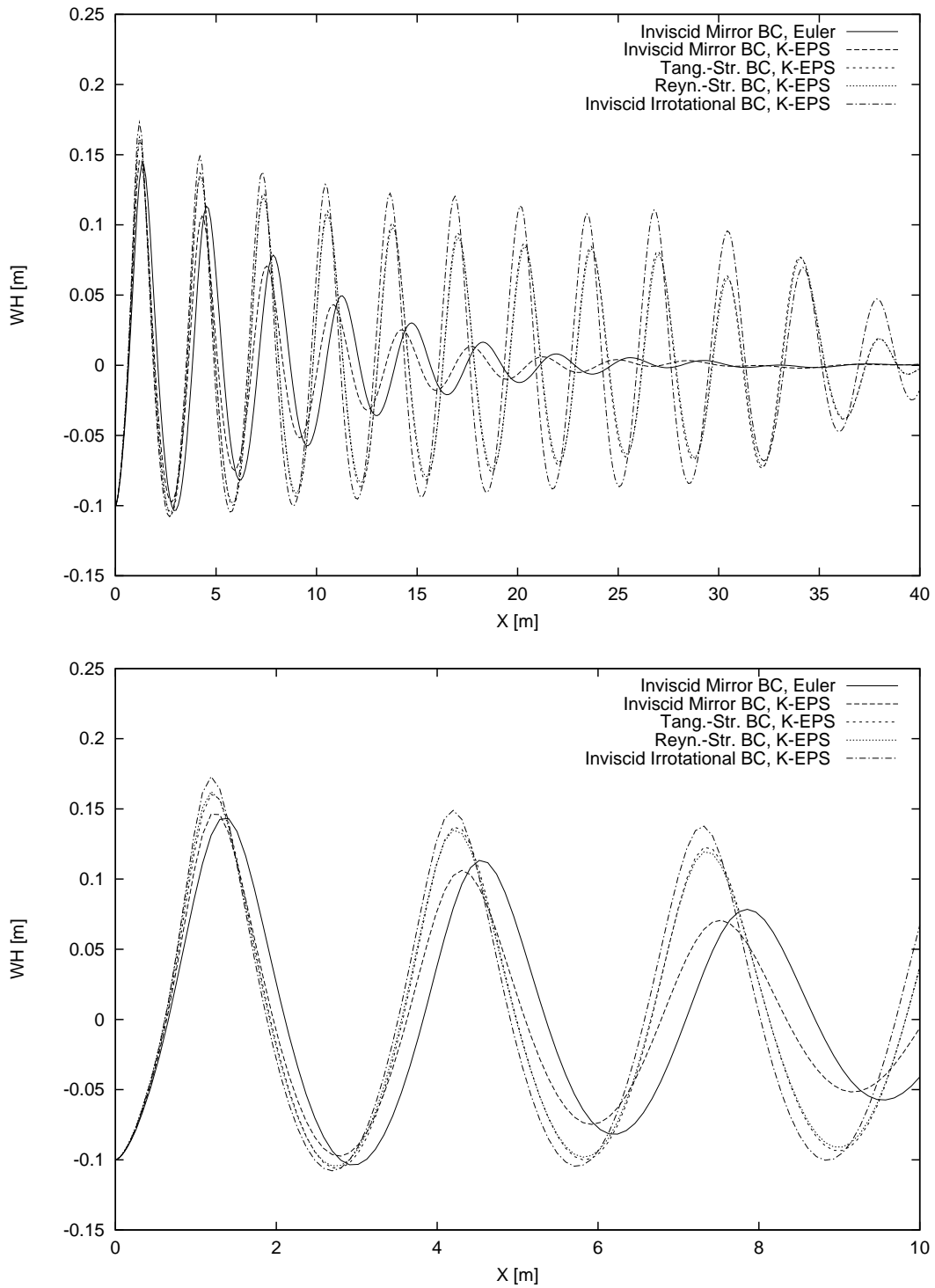
Figure 4.28: Computed wave profiles behind the transom of the model, *Ile*. The computations were carried out solving the Euler and the RaNS equations using Chien's k-ϵ turbulence model and the inviscid and viscous free-surface boundary conditions. The used grid was FINE. $Fn_T = 2.3$. $Re_l = 3.066 \times 10^6$.
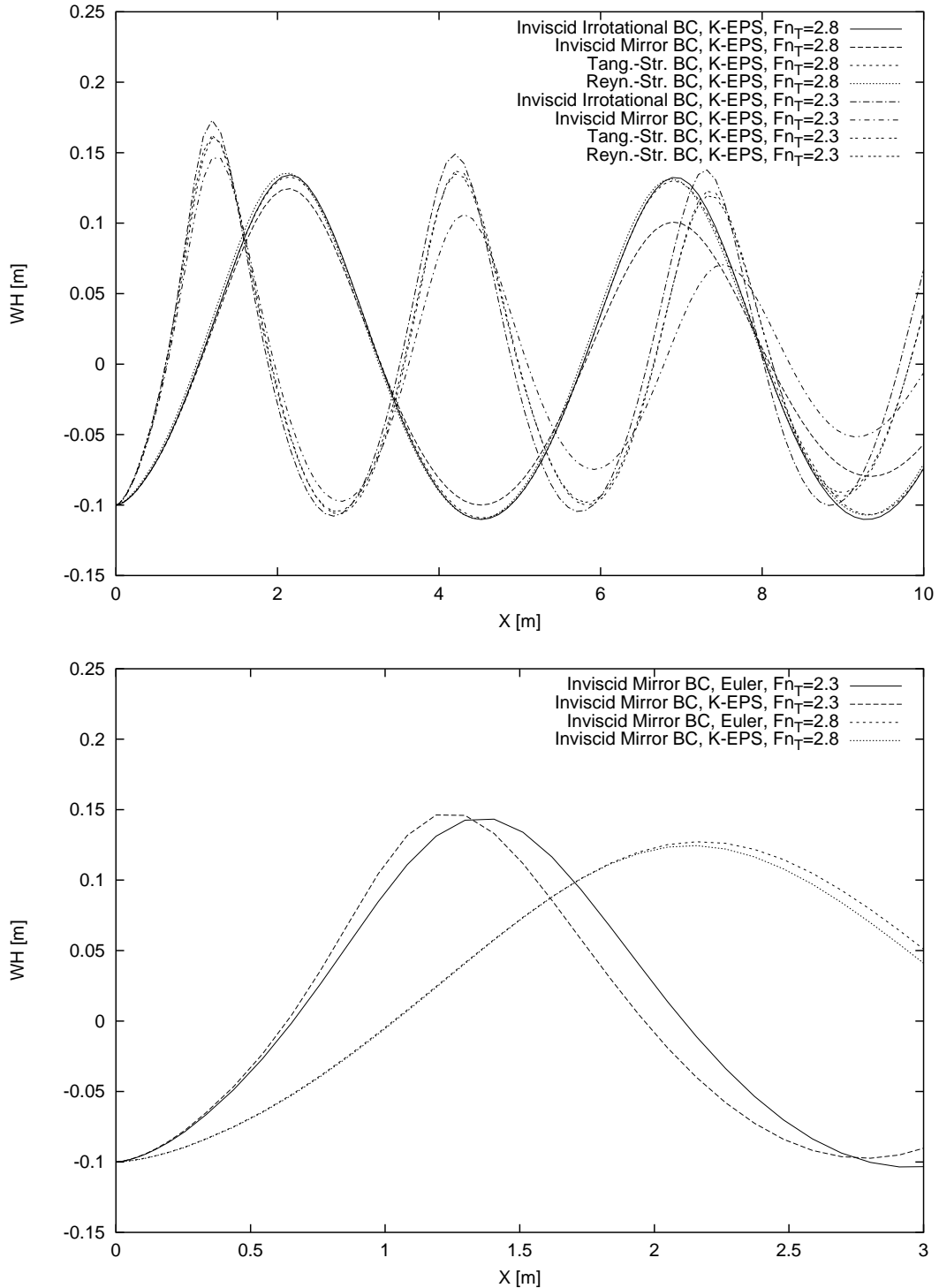
Figure 4.29: Computed transom-wave profiles of the model, *Ile*. Froude numbers, $Fn_T = 2.8$ and 2.3. Reynolds numbers, $Re_l = 3.732 \times 10^6$ and 3.066×10^6. Grid, FINE. **Top:** Solution of the RaNS equations with Chien's k-ϵ turbulence model and the inviscid and viscous free-surface boundary conditions. **Bottom:** Solution of the Euler and RaNS equations with Chien's k-ϵ turbulence model and the inviscid mirror free-surface boundary conditions.
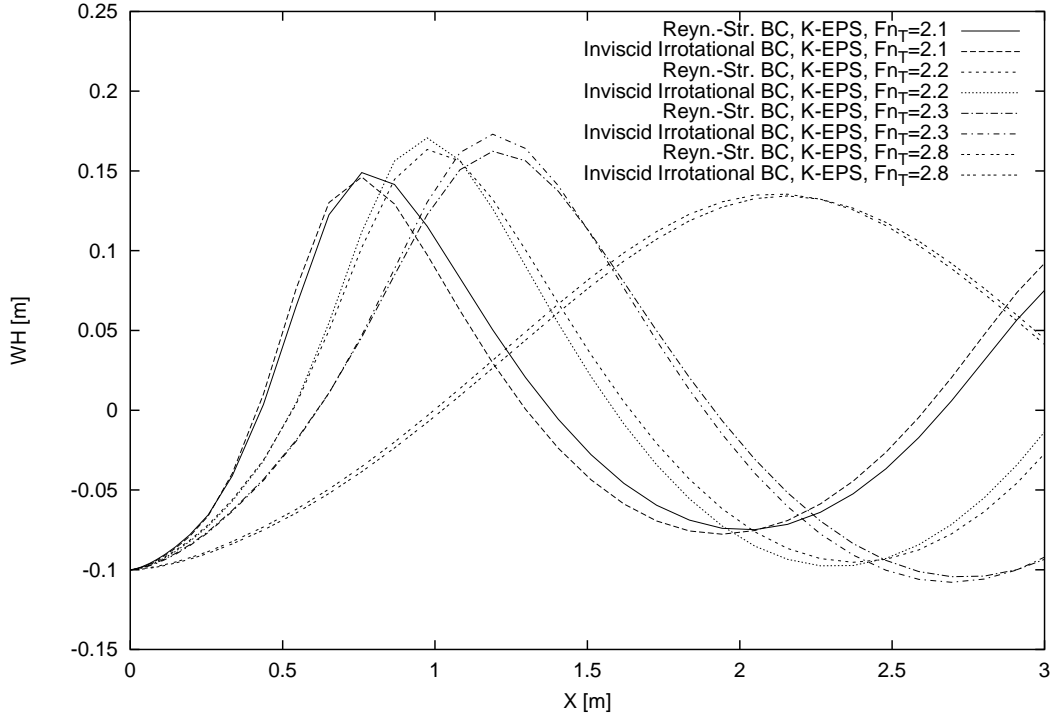
Figure 4.30: Computed wave profiles behind the transom of the model, *Ile*, for the Froude numbers, $Fn_T = 2.1$, $Fn_T = 2.2$, $Fn_T = 2.3$ and $Fn_T = 2.8$, and the respective Reynolds numbers, $Re_l = 2.8 \times 10^6$, $Re_l = 2.933 \times 10^6$, $Re_l = 3.066 \times 10^6$ and $Re_l = 3.732 \times 10^6$. The computations were carried out solving the RaNS equations using Chien's k-ϵ turbulence model and the inviscid irrotational and Reynolds-stress free-surface boundary conditions. The used grid was FINE.

4.4.2 Influence of the Free-Surface Boundary Conditions on the Flow Field

In Figs. 4.31 up to 4.36, the momentum, the momentum components in the x- and z-directions, the turbulent kinetic energy, the nondimensional turbulent viscosity and the nondimensional vorticity obtained from the computations with the inviscid irrotational and the Reynolds-stress free-surface boundary conditions are presented. The difference between the results with respect to the inviscid and viscous free-surface boundary conditions is rather small. Nevertheless, the turbulent kinetic energy is obviously stronger pronounced by the inviscid irrotational free-surface boundary conditions than by the Reynolds-stress ones. The height of the wave is greater, and its curvature

is stronger in the case of the inviscid irrotational free-surface boundary conditions . Therefore, the velocity gradients below the wave are also stronger, and the production of the turbulent kinetic energy is increased. In consequence, the increased turbulent kinetic energy causes also an increased turbulent viscosity (Fig. 4.35).

In Fig. 4.34, the amplification of the convected turbulent kinetic energy below the wave crest may be observed very clearly.
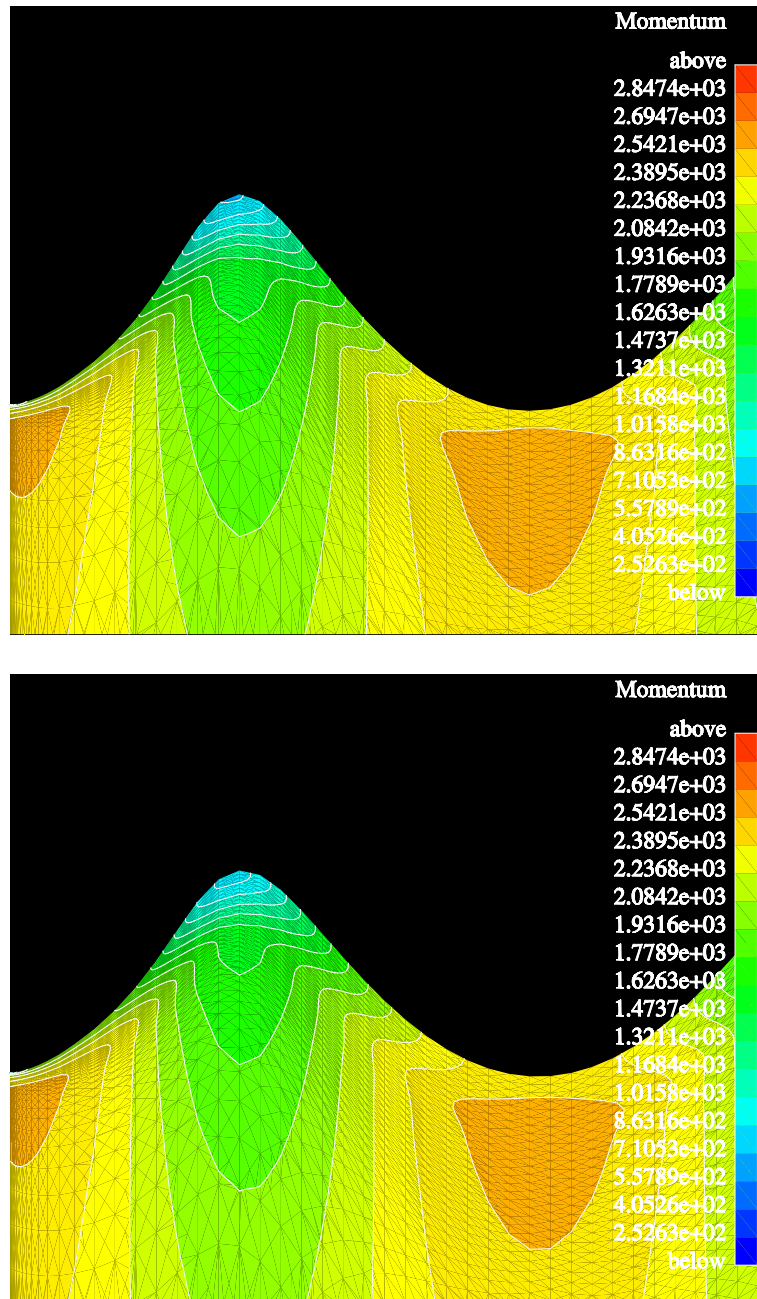
Figure 4.31: Computed momentum, $\rho|\vec{V}|$, behind the transom of the model, *Ile*. The computations were carried out solving the RaNS equations using Chien's k-ϵ turbulence model and the inviscid irrotational (**top**) and Reynolds-stress (**bottom**) free-surface boundary conditions. The used grid was FINE. $Fn_T = 2.3$. $Re_l = 3.066 \times 10^6$. The pictures were compressed in the horizontal direction.
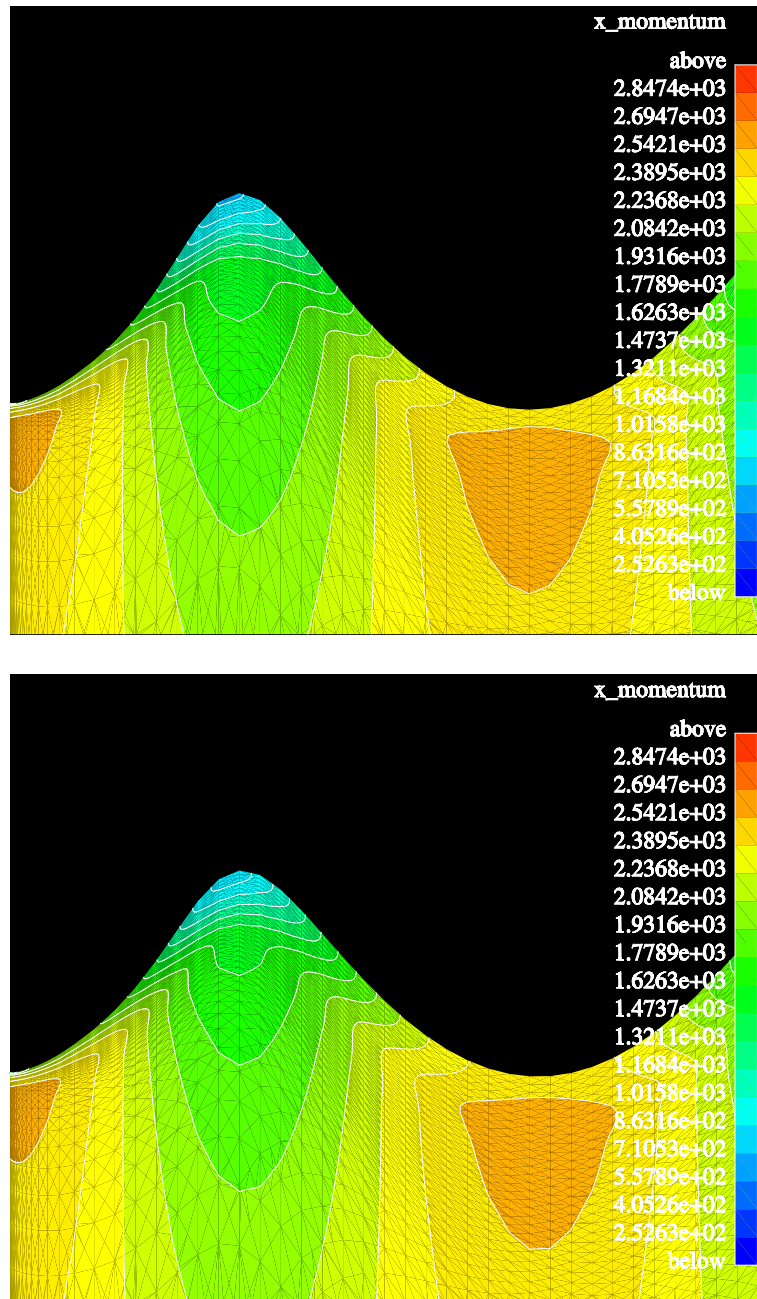
Figure 4.32: Computed component of the momentum in the x-direction, ρu, behind the transom of the model, *Ile*. The computations were carried out solving the RaNS equations using Chien's k-ϵ turbulence model and the inviscid irrotational (**top**) and Reynolds-stress (**bottom**) free-surface boundary conditions. The used grid was FINE. $Fn_T = 2.3$. $Re_l = 3.066 \times 10^6$. The pictures were compressed in the horizontal direction.

Figure 4.33: Computed component of the momentum in the z-direction, ρw, behind the transom of the model, *Ile*. The computations were carried out solving the RaNS equations using Chien's k-ϵ turbulence model and the inviscid irrotational (**top**) and Reynolds-stress (**bottom**) free-surface boundary conditions. The used grid was FINE. $Fn_T = 2.3$. $Re_l = 3.066 \times 10^6$. The pictures were compressed in the horizontal direction.
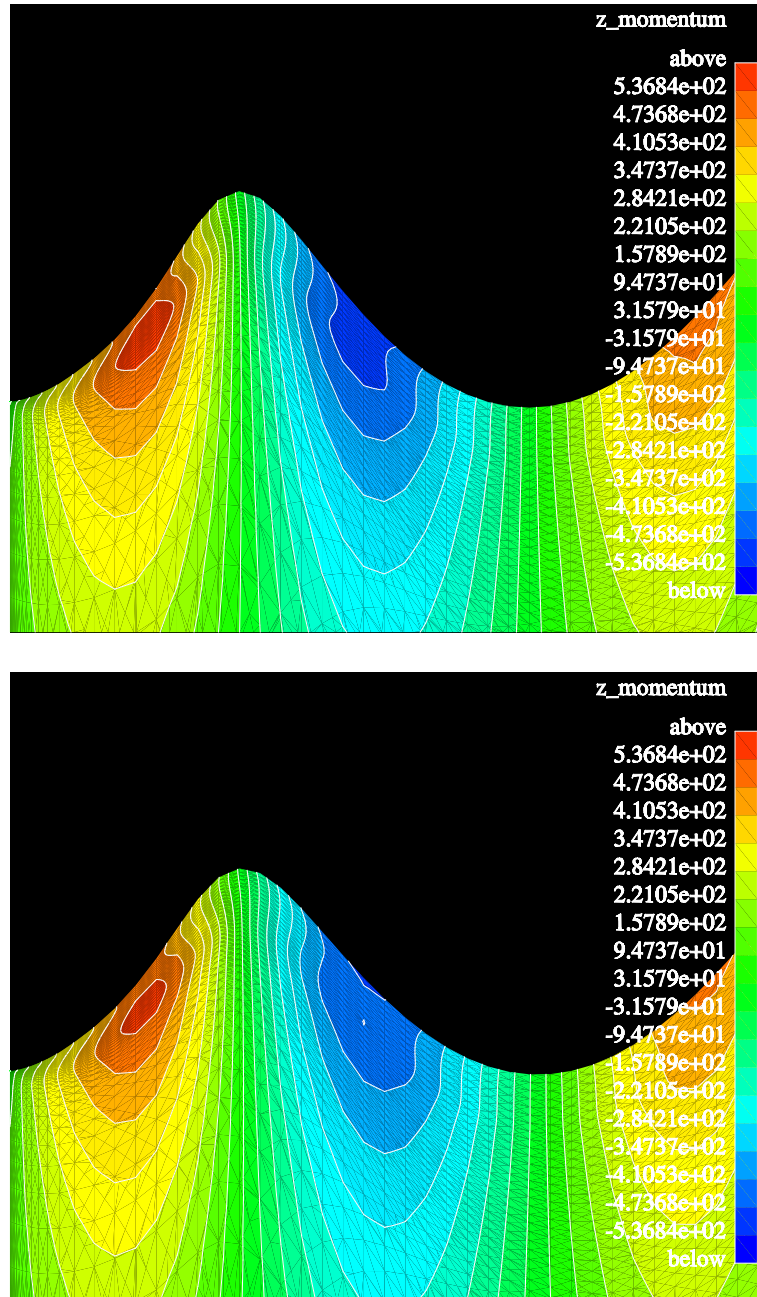
Figure 4.34: Computed turbulent kinetic energy, ρk, behind the transom of the model, *Ile*. The computations were carried out solving the RaNS equations using Chien's k-ϵ turbulence model and the inviscid irrotational (**top**) and Reynolds-stress (**bottom**) free-surface boundary conditions. The used grid was FINE. $Fn_T = 2.3$. $Re_l = 3.066 \times 10^6$. The pictures were compressed in the horizontal direction.
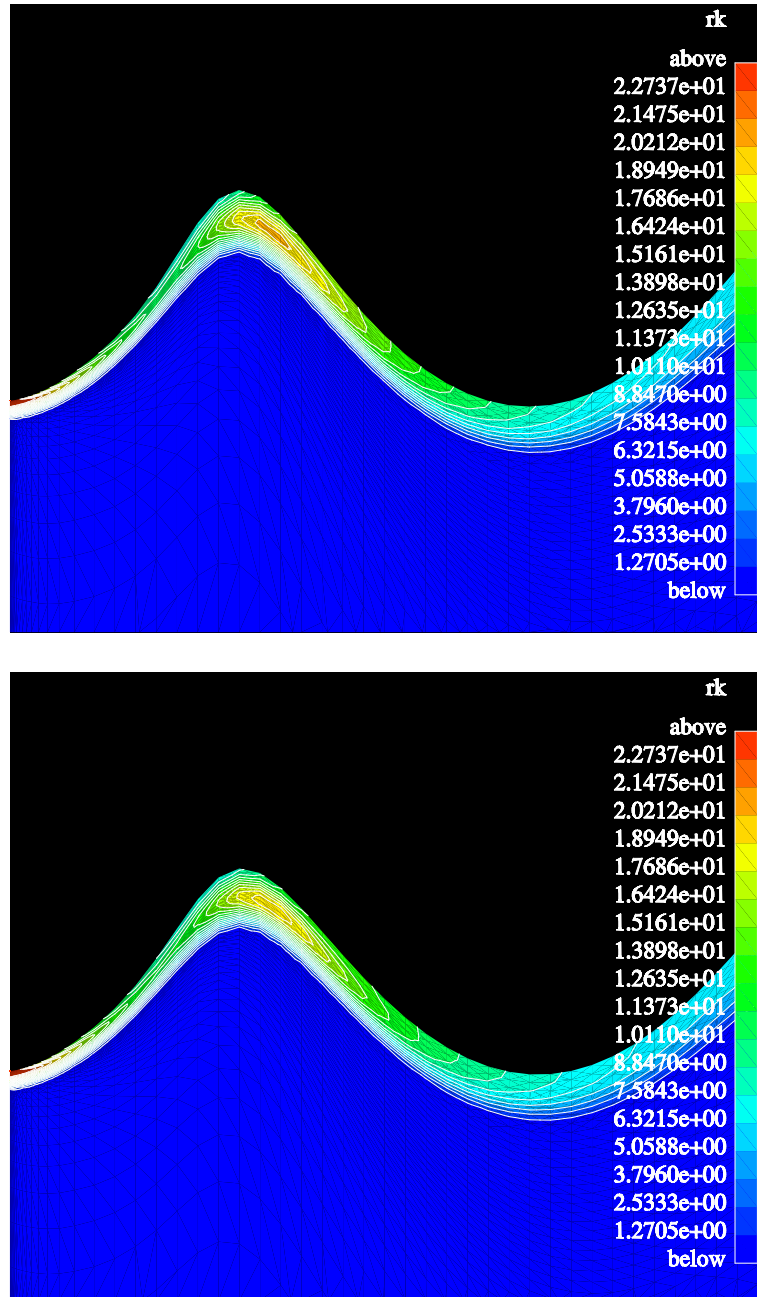
Figure 4.35: Computed nondimensional turbulent viscosity, μ_T/μ, behind the transom of the model, *Ile*. The computations were carried out solving the RaNS equations using Chien's k-ϵ turbulence model and the inviscid irrotational (**top**) and Reynolds-stress (**bottom**) free-surface boundary conditions. The used grid was FINE. $Fn_T = 2.3$. $Re_l = 3.066 \times 10^6$. The pictures were compressed in the horizontal direction.
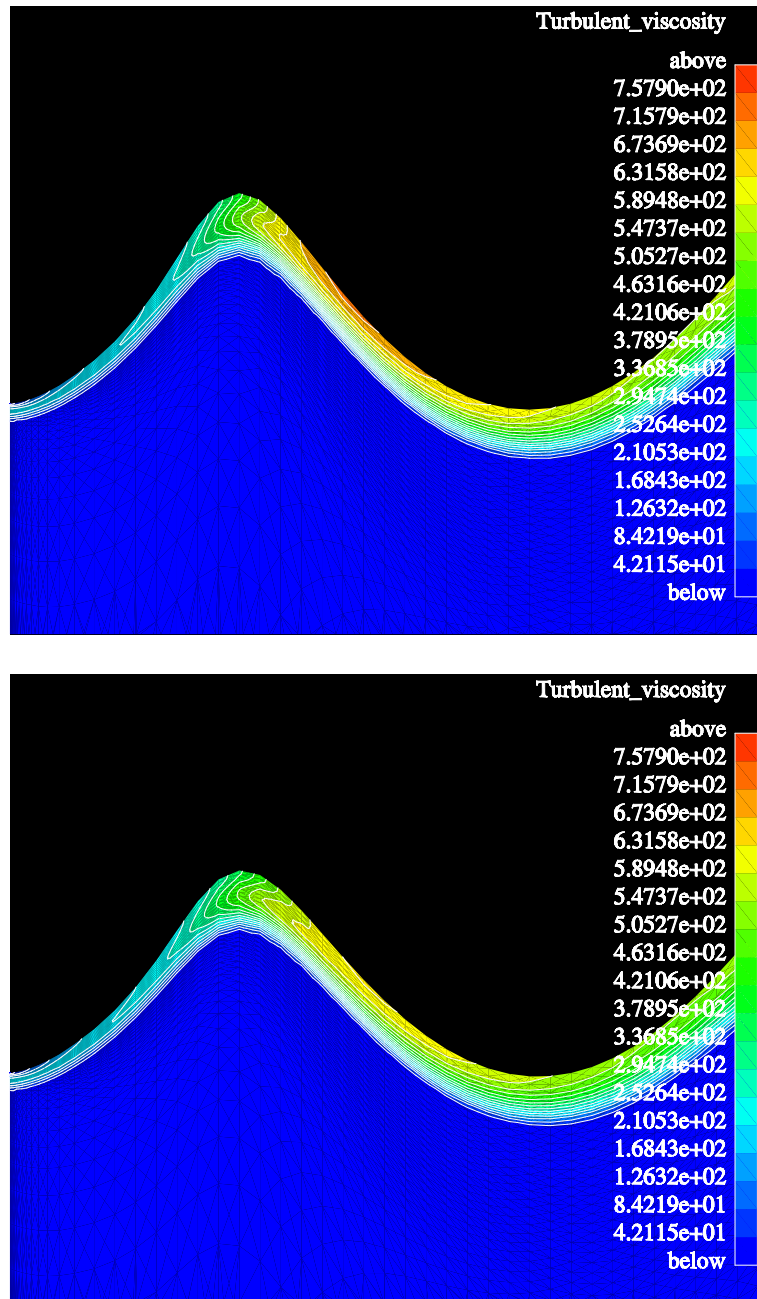
Figure 4.36: Computed nondimensional vorticity, γ^*, behind the transom of the model, *Ile*. The computations were carried out solving the RaNS equations using Chien's k-ϵ turbulence model and the inviscid irrotational (**top**) and Reynolds-stress (**bottom**) free-surface boundary conditions. The used grid was FINE. $Fn_T = 2.3$. $Re_l = 3.066 \times 10^6$. The pictures were compressed in the horizontal direction.
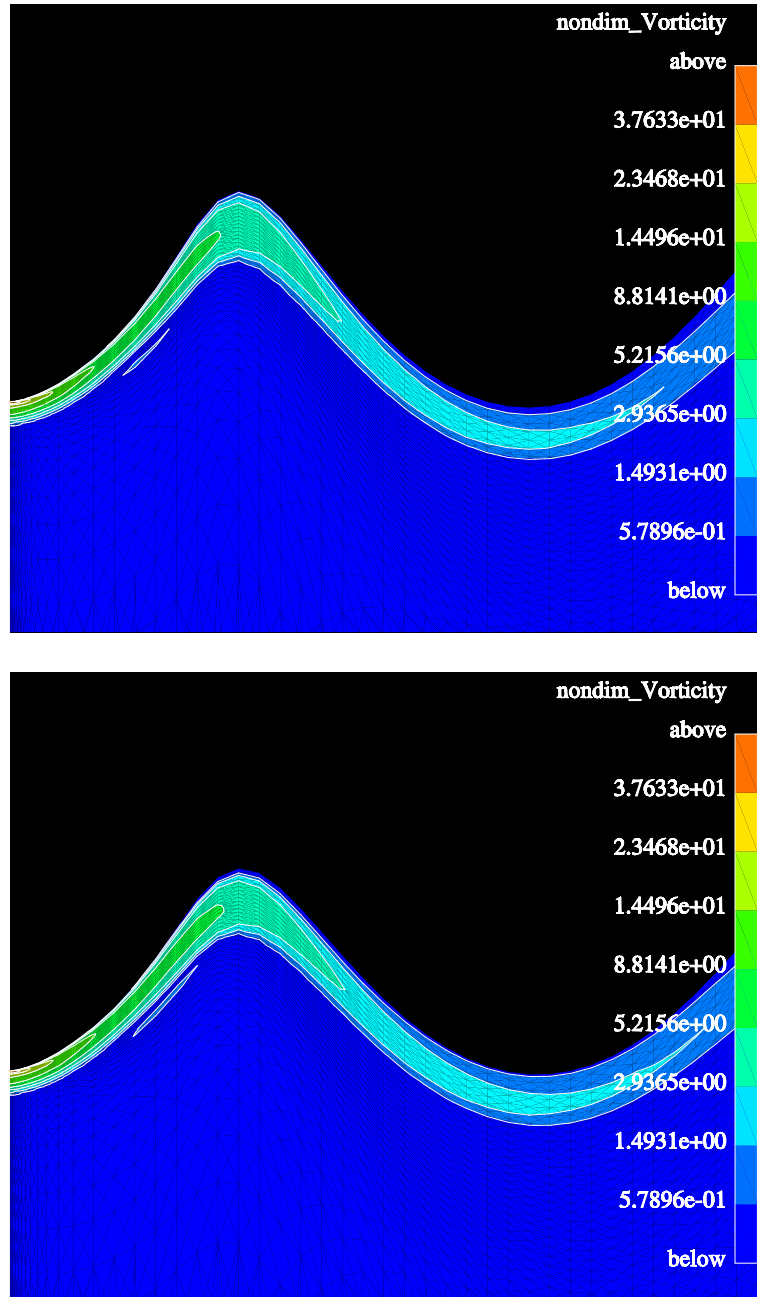
4.4.3   Resistance

In Table 9, the computed drag coefficients are presented for the Froude number, $Fn_T = 2.3$. The viscous free-surface boundary conditions give an about three percent higher value for the drag coefficient than the inviscid mirror free-surface boundary conditions. This result is similar to the one obtained for the Froude number, 2.8. Nevertheless, the inviscid irrotational free-surface boundary conditions give an about three percent higher value for the drag coefficient than the viscous free-surface boundary conditions. For the Froude number, 2.8, no difference was obtained. The difference between both inviscid free-surface boundary conditions is with six percent already not negligible.

Table 9: Drag coefficient, C_D, obtained from the computations for the grids, FINE. The computations were performed using Chien's k-ϵ turbulence model and the inviscid and viscous free-surface boundary conditions. $Fn_T = 2.3$.

Case	FINE
Euler, inviscid mirror BC, $C_D \times 10^3$	9.77
k-ϵ, inviscid mirror BC, $C_D \times 10^3$	14.3
k-ϵ, inviscid irrotational BC, $C_D \times 10^3$	15.09
k-ϵ, tang.-str. BC, $C_D \times 10^3$	14.66
k-ϵ, Reyn.-str. BC, $C_D \times 10^3$	14.63

4.4.4   Convergence

In Figs. 4.37 and 4.38, the convergence histories of the computations associated with the inviscid mirror and Reynolds-stress free-surface boundary conditions are presented. Considering the drag coefficient, C_D, and the L_2-norms of the turbulence quantities, no difference in the convergence duration can be observed. For the L_2-norms of the density, the x-momentum and the z-momentum, the inviscid mirror free-surface boundary conditions give a faster convergence than the Reynolds-stress free-surface boundary conditions. Using a similar reasoning as for the Froude number, 2.8, with respect to the convergence, it makes no difference whether the inviscid mirror or the viscous free-surface boundary conditions are used. This holds also for the inviscid irrotational free-surface boundary conditions.
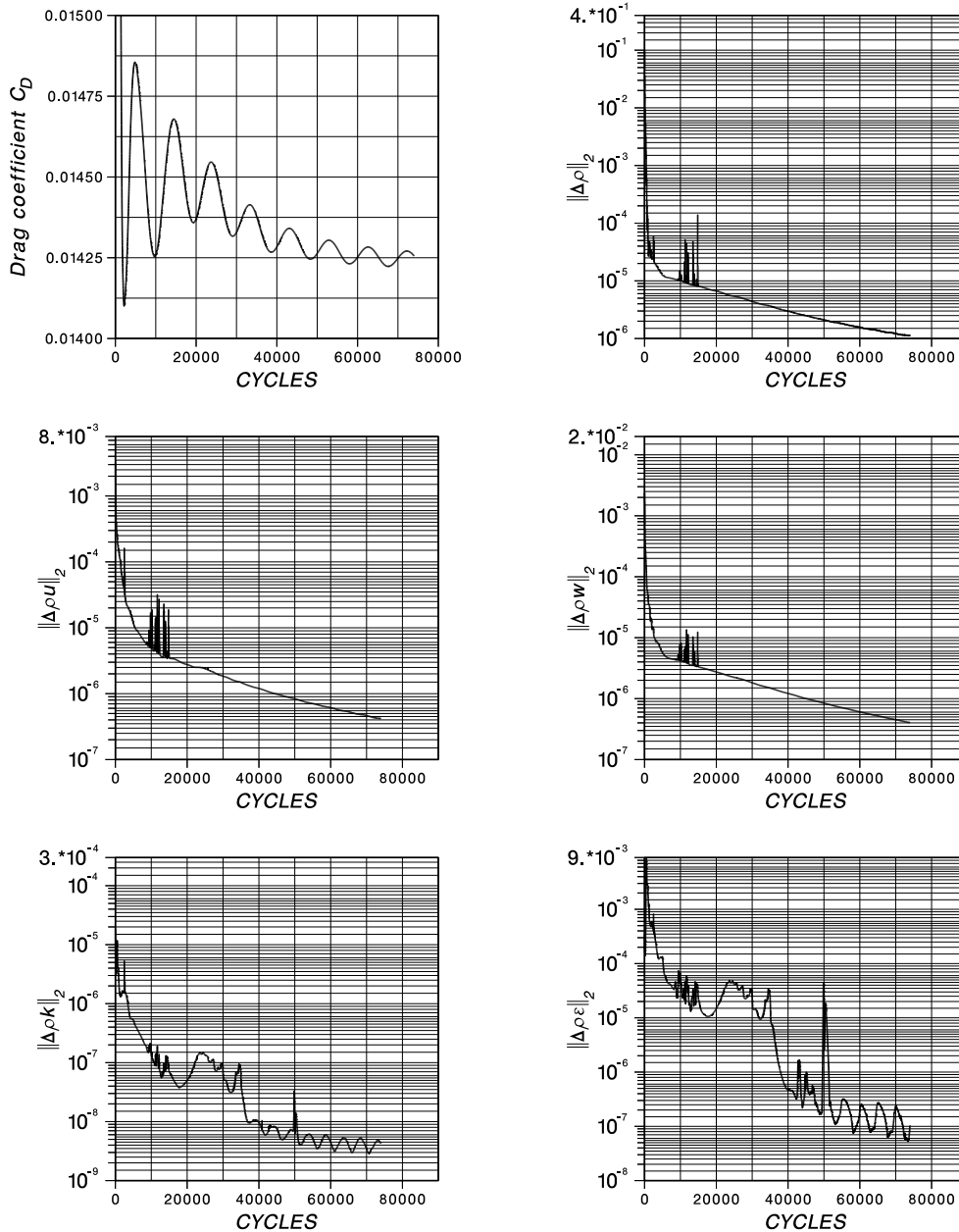
Figure 4.37: Convergence history for the model, *Ile*. The computation was performed solving the RaNS equations using Chien's k-ϵ turbulence model and the inviscid mirror free-surface boundary conditions. The used grid was FINE. C_D is the drag coefficient. The other quantities are the L_2-norms of the residuals of the density, ρ, the x-momentum, ρu, the z-momentum, ρw, the turbulent kinetic energy, k, and the dissipation of the turbulent kinetic energy, ϵ. $Fn_T = 2.3$.

Figure 4.38: Convergence history for the model, *Ile*. The computation was performed solving the RaNS equations using Chien's k-ϵ turbulence model and the Reynolds-stress free-surface boundary conditions. The used grid was FINE. C_D is the drag coefficient. The other quantities are the L_2-norms of the residuals of the density, ρ, the x-momentum, ρu, the z-momentum, ρw, the turbulent kinetic energy, k, and the dissipation of the turbulent kinetic energy, ϵ. $Fn_T = 2.3$.
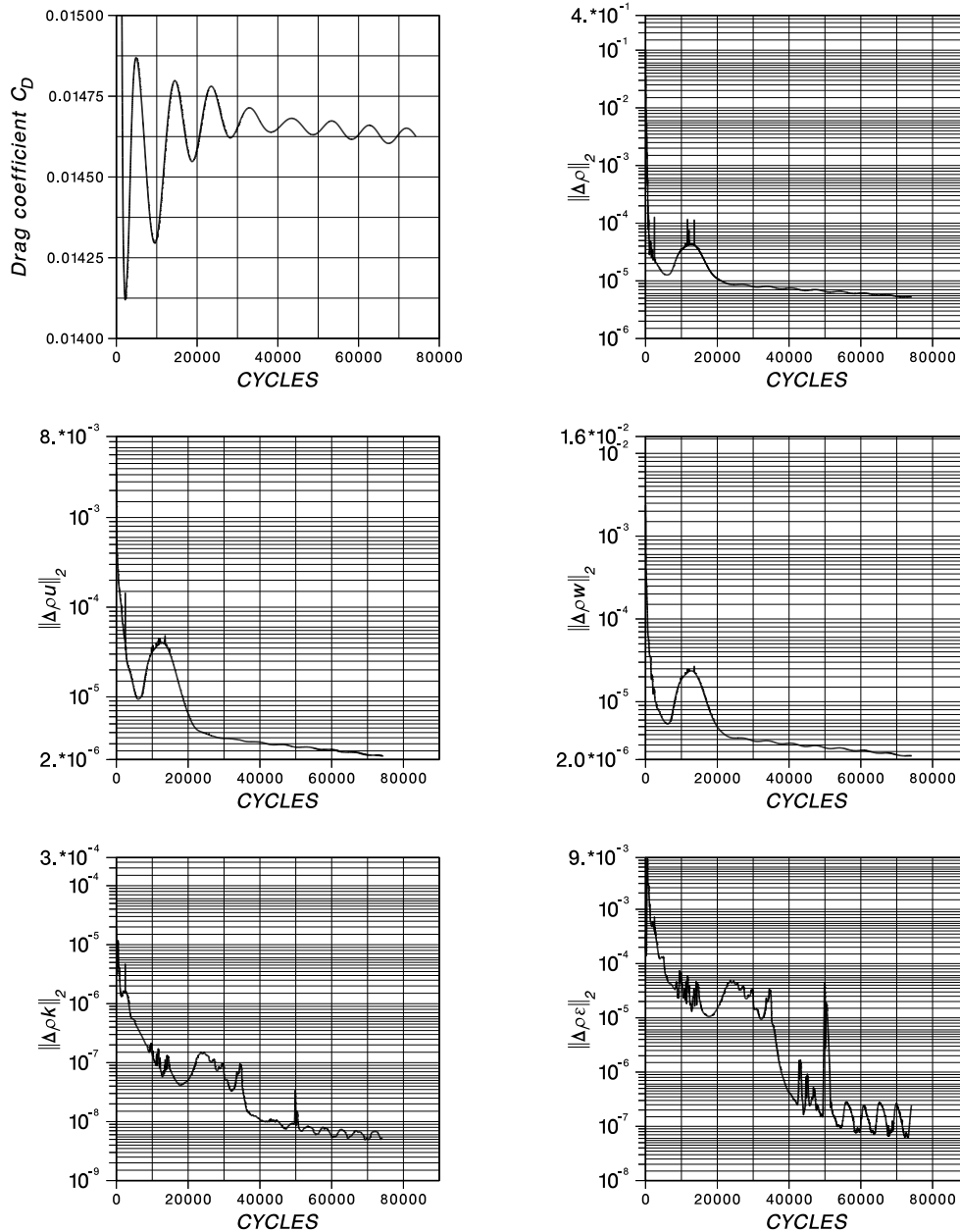
5 Discussion of the Results

The simulations in this work demonstrate the significant effect of the numerical realization of the free-surface boundary conditions on the computed transom waves. Depending on the numerical realization of the free-surface boundary conditions, the computed transom wave is either very little or significantly dampened. The main cause for the dampened solution is numerical damping. The applied free-surface boundary conditions cause a little modification of the flow field close to the free-surface resulting also in different wave profiles. Using the realization of the viscous and the inviscid irrotational free-surface boundary conditions, the numerical damping is less pronounced than in the case of the inviscid mirror free-surface boundary conditions. Therefore, a grid-independent solution may be obtained with less cells, and the computational time may be kept shorter. The inviscid irrotational and the inviscid mirror free-surface boundary conditions have the same physical meaning. Nevertheless, their numerical realizations are different, and the obtained wave profiles show remarkable differences. The strong damping associated with the inviscid mirror free-surface boundary conditions is mainly due to the assumption on the free surface, $\partial w/\partial z = 0$. This assumption should be avoided, and it is recommended to calculate the derivative, $\partial w/\partial z$, from the continuity equation. At the Froude number 2.8, the viscous and the inviscid irrotational free-surface boundary conditions give a negligible difference between the computed wave profiles and the flow fields, and the solution is physically correct. This holds also for the computations at the full-scale ship Reynolds number. Therefore, in this particular case, it makes no difference which of these boundary conditions is applied on the free surface, and the influence of the turbulent viscosity on the transom waves through the dynamic free-surface boundary condition regarding the normal stresses on the free surface can be neglected at model and full scale. Further, the application of the Boussinesq approximation to the evaluation of the Reynolds stresses in the dynamic free-surface boundary conditions has no influence on the evaluated waves. At the lower Froude numbers, where the steepness of the waves and the curvature become more pronounced and

the viscosity effects are increased, the Reynolds-stress free-surface boundary conditions give a strongerly dampend wave profile and a less pronounced turbulence within the transom wave compared with the results obtained with the inviscid irrotational free-surface boundary conditions. Therefore, at the lower Froude numbers, it makes physically a difference which free-surface boundary conditions are applied, and the application of the Reynolds-stress free-surface boundary conditions is recommended.

The computed transom waves amplify the turbulence convected from the boundary layer into the wave system below the wave crest. The turbulent kinetic energy and the respective turbulent viscosity are significantly increased with increasing wave steepness. Therefore, the appearance of waves along the hull of a ship will be associated with an increased turbulent viscosity and skin friction below the wave crests close to the free surface.

For the drag coefficient, a slight difference is obtained by the inviscid and viscous free-surface boundary conditions. For the Froude numbers, 2.3 and lower, this difference cannot be neglected anymore, and the application of the Reynolds-stress free-surface boundary conditions is recommended.

Regarding the convergence, the investigated free-surface boundary conditions give no significant difference.

For the Froude number, 2.8, the boundary layer of the model has a negligible influence on the transom waves at model and full scale. For the Froude number, 2.3, a clear influence is observed. Therefore, for sufficient high model-scale ship Reynolds numbers and a transom wave of moderate steepness, the boundary layer will have no influence on the transom waves at model and full scale.

The computations at the full-scale ship Reynolds number show the remarkable effect of the free-stream turbulence quantities on the boundary layer of the hull when using Chien's low-Reynolds number k-ϵ turbulence model. Keeping the free-stream turbulence level and the nondimensional free-stream turbulent viscosity constant will cause a very high free-stream dissipation of the turbulent kinetic energy resulting in a prevented development of the boundary layer and an underestimated skin friction resistance coefficient. A correct development of the boundary layer is obtained by keeping the free-stream dissipation of the turbulent kinetic energy constant, similar to a material property, and either the nondimensional turbulent viscosity or the free-stream turbulence level variable. For ship flows where the fluid is basically at rest, it seems to be advisable to use a reduced free-stream turbulence level and not an increased nondimensional free-stream turbulent viscosity. The turbulent viscosity will alter the appearing Reynolds number, and partly laminar regions of the hull, e.g. at appendages, will become

turbulent.

The application of multigridding at the full-scale Reynolds number improves the convergence fairly. In a three-dimensional case where more grid levels may be used, the improvement may be even increased. Therefore, the application of multigridding at full-scale ship Reynolds numbers is justified.

At full scale, the computations give a significantly increased nondimensional vorticity at the vicinity of the transom compared with the one at model scale. The dimensional value of the turbulent kinetic energy is also significantly increased at the free surface. At full scale, in association with a lower surface tension than at model scale, this might result in the appearance of ripples at the free surface and a breaking free surface, which would not necessarily appear at model scale.

The computed pressure and mean skin friction coefficients are scaled to full scale giving a total resistance coefficient, which is in in excellent agreement with the one of the modified ITTC-78 method. The ITTC-57 extrapolation method gives a little overestimated total resistance coefficient. The form factor with respect to the mean skin friction line of a flat plate remains constant. With respect to the ITTC-57 model-ship correlation line it is not constant as the ITTC-57 model-ship correlation line deviates from the mean skin friction line of a flat plate at model-scale ship Reynolds numbers. Therefore, for similar computational cases, it may be assumed that the pressure and mean skin friction resistance coefficients will be correctly scaled from model to full scale by the respective computations.

5.1   An Improved Extrapolation Method

It has been shown that turbulent ship-flow computations including the evaluation of the free-surface are possible up to full-scale ship Reynolds numbers whereby the accuracy of the results may be regarded as at least satisfactory. Using the obtained skills, a new extrapolation method for the evaluation of the total resistance of a ship may be proposed.

In the future, the final-power estimation of a full-scale ship may be carried out using the traditional extrapolation methods, reference ships with empirical correlation coefficients, computational methods with empirical correlation coefficients, computational methods with model testing and computational methods of very high accuracy. Except the last two ones, all other methods are based on empirical coefficients which are not known for novel ships. Therefore, the final power prediction for the new vessel may be significantly erroneous. Due to the approximative treatment of the turbulence

and the grid influence on the results, a highly accurate estimation of the final power seems to be not generally possible using only computational methods.

The proposed extrapolation method is based on the idea to use the model-test results for calibration purposes. Further, it is assumed that the scaling of the total resistance may be estimated fairly accurate using computational methods. The new method makes no use of empirical correlation coefficients anymore. It combines model testing with ship-flow computations at model-scale and full-scale ship Reynolds numbers, and it is outlined in the following.

At the model-scale ship Reynolds number, the total resistance coefficient, C_{TM}, is obtained from the model test. Respective computations of the ship are carried out at model-scale and full-scale ship Reynolds numbers giving the total resistance coefficients, C_{TMC} and C_{TSC}, respectively. C_{TMC} is the computed total resistance coefficient at model scale, and C_{TSC} is the one at full scale. It is assumed that the scaling of the measured total resistance coefficient obeys the following relation:

$$\frac{C_{TM}}{C_{TS}} = \frac{C_{TMC}}{C_{TSC}} \; , \tag{5.1}$$

where C_{TS} is total resistance coefficient of the ship. Using the measured and computed results, the total resistance coefficient of the ship is obtained from

$$C_{TS} = C_{TM}\frac{C_{TSC}}{C_{TMC}} \; . \tag{5.2}$$

No engineering line and no empirical correlation coefficients are needed anymore. The hull form influence on the pressure and skin friction resistance coefficients is taken into account. Basically, the method is applicable also for rough surfaces provided a suitable turbulence model is available. Having measured the thrust at model scale, the same idea may be applied to the estimation of the thrust at full scale by computations of the hull-propeller interaction at model- and full-scale ship Reynolds numbers.

6 Conclusions

Considering the results of this work, the conclusions may be summarized as presented in the following.

The numerical realization of the free-surface boundary conditions has a significant effect on the computed transom waves. Depending on the numerical realization of the free-surface boundary conditions, the computed transom wave is either very little or significantly dampened. The damped solution is caused by numerical damping and the modification of the flow field close to the free surface. The assumption on the free surface, $\partial w/\partial z = 0$, causes a dampened wave profile, and it should be avoided. Using the viscous and the inviscid irrotational free-surface boundary conditions, a solution independed of the grid may be obtained with a rather low resolution of the grid resulting in shorter computational times.

At the Froude number 2.8, it makes no difference whether the viscous or the inviscid irrotational free-surface boundary conditions are applied to the evaluation of the transom waves. This holds also for the computations at the full-scale ship Reynolds number. The influence of the turbulent viscosity on the transom waves through the dynamic free-surface boundary condition with respect to the normal stresses can be neglected at model and full scale. Further, the application of the Boussinesq approximation has no influence on the evaluated waves through the dynamic free-surface boundary condition with respect to the normal stresses.

At the lower Froude numbers, where the steepness of the waves and the curvature become more pronounced and the viscosity effects are increased, it makes physically a difference which free-surface boundary conditions are applied, and the application of the Reynolds-stress free-surface boundary conditions is recommended.

The appearance of waves will cause an amplification of the turbulent kinetic energy and the respective turbulent viscosity below the wave crest, and, therefore, the skin friction will be increased in this area.

For the drag coefficient, a slight difference is obtained by the inviscid and viscous free-surface boundary conditions. For the Froude numbers, 2.3 and

lower, it cannot be neglected anymore, and the application of the Reynolds-stress free-surface boundary conditions is recommended.

Regarding the convergence, it makes no difference which one of the investigated free-surface boundary conditions is used.

For sufficient high Reynolds numbers and a transom wave of moderate steepness, the boundary layer will have no influence on the transom waves at model and full scale. The effect of the boundary layer on the transom waves increases with decreasing Froude and Reynolds numbers.

When using Chien's low-Reynolds number k-ϵ turbulence model at model and full scale, the free-stream dissipation of the turbulent kinetic energy has to be kept constant, similar to a material property, and either the nondimensional free-stream turbulent viscosity or the free-stream turbulence level has to be a variable.

The application of multigridding at full-scale ship Reynolds numbers will improve the convergence.

At full scale, the nondimensional vorticity at the vicinity of the transom will be significantly increased compared with the one at model scale. The dimensional value of the turbulent kinetic energy will be also significantly increased at the free surface. At full scale in association with a lower surface tension than at model scale, this might result in the appearance of ripples at the free surface and a breaking free surface, which would not necessarily appear at model scale.

For similar computational cases as the ones presented in this investigation, it may be assumed that the pressure, the mean skin friction and the total resistance coefficients will be correctly scaled from model to full scale by the respective computations.

Free-surface computations of turbulent ship flows are possible at full-scale ship Reynolds numbers using the moving-grid technique and no wall functions.

In the future, based on the results of this work, further research may be conducted with respect to the following items:

- Investigation of the accuarcy of the proposed extrapolation method.

- Effect of a second-order extrapolation of the velocities to the free surface on the waves.

- Departure from the flat-surface approximation and use of the exact free-surface boundary conditions.

- Extension of the method to three-dimensional cases.

- Investigation of the scaling of high-curvature free surfaces where viscosity effects are evident.

Dealing with the inviscid irrotational and the viscous free-surface boundary conditions presented in this work, little damping of the waves may appear. Therefore, the creation of artificial damping zones might be necessary in order to avoid the reflection of the waves from the boundaries of the computational domain.

Bibliography

AHO, H. AND SCHWEIGHOFER, J. 1995. Laboratory Exercise - Model Tests, Ship Laboratory, Helsinki University of Technology, in Finnish.

ALESSANDRINI, B. AND DELHOMMEAU, G. 1994. Simulation of Three-Dimensional Unsteady Viscous Free Surface Flow around a Ship Model, *International Journal for Numerical Methods in Fluids*, Volume 19, pp. 321-342.

ALESSANDRINI, B. AND DELHOMMEAU, G. 1997. A Multigrid Velocity-Pressure-Free Surface Elevation Fully Coupled Solver for Calculation of Turbulent Incompressible Flow around a Hull, *21st Symposium on Naval Hydrodynamics*, pp. 328-329.

ANDERSON, D.A., TANNEHILL, J.C., PLETCHER, R.H. 1984. Computational Fluid Dynamics and Heat Transfer, Hemisphere Publishing Corporation, McGraw-Hill Book Company.

BALDWIN, B.S. AND LOMAX, H. 1978. Thin-Layer Approximation and Algebraic Model for Separated Turbulent Flows, *AIAA Paper*, 78-257, Huntsville, AL.

BRANDT, T. 2000. Inclusion of a Two-Equation Turbulence Model in the Navier-Stokes solver FINFLO-SHIP, Master's Thesis, Department of Engineering Physics and Mathematics, Helsinki University of Technology.

BRUNS, J., DENGEL, P. AND FERNHOLZ, H.H. 1992. Mean Flow and Turbulence Measurements in an Incompressible Two-Dimensional Turbulent Boundary Layer, Part 1: data. Institutsbericht

Nr. 02/92, Hermann-Föttinger-Institut für Thermo- und Fluiddynamik, Technische Universität Berlin.

CHAO, K.Y. 2001. Numerical Propulsion Tests, *Ship Technology Research - Schiffstechnik*, No. 48, pp. 51-55.

CHEN, Y.J., KOUH, J.S. AND CHAU, S.W. 2001. Computation of Free-Surface Ship Flow at Full-Scale and Model-Scale Reynolds Number Using VOF Method, *Fourth Numerical Towing Tank Symposium*, Hamburg, Germany.

CHEN, Y.J. 2001. Private conversation.

CHIEN, K. 1982. Predictions of Channel and Boundary-Layer Flows with a Low-Reynolds-Number Turbulence Model, *AIAA Journal*, Vol. 20, No. 1, pp. 33-38.

CHOI, J.E. AND STERN, F. 1993. Solid-Fluid Juncture Boundary Layer and Wake with Waves, *Proceedings of the 6th International Conference on Numerical Ship Hydrodynamics*, Iowa City, Iowa.

COWLES, G. AND MARTINELLI, L. 1999. A Viscous Multiblock Flow Solver for Free-Surface Calculations on Complex Geometries, *22nd Symposium on Naval Hydrodynamics*.

DABIRI, D. AND GHARIB, M. 1997. Generation Mechanisms and Sources of Vorticity Within a Spilling Breaking Wave, *21st Symposium on Naval Hydrodynamics*, pp. 520-533.

DOLPHIN, G.W. 1997. Evaluation of Computational Fluid Dynamics for a Flat Plate and Axisymmetric Body from Model- to Full-Scale Reynolds Numbers, Master's Thesis, University of Iowa, Iowa City, IA.

DONG, C.M. AND HUANG, C.J. 1999. Vortex Generation in Water Waves Propagating Over a Submerged Rectangular Dike, *Proceedings of the Ninth International Offshore and Polar Engineering Conference*, Brest, France, pp. 388-395.

ECA, L. AND HOEKSTRA, M. 1997. Numerical Calculations of

Ship Stern Flows at Full-Scale Reynolds Numbers, *Twentyfirst Symposium on Naval Hydrodynamics*, National Research Council, pp. 377-391.

ECA, L. AND HOEKSTRA, M. 2000. Numerical Prediction of Scale Effects in Ship Stern Flows with Eddy-Viscosity Turbulence Models, *Twentythird Symposium on Naval Hydrodynamics*, National Research Council, pp. 553-568.

FAGERHOLM, J. AND HAATAJA, J. 1999. Client's Guide, CSC - Center for Scientific Computing, Helsinki, Finland, in Finnish.

FARMER, J.R. 1993. A Finite Volume Multigrid Solution to the Three Dimensional Nonlinear Ship Wave Problem, Ph.D.-Thesis, Department of Mechanical and Aerospace Engineering, Princeton University.

FERNHOLZ, H.H., KRAUSE, E., NOCKEMANN, M. AND SCHOBER, M. 1995. Comparative Measurements in the Canonical Boundary Layer at $Re_{\delta 2} \leq 6 \times 10^4$ on the Wall of DNW, Phys. Fluids, A7, pp. 1275-1281.

FERNHOLZ, H.H. AND FINLEY, P.J. 1996. The Incompressible Zero-Pressure-Gradient Turbulent Boundary Layer: an Assessment of the Data, Progress in Aerospace Sciences, Volume 32, No. 4, pp. 245-311.

FERZIGER, J.H. AND PERIĆ, M. 1999. Computational Methods for Fluid Dynamics, Second Edition, Springer-Verlag, Berlin, Heidelberg.

FUNENO, I. AND YAMANO, T. 2001. On Free Surface Flows behind a Two-Dimensional Transom Stern, *Journal of the Kansai Society of Naval Architects of Japan*, No. 235, pp. 23-30.

GENTAZ, L., MAURY, C., ALESSANDRINI, B. AND DELHOMMEAU, G. 2000. Numerical Simulations of a Two-Dimensional Wave Tank in Viscous Fluid, *International Journal of Offshore and Polar Engineering*, Volume 10, No. 1, pp. 1-9.

HELLSTEN, A. 1996. Implementation of a One-Equation Turbu-

lence Model into the FINFLO FLOW SOLVER, Report B-49, Series B, Laboratory of Aerodynamics, Helsinki University of Technology.

HINATSU, M. 1992. Numerical Simulation of Unsteady Viscous Nonlinear Waves Using Moving Grid System Fitted on a Free Surface, *Journal of the Kansai Society of Naval Architects of Japan*, No. 217, pp. 1-11.

HOFFRÉN, J. AND SIIKONEN, T. 1992. FINF2A: A Multi-Block Navier-Stokes Solver for Two-Dimensional and Axisymmetric Flows, Report B-38, Series B, Laboratory of Aerodynamics, Helsinki University of Technology.

ISHIKAWA, S. 1994. Application of CFD to the Estimation of Ship's Viscous Resistance - A Series of Full Hull Forms, Transactions of the West-Japan Society of Naval Architects, No. 87.

ITTC. 1999. ITTC - Quality Manual, *22nd International Towing Tank Conference*.

JAMESON, A. AND YOON, S. 1986. Multigrid Solution of the Euler Equations Using Implicit Schemes, *AIAA Journal*, 24, No. 11.

JÄRVINEN, E. 2000. Fluid Dynamics Technology Program 1995 - 1999, Final Report, TEKES, Helsinki, Finland, in Finnish.

JEONG, U.-C. AND DOI, Y. 1995. Numerical Study of Vortical Flows beneath the Free Surface around Struts, *Journal of the Society of Naval Architects of Japan*, Volume 178, pp. 23-31.

JU, S. AND PATEL, V. 1991. Stern Flows at Full-Scale Reynolds Numbers, *Journal of Ship Research*, Volume 35, No. 2, pp. 101-113.

JU, S. AND PATEL, V. 1994. A Numerical Approach for Predicting the Total Resistance and Nominal Wakes of Full-Scale Tankers, *Nineteenth Symposium on Naval Hydrodynamics*, National Research Council, pp. 371-387.

KAURINKOSKI, P. AND HELLSTEN, A. 1998. FINFLO: the Parallel Multi-Block Flow Solver, Report A-17, Laboratory of Aerody-

namics, Helsinki University of Technology.

KUK-JIN, K. 1996. Numerical Simulations of Nonlinear Waves Generated by Submerged Bodies, Post Doctoral Research Report CHA/NAV/R-96/0043, Department of Naval Architecture and Ocean Engineering, Chalmers University of Technology.

LARSSON, L., STERN, F. AND BERTRAM, V. 2000. Gothenburg 2000 - A Workshop on Numerical Ship Hydrodynamics, Department of Naval Architecture and Ocean Engineering, Chalmers University of Technology, Sweden.

LEHTIMÄKI, R. 2000. On Structured Grid Generation, Ph.D. Thesis, Report A-19, Laboratory of Aerodynamics, Helsinki University of Technology.

LI, T. 2000. Numerical Simulation of Viscous Steady Flow with Free Surface around Two Types of Modern Realistic Hull Forms: the Hamburg Test Case and Tanker, Report M-247, Ship Laboratory, Helsinki University of Technology.

LI, T. 2002. Ship Wavemaking in the Context of a RaNS-Solver FINFLO-SHIP, Report M-270, Ship Laboratory, Helsinki University of Technology.

LILEK, Z. 1995. A Numerical Method for Three-Dimensional Viscous Flows with Free Surfaces, Report 553, Institut für Schiffbau der Universität Hamburg, in German.

LILEK, Z. 1996. A Finite-Volume Method for the Computation of Incompressible and Compressible Flows in Complex Geometries with Moving Boundaries and Free Surfaces, Dissertation, Report 563, Institut für Schiffbau der Universität Hamburg, in German.

LIU, H. AND KODAMA, Y. 1993. Computation of Waves Generated by a Ship Using an NS Solver with Global Conservation, *Journal of the Society of Naval Architects of Japan*, Volume 173, pp. 1-8.

LOMBARD, C., BARDINA, J., VENKATAPATHY, E. AND OLIGER, J. 1983. Multi-Dimensional Formulation of CSCM - an

Upwind Flux Difference Eigenvector Split Method for the Compressible Navier-Stokes Equations, *6th AIAA Computational Fluid Dynamics Conference, AIAA Paper 83-1895-CP*, pp. 649-664.

LONGUET-HIGGINS, M.S. 1997. Progress Toward Understanding How Waves Break, *21st Symposium on Naval Hydrodynamics*, pp. 7-28.

LUNDGREN, T. AND KOUMOUTSAKOS, P. 1999. On the Generation of Vorticity at a Free Surface, *Journal of Fluid Mechanics*, Volume 382, pp. 351-366.

MENTER, F.R. 1993. Zonal Two-Equation k-ω Turbulence Models for Aerodynamic Flows, *24th AIAA Computational Fluid Dynamics Conference, (Orlando, Florida), AIAA Paper 93-2906-CP*.

MIKKOLA, T. 1999. Testing of Two FINFLO-Based Free-Surface Codes Using Eulerian Flow over a Gaussian Ground Elevation, Report D-56, Ship Laboratory, Helsinki University of Technology.

MIKKOLA, T. 2000. Implementation of an Implicit Scheme into a Free Surface RaNS Solver in order to improve the Convergence, Report M-257, Ship Laboratory, Helsinki University of Technology.

NIITTYMÄKI, J. 2001. Effects of the Stern Form on Hydrodynamic Properties of a Fast ROPAX-Vessel, Master's Thesis, Ship Laboratory, Helsinki University of Technology, in Finnish.

NUMECA INTERNATIONAL. 1999. Igg - User Manual, Version 3.7, Brussels, Belgium.

OHKUSU, M. 1996. Advances in Marine Hydrodynamics, Computational Mechanics Publications, Southampton, Boston, pp. 59.

PETRIE, H.L., FONTAINE, A.A., SOMMER, S.T. AND BRUNGART, T.A. 1990. Large Flat Plate Turbulent Boundary Layer Evaluation, TM-89-207, Pennsylvania State University Applied Research Laboratory.

RAHMAN, M., RAUTAHEIMO, P. AND SIIKONEN, T. 1997.

Numerical Study of Turbulent Heat Transfer from Confined Impinging Jets Using a Pseudo-Compressibility Method, Report 99, Laboratory of Applied Thermodynamics, Helsinki University of Technology.

RAHMAN, M. 1999. An Improved Pressure Correction Method on a Collocated Grid, Report 124, Laboratory of Applied Thermodynamics, Helsinki University of Technology.

RAHMAN, M. 2000. Solution Methods and Turbulence Modeling for Heat Transfer Problems, Ph.D. Thesis, Department of Mechanical Engineering, Helsinki University of Technology.

ROYAL AERONAUTICAL SOCIETY. 1968. The Compressible Two-Dimensional Turbulent Boundary Layer, Both with and without Heat Transfer, on a Smooth Flat Plate, with Application to Wedges, Cylinders and Cones, Engineering Sciences Data item No. 68020 with amendments A to C March 1988, Engineering Sciences Data Unit, London.

SAISTO, I. 1995. Computations of Waves Created by a Ship's Stern Using a Two-Dimensional Boundary-Element Method, Report M-193, Ship Laboratory, Helsinki University of Technology, in Finnish.

SAISTO, I. AND SUNDELL, T. 1996. Computation of the Viscous Flow Field around the HSVA Tankers, Report M-206, Ship Laboratory, Helsinki University of Technology.

SAISTO, I. 2000. Computation of Two-Dimensional Stern Wave Using the Boundary-Element Method, Licentiate Thesis, Department of Mechanical Engineering, Helsinki University of Technology.

SCHLICHTING, H. 1979. Boundary Layer Theory, 7th edition, McGraw-Hill, New York.

SCHMITT, H. 1997. Advances in Fluid Dynamics - Flows at Large Reynolds Numbers, Computational Mechanics Publications, pp. 251-290.

SCHWEIGHOFER, J. 1997. Evaluation of the Fully Turbulent Flow over a Flat Plate for a Large Range of Reynolds Numbers,

Master's Thesis, Ship Laboratory, Helsinki University of Technology.

SIIKONEN, T., HOFFRÉN, J. AND LAINE, S. 1990. A Multigrid LU Factorization Scheme for the Thin-Layer Navier-Stokes Equations, Proc. 7th ICAS Congress, Stockholm.

SIIKONEN, T. 1994. An Application of Roe's Flux-Difference Splitting for k-ϵ Turbulence Model, Report A-15, Laboratory of Aerodynamics, Helsinki University of Technology.

SIIKONEN, T. 1995. An Application of Roe's Flux-Difference Splitting for k-ϵ Turbulence Model, *International Journal for Numerical Methods in Fluids*, Vol. 21, No. 11.

SIIKONEN, T. 1996. FINFLO User Guide, Version 2.2, Laboratory of Applied Thermodynamics, Helsinki University of Technology.

THE SOCIETY OF NAVAL ARCHITECTS AND MARINE ENGINEERS. 1988. Principles of Naval Architecture, Volumes 2 and 3.

STARKE, B. 2001. A Validation Study of Wake-Field Predictions at Model and Full Scale Reynolds Numbers, *Fourth Numerical Towing Tank Symposium*, Hamburg, Germany.

STERN, F., PATERSON, E.G. AND TAHARA, Y. 1996. CFDSHIP-IOWA: Computational Fluid Dynamics Method for Surface-Ship Boundary Layers, Wakes and Wave Fields, IIHR Report 381, Iowa Institute of Hydraulic Research, College of Engineering, The University of Iowa, pp. 11.

SUNDELL, T. 1997. Computation of the Free Surface Flow around a Ship Using the NS Solver FINFLO, Report VALB279, VTT Manufacturing Technology, Espoo, Finland.

TAHARA, Y. AND IWASAKI, Y. 1998. A Study of Transom-Stern Free-Surface Flows by 2-D Computational and Experimental models, New Ship & Marine Technology into the 21st Century, Conference Proceedings, Osaka Prefecture University, Japan, pp. 83-92.

TZABIRAS, G.D. 1992. A Numerical Investigation of the Reyn-

olds Scale Effect on the Resistance of Bodies of Revolution, *Ship Technology Research - Schiffstechnik*, Volume 39, No. 1, pp. 28-44.

TZABIRAS, G.D. 1993. Resistance and Self-Propulsion Numerical Experiments on Two Tankers at Model and Full Scale, *Ship Technology Research - Schiffstechnik*, Volume 40, No. 1, pp. 20-38.

VANDEN-BROECK, J.-M. 1980. Nonlinear Stern Waves, *Journal of Fluid Mechanics*, part 3, pp. 603-611.

VOGT, M. 1998. A Numerical Investigation of the Level Set Method for Computing Free Surface Waves, Licentiate Thesis, CHA/NAV/R-98/0054, Department of Naval Architecture and Ocean Engineering, Chalmers University of Technology.

WILCOX, D.C. 1993. Turbulence Modelling for CFD, DCW Industries Inc., La Cañada, California.

WINTER, K.G. AND GAUDET, L. 1973. Turbulent-Boundary Layer Studies at High Reynolds Numbers at Mach Numbers between 0.2 and 2.8, Aeronautical Research Council, Reports and Memoranda, R. & M. No. 3712, London.

WHITE, M.F. 1991, Viscous Fluid Flow, second edition, McGraw-Hill, New York.

YAMANO, T., IKEBUCHI, T. AND FUNENO, I. 2000. On Forward-Oriented Wave Breaking just behind a Transom Stern, *Journal of the Society of Naval Architects of Japan*, No. 187, pp. 25-32.

YAMANO, T., IKEBUCHI, T. AND FUNENO, I. 2001. Stern Waves consisting of Forward-Oriented Breaking Waves and the Remaining Following Waves, *Journal of Marine Science and Technology* , No. 6, pp. 13-22.